QUANTITATIVE IMAGING TECHNIQUES TO GUIDE CLINICAL DECISION MAKING AND TREATMENT OF GLIOBLASTOMA

A Dissertation
Presented to
The Academic Faculty

by

Karthik K. Ramesh

In Partial Fulfillment

Of the Requirements for the Degree Doctor of Philosophy in Biomedical Engineering

Wallace H. Coulter Department of Biomedical Engineering

Georgia Institute of Technology and Emory University
May 2024

QUANTITATIVE IMAGING TECHNIQUES TO GUIDE CLINICAL DECISION MAKING AND TREATMENT OF GLIOBLASTOMA

Reviewed by:

Dr. Hyunsuk Shim, Advisor
Wallace H. Coulter Department of Biomedical Engineering
Georgia Institute of Technology and *Emory University*

Dr. Brent D. Weinberg
Wallace H. Coulter Department of Biomedical Engineering
Georgia Institute of Technology and *Emory University*

Dr. Lee A.D. Cooper
Department of Pathology and Institute for Artificial Intelligence in Medicine
Northwestern University

Dr. Hui-Kuo G. Shu
School of Medicine Department of Radiation Oncology
Emory University

Dr. Amir Pourmorteza
Wallace H. Coulter Department of Biomedical Engineering
Georgia Institute of Technology and *Emory University*

Date Approved: March 4th, 2024

To my late sister, Sahana Darshini Ramesh.

ACKNOWLEDGEMENTS

First and foremost, without the support and vision of my advisor Dr. Hyunsuk Shim, none of this would have been possible. I am eternally grateful for her mentorship over the years that has shaped me into the researcher that I am today. I would also like to express gratitude towards all the scientists that collaborated with and guided me through completing this dissertation. Dr. Weinberg was incredibly kind and provided plenty of support editing every one of my publications and meeting weekly to discuss my research progress and give advice as well as encouragement. I would also like to thank my other committee members – Dr. Shu, Dr. Cooper, and Dr. Pourmorteza for their support and guidance.

I would also like to thank everyone in my research lab for being directly involved with and helping my research. None of this is possible without a concerted team effort. I would like to thank Zander, Vicki, Anu, and Abi, who have made it a joy to work on these projects. Finally, without Saumya Gurbani, the PhD student who mentored me when I joined the lab, I would not have had any of these publications.

I would like to thank my family for nurturing and guiding my interests and dreams. I wanted to pursue a PhD to follow in the footsteps of my father, Anapathur Ramesh, and would not have had the gall to believe in myself without the support of my mother, Nalini, and uncle Gireesh Vedachalam. My fiancée Ananya, who I met in the middle of my PhD, has been a constant beacon of light throughout the darkest and brightest parts of this effort. Finally, I would like to thank my sister Sahana, who was immensely proud of me and my accomplishments, and was even praising my research hours before her death.

TABLE OF CONTENTS

ACKNOWLEDGEMENTS **iv**

LIST OF TABLES **viii**

LIST OF FIGURES **ix**

LIST OF SYMBOLS AND ABBREVIATIONS **xvi**

SUMMARY **xix**

Chapter 1. Introduction and Background **1**
1.1 Clinical Hurdles of Treating Glioblastoma **1**
1.2 Need for Advanced Imaging Techniques for GBM Treatment **3**
1.2.1 Clinical Standard 3
1.2.2 Spectroscopic Imaging 5
1.3 Need for Predictive Analytics for Tumor Tracking **6**
1.3.1 Importance of Tumor Recurrence Determination 6
1.3.2 Age of Artificial Intelligence 8
1.4 Closing the Gap to Clinical Translation **8**

Chapter 2. A multisite pilot clinical trial of spectroscopic MRI-guided radiation dose escalation in glioblastoma patients: Interim results and toxicity reports **10**
2.1 INTRODUCTION **10**
2.2 METHODS **13**
2.2.1 Eligibility Criteria 13
2.2.2 Image Acquisition 14
2.2.3 Target Generation 15
2.2.4 Treatment Plan 18
2.2.5 Follow-up 19
2.2.6 Statistical Analysis 20
2.3 RESULTS **20**
2.3.1 Study Participants 20
2.3.2 Survival Analysis 24
2.3.3 Radiation Treatment Effects 26
2.3.4 Toxicity 28
2.4 DISCUSSION **29**
2.5 CONCLUSION **31**

Chapter 3. Spectroscopic MRI-Based Biomarkers Predict Survival for Newly Diagnosed Glioblastoma in a Clinical Trial **32**
3.1 INTRODUCTION **32**
3.2 METHODS **33**
3.2.1 Description of tumor volume determination/target generation 33
3.2.2 Surgical resection classification 38

3.2.3 Statistical analysis/survival analysis 38
3.3 RESULTS 39
3.4 DISCUSSION 43
3.5 CONCLUSION 46

Chapter 4. The Longitudinal Imaging Tracker (BrICS-LIT): a cloud platform for monitoring treatment response in glioblastoma patients 47
4.1 INTRODUCTION 47
4.2 METHODS 49
4.2.1 Software Architecture 49
4.2.2 Semi-Automated Segmentation of Lesion 52
4.2.3 Visualization and Manual Editing 54
4.2.4 BT-RADS Scoring and REDCap Integration 54
4.3 RESULTS 55
4.4 DISCUSSION 58

Chapter 5. A Novel Approach to Determining Tumor Progression Using a Three-Site Pilot Clinical Trial of Spectroscopic MRI-Guided Radiation Dose Escalation in Glioblastoma 61
5.1 INTRODUCTION 61
5.2 METHODS 64
5.2.1 Clinical Trial Treatment Protocol 64
5.2.2 Follow-Up 66
5.2.3 Tumor Recurrence Determination 69
5.2.4 Survival Analysis 70
5.3 RESULTS 71
5.3.1 Survival Analysis 71
5.3.2 Example Assessments of Recurrence Using Patient Follow-Up 73
5.4 DISCUSSION 77
5.5 CONCLUSION 81

Chapter 6. A Fully Automated Post-Surgical Brain Tumor Segmentation Model for Radiation Treatment Planning and Longitudinal Tracking 82
6.1 INTRODUCTION 82
6.1.1 Related Work 82
6.1.2 Purpose 84
6.2 METHODS 85
6.2.1 Preparation of Training Data 85
6.2.2 Segmentation Models and Training 88
6.2.3 Application of Segmentation in Longitudinal Tracking 90
6.3 RESULTS 91
6.3.1 Segmentation for RT Planning 91
6.3.2 Application of Segmentation in Longitudinal Tracking 94
6.4 DISCUSSION 96
6.5 CONCLUSION 100

Chapter 7. Final report on clinical outcomes and tumor recurrence patterns of a human pilot study assessing efficacy of belinostat (PXD-101) combined with chemoradiation in treating newly diagnosed glioblastoma 102
7.1 INTRODUCTION 102
7.2 METHODS 103
7.2.1 Patient Enrollment 103
7.2.2 Treatment 104
7.2.3 Follow-Up 106
7.3 RESULTS 107
7.3.1 Survival Analysis 107
7.3.2 Radiation Overlap Statistics 109
7.3.3 Recurrence Analysis and Toxicities 112
7.4 DISCUSSION 115
7.5 CONCLUSION 119

Chapter 8. The Utility of Spectroscopic MRI in Stereotactic Biopsy and Radiotherapy Guidance in Newly Diagnosed Glioblastoma 120
8.1 INTRODUCTION 120
8.2 METHODS 124
8.2.1 Stereotactic Biopsy 124
8.2.2 Tumor Volume Determination (NCT02137759) 125
8.2.3 Statistical Analysis/Survival Analysis 127
8.3 RESULTS 129
8.3.1 Stereotactic Biopsy 129
8.3.2 NCT02137759 Retrospective Analysis 131
8.4 DISCUSSION 137
8.5 CONCLUSION 141

Chapter 9. Conclusions and Future Work 143
9.1 MAIN CONTRIBUTIONS 143
9.1.1 Clinical Translatability of Spectroscopic MRI 143
9.1.2 Automated Post-Treatment Tracking of Glioblastoma 144
9.2 FUTURE WORK 145
9.2.1 Spectroscopic MRI to Guide GBM Treatment 145
9.2.2 Additional Applications of Spectroscopic MRI 146
9.2.3 Automated Approaches for Tumor Segmentation and Longitudinal Tracking 147
9.3 CONCLUSION 149

APPENDIX A 151
A1. List of Publications 151
A2. List of Abstracts 153

REFERENCES 155

LIST OF TABLES

Table 2.1	Subject Demographics and Clinical Data	19
Table 2.2	Grade 3 or Greater Toxicities At Least Possibly Due to Therapy	24
Table 3.1	Classification of all 28 patients based on extent of resection (EOR) and residual postcontrast enhancement (rENH) volume.	36
Table 5.1	Compiled genetic and PFS data for 14 of the 19 patients with confirmed tumor progression.	69
Table 6.1	A comparison of strengths and weaknesses between previous efforts in brain lesion segmentation and our proposed effort.	81
Table 6.2	A comparison of 2D and 3D approaches to post-surgical GTV segmentation. The CNN-based 3D Unet outperforms the other models on our test dataset with the highest Dice scores (bolded).	87
Table 7.1	Summary statistics for both cohorts including tabulation of significant toxicities (≥grade 3) in all patients. * All occurrences were at 750 mg/m^2/day dosing.	103
Table 7.2	Minimum, maximum, and mean radiation dose to recurrence volume (rGTV), overlap between rGTV and PTV1, and overlap between rGTV and PTV2.	106
Table 8.1	Recurrence Analysis Results.	129

LIST OF FIGURES

Figure 2.1 (a) Example subject after gross total resection with only expected linear post-operative enhancement around the resection cavity on T1w-CE MRI (left). A contour was generated in BrICS where the Cho/NAA ≥ 2x normal results in a GTV3 volume of 18.45 mL (right). This GTV3 received 75 Gy. (b) Summary of the RT target volumes and doses used in this study. All doses were delivered in 30 fractions of concurrent dose-painted intensity modulated RT. 12

Figure 2.2 For the patient in Figure 2.1, an RT dose-volume histogram is shown on the left for each PTV volume. Overlays of each PTV (PTV1 green line, PTV2 blue line, PTV3 red line) as well as the radiation dose cloud over the patient's treatment planning CT are shown. 14

Figure 2.3 Patient enrollment pipeline for this trial. 18

Figure 2.4 Scatter plot of GTV3 volume vs residual T1w-CE volume for each patient on the trial. While there isn't a clear correlation between T1w-CE and GTV3 volume, the GTV3 volume is consistently larger than the T1w-CE volume. 20

Figure 2.5 Kaplan-Meier estimator for (a) overall survival (OS) with median of 23.0 months and (b) progression free survival (PFS) with median of 16.6 months are shown. 95% confidence intervals are included (grayed out area). 21

Figure 2.6 Examples of two cases with "late pseudoprogression," or radiation necrosis are shown. [**Case #1**] (a) At 1-month post-RT, residual enhancement is seen on T1w MRI within the pink PTV3 contour. (b) At 5 months post-RT, residual enhancement has increased, but the relative cerebral blood volume (rCBV) map on dynamic susceptibility contrast (DSC) perfusion MRI shows minimal to no perfusion. (c) Repeat resection demonstrated 100% necrosis on H&E-stained sections. [**Case #2**] (d) At 1-month post-RT, there is primarily linear, post-operative enhancement on T1w-CE MRI within the red PTV3 contour. (e) At 8 months post-RT, increasing enhancement is seen at periphery of cavity. The DSC perfusion MRI again shows no definitive hyperperfusion. (f) Repeat resection again found predominantly (99%) necrosis on H&E-stained sections. 23

Figure 3.1 A comparison of an example gross tumor volume 3 (GTV3) treatment volume to the resection cavity with standard of care margins. Due to no residual enhancing tumor, standard of care would involve treating the cavity with a margin. (A) An axial view of the GTV3 contour (green) that extends past the resection cavity (blue), 32

resection cavity with 5 mm margin (yellow), 10 mm margin (orange), and 20 mm margin (red). (B) This 3D view of the GTV3 contour shows a small amount of infiltrating tumor (arrow) that extends even past the 20 mm margin. (C-E) 3D views of the resection cavity with various margins and volumes calculated. A Dice overlap score was calculated between each margin and GTV3. For (C), (D), (E), and (F), the Dice scores were 0.18, 0.47, 0.59, and 0.40, respectively. The percentages of volumes in (C), (D), (E), and (F) which are not included in (B) were 37.4%, 41.3%, 49.7%, and 74.9% respectively.

Figure 3.2 Two sample cases are shown. In the first case, the first column shows the residual postcontrast enhancement (rENH) contour with a volume of 12.11 cc, overlaid on the T1-weighted contrast-enhanced (T1w-CE) MRI (first row) for a 54-year-old female glioblastoma patient. The second column shows the gross tumor volume 3 (GTV3) contour over 5 times larger than rENH with a volume of 63.37 cc. The second row is a three-dimensional rendering of both contour volumes overlaid on a T1 precontrast image. In the second case of a 56-year-old female glioblastoma patient, there is no residual contrast enhancement visible on the T1w-CE MRI, whereas the GTV3 volume is 18.45 cc. 33

Figure 3.3 Kaplan-Meier survival curve of progression-free survival (PFS) for the 28 IDH wild type patients included in this analysis. The median PFS is 16.2 months and median time to follow-up is 22.4 months. 35

Figure 3.4 Gross tumor volume 3 (GTV3) and residual postcontrast enhancement (rENH) plot indicating low correlation between the two volumes based on R^2=0.127 (p=0.063). The horizontal blue line indicates the median GTV3 volume (19.2 cc), and the vertical orange line indicates the median rENH volume (2.1 cc). 37

Figure 3.5 (A) Kaplan-Meier survival curve for overall survival (OS) stratified into equal groups by the median residual contrast enhancing (rENH) tumor volume (2.1 cc). The median OS for patients with rENH > 2.1 cc is 21.3 months, and the median for OS for patients with rENH < 2.1 cc is 23.0 months. (B) Kaplan-Meier survival curve for OS stratified into equal groups by the median gross tumor volume 3 (GTV3) (19.2 cc). The median OS for patients with GTV3 > 19.2 cc is 17.1 months, and the median OS for patients with GTV3 < 19.2 cc is 27.4 months. (C) Kaplan-Meier survival curve for progression free survival (PFS) stratified into equal groups by the median rENH tumor volume (2.1 cc). The median PFS for patients with rENH > 2.1 cc is 12.8 months, and the median PFS for patients with rENH < 2.1 cc is 19.0 months. (D) Kaplan-Meier survival curve for PFS stratified into equal groups by the median GTV3 (19.2 cc). The 39

median PFS for patients with GTV3 > 19.2 cc is 12.6 months, and the median PFS for patients with GTV3 < 19.2 cc is 24.0 months.

Figure 4.1 An example GBM patient enrolled in our dose escalation trial at Emory site. Follow-up images are displayed from the earliest date on the far right (pre-RT) to the most recent date on the left. T2 FLAIR (top row) and CE-T1w MRIs (bottom row) are co-registered and interpolated to allow for simultaneous scrolling through all slices. 47

Figure 4.2 The same patient from Figure 1 with their radiation planning dose map overlaid. The MRIs on the far right do not have radiation overlaid as that visit preceded the start of radiation treatment. 47

Figure 4.3 For the semi-automated CE-T1w segmentation, (A) a clinician must place a seed in the region of interest. (B) Otsu thresholding and filtering identifies extent of enhancement. (C) Indicates the segmented contour for a representative slice after region growing. (D) The entire volume of segmented lesion. The FLAIR segmentation also requires (E) users to make a seed within the hyperintense region. (F) After smoothing, thresholding, and region growing the contour has segmented the extent of hyperintensity. (G) A volumetric representation of FLAIR hyperintensity for this patient. 49

Figure 4.4 Clinicians and researchers can open a window within LIT that displays relevant clinical and genomic data automatically retrieved from a REDCap database that can assist in BT-RADS scoring. 51

Figure 4.5 An example Johns Hopkins GBM patient with follow-up imaging co-registered and ready to view in BrICS-LIT. Contours have been generated semi-automatically with respective volumes of lesion calculated. A neuroradiologist used the segmented volumes, along with REDCap data on the right panel to assign BT-RADS scores for each visit date. 53

Figure 4.6 A GBM patient from our dose escalation trial at University of Miami who initially received a radiation dose of 75 Gy in the left occipital lobe. However, by 1/29/2019, a distant contrast enhancing lesion appears in the left frontal lobe, away from the radiation treatment zone (indicated by red arrow). 54

Figure 5.1 A comparison between the ratio map of choline to N-acetylaspartate (Cho/NAA) and T1-weighted contrast-enhanced (T1w-CE) imaging for three patients on the trial. For each patient, the top left image contains the Cho/NAA ratio map superimposed on the T1w image along with a contour encompassing all voxels with a Cho/NAA ≥ 2x normal. That contour is overlaid on the T1w-CE image on the top 62

right image which shows enhancement from residual tumor and recent surgery. The bottom left image shows a 3D volume rendering of the volume of tissue that received 75 Gy of radiation guided by the Cho/NAA ≥ 2x contour, while the bottom right image shows a 3D volume rendering of the residual contrast enhancing lesion, which normally receives 60 Gy of radiation along with resection cavity in standard therapies. In all cases, the Cho/NAA ≥ 2x contour was significantly larger than the contrast-enhancing lesion.

Figure 5.2 A view of the Brain Imaging Collaboration Suite Longitudinal Imaging Tracker (BrICS-LIT). The top row consists of T2-weighted fluid-attenuated inversion recovery (FLAIR) MRIs and the middle row of T1w-CE MRIs co-registered and interpolated to an atlas for easier comparison. Studies are longitudinally arranged from newest (left column) to oldest (right column). Segmented lesions are overlaid in the top two rows, while the radiation dose map is overlaid on the T1w-CE MRI in the bottom row to intuitively determine the radiation dose received of the suspected recurring tumor. 65

Figure 5.3 Kaplan–Meier estimator for PFS; median PFS: 16.6 months with a median time to follow-up of 20.3 months. 68

Figure 5.4 With our web platform, clinicians assessed (A) graphs of lesion volumes from FLAIR and T1w-CE (labeled ENH) imaging, as well as (B) A graph of Brain Tumor Reporting and Data System (BT-RADS) scores during a patient's follow-up. The red stars indicate re-resection of suspected lesions. In this case, the patient had two re-resections (16.3 and 25.2 months) with significant treatment effect and necrosis found in both cases. (C) For each follow-up visit in the above graph, the FLAIR MRIs (top row), T1w-CE MRIs (middle row), and radiation dose map overlaid on T1w-CE MRIs (bottom row) are displayed from oldest (left column) to newest (right column). While the increasing enhancing rim as well as FLAIR volumes were cause for concern, this patient had still not had confirmed disease progression. 71

Figure 5.5 (A) A graph of changing lesion volumes from FLAIR and T1w-CE (labeled ENH) imaging can help assess suspicious trends, especially after re-resection in this case. (B) A graph of BT-RADS scores during a patient's follow-up. The red star indicates re-resection of suspected lesions. This patient had one follow-up surgery that found 30% tumor in samples biopsied (13.4 months). Therefore, their recurrence date (orange diamond) was set before their follow-up surgery. (C) For each follow-up visit in the above graph, the FLAIR MRIs (top row), T1w-CE MRIs (middle row), and radiation dose map overlaid on T1w-CE MRIs (bottom row) are displayed. From 72

the 14th month onwards, a second lesion is apparent on the contralateral side of the brain outside of the radiation treatment zone.

Figure 6.1 FLAIR and CE-T1w segmentation overlays (in red) from a BraTS competition-winning segmentation model over MRIs prior to surgery, prior to receiving radiation therapy, and 3 months after completing radiation therapy. 79

Figure 6.2 Example contour overlays from our training dataset of GTV1 (yellow contour) overlaid on T2w/FLAIR MRI and GTV2 (red contour) on CE-T1w MRI that includes cavity and blood product. 82

Figure 6.3 (A) Training pipeline for our segmentation models. During the pre-processing step, a 3-channel input was used with the first two channels using skull-stripped T2w/FLAIR and CE-T1w MRIs and the third channel including skull to assist in delineating cavity margins. The model weights that performed the best with the validation data were tested on the independent test dataset. (B) Network architecture for 3D Unet, which has a depth of 3, and was trained on our post-operative MRIs after pre-processing. The number of filters is listed above each block. 84

Figure 6.4 Example GTV2 (CE-T1w target) and GTV1 (T2w/FLAIR target) segmentations for patients from three different institutions with our best-performing 3D Unet model. For GTV2 and GTV1, we have included an axial view of the clinician GTVs (red) and the prediction (blue) as well as a volume-rendered view of the contour overlap in the sagittal orientation. Dice scores are included between the 2D and volume rendering for each example. 90

Figure 6.5 The three worst-performing cases of our 3D Unet model. In (A), the small CE-T1w lesion is missed, possibly being confused for blood vessel. In (B), the model has difficulty capturing the entire extent of hyperintensity from the 3D T2w/FLAIR acquisition, and in (C), the model confuses the ventricle for the shape of a cavity, especially when there are T2w/FLAIR edema in the same region. 90

Figure 6.6 The 3D Unet segmentation model implemented into our web application BrICS-LIT, displayed for an example patient's post-operative and post-RT follow-up MRIs. Automated lesion segmentations (red overlay) and lesion volume cutoffs assist in generating automated structured reporting scores (bottom row) for post-treatment longitudinal tracking. 92

Figure 6.7 Interactive chart tracking changes in CE-T1w lesion volume (ENH), T2w/FLAIR lesion volume, and structured reporting scores for the 92

patient shown in Figure 6.6. A drastic increase in lesion volume is seen 6 months after surgery.

Figure 7.1 One-year timeline of chemotherapy, intravenous belinostat, and radiation for patients in NCT02137759. 101

Figure 7.2 (A) Overall Survival (OS) Kaplan-Meier Survival Curves. The median OS for the control and belinostat cohorts was 15.8 and 18.5 months, respectively (p = 0.53), for all patients. (B) Progression free survival (PFS) for all patients. The median PFS for control and belinostat cohorts was 9.0 months and 9.3 months, respectively (p = 0.75). 104

Figure 7.3 T1 post-contrast imaging in three patients, by horizontal row, with out of field recurrence in cohort 2. For each patient, the enhancing recurrence contour (rGTV) encompasses lesion that has spread outside the extent of radiation treatment targets PTV1 (guided by T2/FLAIR) or PTV2 (guided by T1w-CE). 107

Figure 7.4 Pre-RT sMRI scans suggest out-of-field recurrence in the belinostat cohort with tumor infiltration beyond what is shown in standard imaging. (A) This patient had two-fold Cho/NAA elevation that had spread contralaterally. While pre-RT standard imaging failed to detect this, FLAIR hyperintensity at recurrence mimics the direction of tumor infiltration detected by pre-RT sMRI. (B) The second patient had tumor infiltration across the midline that wasn't detected by pre-RT standard imaging. Lesions at recurrence in both T1w-CE and FLAIR MRIs confirm Cho/NAA abnormalities in the pre-RT sMRI scan, suggesting standard imaging underestimated the extent of tumor infiltration. (C) This patient had a large lesion of metabolically active tumor that was not shown in T1w-CE, thus, undertreated, which became apparent at recurrence. 108

Figure 8.1 Graphical depiction of the calculations performed for overlap analysis. The goal of our analysis was to quantify the region of overlap (purple) between the recurring contrast enhanced volume (red) and Cho/NAA ≥ 2X excluding (light blue) the original treatment volume (GTV2 or CTV2), depicted in black. This would allow us to infer the capability of pretreatment sMRI in predicting areas of subsequent recurrence. 124

Figure 8.2 Patient with low grade glioma presented for repeat biopsy to assess possible disease progression. Due to lack of enhancement in CE-T1w and difficulty finding the areas most suspicious for progressive tumor within the FLAIR volume, sMRI was utilized to better delineate target for biopsy. As noted, the FLAIR volume (red) of 86.4 cc is too large to allow for adequate targeting during surgical 125

biopsies. Cho/NAA ratio five times (yellow) abnormal was instead utilized to delineate biopsy target. The 3D contour of Cho/NAA ≥ 5X (yellow) and Cho/ NAA ≥ 2X (blue) is shown for comparison. The 2X volume is typically used for radiation-treatment while the 5X threshold maximizes tumor density and probability of a successful biopsy. All images are displayed in our in-house program, the Brain Imaging Collaboration Suite (BrICS).

Figure 8.3 Medtronic S8 Stealth® Navigation Tool with 5X Cho/NAA biopsy target displayed. Entry point coordinate was (72, 15, -14) and target point, depicted by the red crosshair, was at coordinates (36, 12, -15) in MRI DICOM space. Total travel distance was 36.1 mm to reach target volume. The blue line shows the projected travel of the needle. The patient's face is obscured for anonymity. 126

Figure 8.4 (A) A representative patient from the belinostat cohort displaying the vast difference in the T1w-CE derived volume compared to the Cho/NAA ≥ 2x volume. (B) The High-Mismatch Group patients (red) had much larger Cho/NAA ≥ 2x volumes compared to the T1w-CE lesion and showed a median survival of 14.4 months, whereas the counterpart (Low-Mismatch Group) had a smaller difference between Cho/NAA ≥ 2X and the T1w-CE lesion with a median survival of 34.3 months. 128

Figure 8.5 A representative case from the High-Mismatch Group with recurrence overlap analysis using GTV2. (A) An axial view of the GTV2 (blue), pre-RT Cho/NAA ≥ 2X, and rCE excluded from GTV2 (yellow) and rCE within the GTV2 (red) These images were acquired 3 months after the progression date calculated using BT-RADS and clinical correlations. (B) 3D images of the rCE volume excluding GTV2 (yellow), the pre-RT Cho/NAA ≥ 2X (green), and the GTV2 (blue). (C) 3D images of the rCE excluded from GTV2 (yellow) and pre-RT Cho/NAA ≥ 2X (green) without the GTV2 displaying the 54.5% overlap between the two volumes. 130

Figure 8.6 A representative case from the High-Mismatch Group with recurrence overlap analysis using CTV2. This is the same patient displayed in Figure 5. (A) An axial view of the CTV2 (blue), pre-RT Cho/NAA ≥ 2X, and rCE excluded from CTV2 (yellow) and rCE within the CTV2 (red). Similar to Figure 5, these images were acquired 3 months after the progression date calculated using BT-RADS and clinical correlations. (B) 3D images of the rCE volume excluding CTV2 (yellow), the pre-RT Cho/NAA ≥ 2X (green), and the CTV2 (blue). (C) 3D images of the rCE excluded from CTV2 (yellow) and pre-RT Cho/NAA ≥ 2X (green) without the CTV2 displaying the 24.8% overlap between the two volumes. 132

LIST OF SYMBOLS AND ABBREVIATIONS

3D	3-dimensional
3T	3-Tesla (MRI magnetic field strength)
AI	Artificial Intelligence
BraTS	Brain Tumor Segmentation Challenge
BrICS	Brain Imaging Collaboration Suite
BT-RADS	Brain Tumor Reporting and Data System
CE-T1w	Contrast-enhanced T1w MRI (same as T1w-CE)
Cho	Choline
Cho/NAA	Normalized ratio of Choline to N-acetylaspartate
CNN	Convolutional Neural Network
Cr	Creatine
CSI	Chemical Shift Imaging
CT	Computed Tomography
CTV	Clinical Tumor Volume
DLT	Dose Limiting Toxicities
EOR	Extent of Resection
EPSI	Echo-Planar Spectroscopic Imaging
ESAPI	Eclipse Scripting Application Programming Interface
FA	Flip Angle (MRI)
FLAIR	T2-weighted Fluid-Attenuated Inversion Recovery MRI
GBM	Glioblastoma
GRAPPA	GeneRalized Autocalibrating Partial Parallel Acquisition
GTR	Gross Total Resection

GTV	Gross Tumor Volume
Gy	Gray (unit for ionizing radiation dose)
HDAC	Histone Deacetylase
HDACi	Histone Deacetylase Inhibitor
IDH	Isocitrate Dehydrogenase
IRB	Institutional Review Board
ITK	Insight Toolkit
LIT	Longitudinal Imaging Tracker
MIDAS	Metabolite Imaging and Data Analysis System
MPRAGE	T1w Magnetization-Prepared Rapid Acquisition Gradient Echo
MRI	Magnetic Resonance Imaging
MRSI	Magnetic Resonance Spectroscopic Imaging
NAA	N-acetylaspartate
NAWM	Normal Appearing White Matter
NCTN	National Clinical Trials Network
OS	Overall Survival
PFS	Progression Free Survival
PTV	Planning Treatment Volume
RANO	Response Assessment in Neuro-Oncology
rCE	Recurrence volumes determined by T1w-CE
rENH	Residual Post-contrast Enhancement (after surgery)
rGTV	Tumor recurrence volumes based on enhancement
RT	Radiation Therapy
SAHA	Suberanilohydroxamic
SIB	Simultaneous Integrated Boost

sMRI	Spectroscopic MRI
SNR	Signal-to-noise ratio
Sox2	Sex Determining Region Y-box 2
SRS	Stereotactic Radiosurgery
STR	Subtotal Resection
Swin	Shifted Window (Transformer-based CNN approach)
T1w-CE	T1-weighted Contrast Enhanced MRI
TE	Echo Time (MRI)
TMZ	Temozolomide
TR	Repetition Time (MRI)
TTF	Tumor Treating Fields
WebGL	Web Graphics Library
WHO	World Health Organization

SUMMARY

Treatment of glioblastoma (GBM), a grade IV brain tumor, is complex and challenging. Despite an aggressive treatment protocol of surgery, radiation treatment, and chemotherapy, patient outcomes are poor. Throughout a patient's treatment timeline, imaging is central to clinical decision making. The gold standard imaging for treatment of GBM is magnetic resonance imaging (MRI). While clinical MRIs show some extent of tumor infiltration, they do not capture the entire extent and further, can struggle to define tumor margins. Spectroscopic MRI (sMRI) measures the endogenous metabolites in the brain and in particular, a ratio of two metabolites (choline and N-acetyl aspartate) shows tumor margins that extend well past what's seen in the clinic. To that end, we first present our efforts to guide GBM treatment with sMRI. Next, we analyze whether pre-treatment insights from sMRI correlate with patient survival and outcomes. Finally, GBM patients are tracked with clinical imaging after completing surgery and chemoradiation. To improve objectivity and robustness in post-treatment patient tracking, we have developed deep learning algorithms to quantify patient lesions and provide assistive suggestions to physicians for whether tumor recurrence has occurred. By utilizing sMRI during treatment and the latest deep learning algorithms after treatment, we have improved GBM patient survival and provided insights that can help physicians treat patients more proactively. Further, all our algorithms are housed in software that fit seamlessly into clinician workflows as the integration of quantitative tools and imaging into the clinic is vital towards affecting patient lives directly. Future plans involve translating sMRI and our quantitative software into the clinic to assist clinicians and improve patient livelihood.

Chapter 1. Introduction and Background

1.1 Clinical Hurdles of Treating Glioblastoma

Glioblastoma (GBM), a grade IV primary brain tumor, has devastated millions of families around the world with an annual incidence rate of 3.19 per 100,000 in the United States alone [1]. The median time of survival is typically 10-12 months from diagnosis [2], with a five-year survival rate of only 6.8% [2,3]. Treatments for this form of cancer are intense, invasive, and painful, and commonly include surgery, high-dose radiation treatment, and chemotherapy. Curiously, little has improved patient outcomes in the past decades. Even with an aggressive treatment protocol, median survival time is typically 15-16 months [4-6].

Patients with GBM typically present with symptoms largely arising from increased pressure in the brain due to active tumor proliferation. Symptoms include but are not limited to seizures, headaches, memory loss, speech difficulty, and changes in vision. Patients presenting with symptoms are typically screened for lesions or abnormalities via medical imaging such as computed tomography (CT) or the gold standard magnetic resonance imaging (MRI). Tissue samples are taken from areas of visible tumor via biopsy and undergo histological analysis. The presence of necrosis, microvascular proliferation, increased cell density, and atypia are hallmarks of GBM, with the first two features leading to a grade IV characterization [7]. However, the presence of these features can vary due to the heterogeneity of GBM as well as the tissue sample biopsied [8].

Glioblastoma is primarily composed of abnormal astrocytes, a type of glial cell. Glial cells are regularly referred to as the “glue” of the central and peripheral nervous system as they support neurons and their cellular environment. The main functions of healthy glia include providing insulation between neurons, supplying nutrients to neurons, as well as removing dead neurons and pathogens. Astrocytes in particular are star-shaped glial cells in the brain and spine that have numerous functions some of which include regulating transmission of electrical impulses between neurons, metabolic and nutrient support of neurons, and maintenance of the blood-brain-barrier (BBB). While the exact origin of glioblastoma is unknown, it is actively being researched, with a majority of glioblastomas presenting as grade IV from the onset [9].

Glioblastoma is incredibly infiltrative and rapidly spreads into neighboring brain tissue and along white matter tracts. Due to the rapidly invasive nature of GBM, as well as the potential loss of brain function, standard clinical treatment is aggressive. As mentioned previously, the standard Stupp protocol for treatment of GBM involves maximal-safe surgical resection of visible lesion in contrast-enhanced T1-weighted MRIs (T1w-CE), before administering radiotherapy (RT) to residual lesion in the brain with concurrent temozolomide (TMZ) chemotherapy [10]. After initial treatment, patients are imaged and tracked every 2-3 months to assess for recurring tumor, which could lead to subsequent surgeries or changes in treatment. Throughout the treatment and post-treatment timeline of a GBM patient, medical imaging is central to their clinical management. However, the gold standard imaging modalities are limited in detecting the full extent of tumor infiltration, which leads to undertreatment of spreading tumor and overtreatment of otherwise healthy tissue at every stage. The ultimate basis for this work is 1) guiding GBM treatment with

advanced, quantitative imaging techniques such as spectroscopic MRI (sMRI) to capture the true extent of tumor infiltration in the brain and 2) using the latest deep learning and machine learning techniques to provide robust, actionable analytics during post-treatment follow-up for proactive treatment of GBM. Finally, this work continues the effort of bringing these quantitative techniques to clinical adoption.

1.2 Need for Advanced Imaging Techniques for GBM Treatment

1.2.1 Clinical Standard

The gold standard imaging used for diagnosis, evaluation, and treatment of GBM is magnetic resonance imaging (MRI). Broadly, the phenomenon of magnetic resonance or nuclear magnetic resonance (NMR) involves the nuclei of atoms in a magnetic field being perturbed by radiofrequency (RF) pulses. After perturbation, the nuclei return to an equilibrium state and in that process generate an electromagnetic signal that can be measured by RF coils. When patients enter an MRI machine, they are essentially inside of a magnet with its own magnetic field parallel to the direction of the patient lying down (B_0). Protons in tissue, which normally are oriented randomly, will align in the same direction of the B_0 field due to having their own magnetic dipole. RF pulses are used to perturb protons into certain orientations before being turned off. In the process of turning on and immediately turning off an RF pulse, the protons perturb in a particular orientation and then relax towards equilibrium. During that relaxation process, an RF signal is emitted and measured to calculate tissue properties and generate images with tissue contrast.

Image contrast is generated due to the time it takes for protons in different tissue environments to relax. Depending on the time in which signal is acquired after RF pulse is

turned off, known as the echo time (TE), signal from certain tissue environments will be more prominent than that of others. In general, after perturbation by an RF pulse, protons initially rotate to the direction of the RF magnetization, and then relax to equilibrium parallel to the direction of B_0. That relaxation process generates an electromagnetic signal in two different directions as the protons wobble or undergo precession. When measuring the longitudinal magnetization, or the component of magnetization parallel to B_0, protons in various tissue environments recover at an exponentially decaying rate to a maximum magnetization in the B_0 direction. The time it takes for the longitudinal magnetization to reach 63% of its maximum is known as T1 relaxation and is a constant that is unique to certain tissue and fluid environments. When measuring magnetization perpendicular to B_0, due to the protons spinning perpendicular to B_0, the transverse magnetization is initially at its maximum before decaying to 0 in an exponentially decaying manner. T2 relaxation occurs when the transverse magnetization reduces by 37% from its initial maximum and is also unique to certain tissue and fluid environments. During image acquisition, the greatest contrast in longitudinal magnetization between tissue occurs very early during the relaxation phase and therefore, T1-weighted imaging (T1w), that depends on contrast leveraging T1, usually requires shorter TE acquisitions. To maximize T2 contrast, longer TE is used.

In T1w imaging of the brain, water and cerebrospinal fluid (CSF) appear dark while gray and white matter are both visible. In T2w imaging, CSF and water appear very bright, with generally less contrast between gray and white matter. Sometimes, gadolinium contrast agents (Gd) that alter the T1 relaxation time and make certain pathology appear more visible can be used. This is referred to as post-contrast imaging. For GBM, Gd

contrast is typically used during a T1w acquisition. Gd, which travels through blood, appears bright in T1w acquisitions, and therefore, T1w-contrast enhanced (T1w-CE) imaging is commonly used in the clinic to identify regions of the brain where the blood-brain-barrier (BBB) has broken down due to tumor infiltration. In GBM, it is typical to see a cavity forming due to necrosis surrounded by striated regions of enhancement due to leaky vasculature from infiltrating lesion spreading outward [11]. In T2w imaging, tissue with high water content appears bright along with surrounding, free moving CSF. In GBM, tissue where tumor is infiltrating and extending are highly inflamed, leading to a build-up of fluid (edema) and bright lesions. To improve visual contrast between edema and healthy surrounding tissue, an inversion recovery (IR) sequence is performed to effectively "null" bright signal from CSF. To that end, T2w/Fluid-Attenuated Inversion Recovery (FLAIR) imaging is also used in the clinic to guide treatment.

1.2.2 *Spectroscopic Imaging*

The problem with clinical imaging such as T1w-CE is that while visible abnormality from a presence of contrast is certainly a sign of leaky vasculature and therefore active tumor infiltration, it does not capture the entire extent of infiltrating tumor [12,13]. While T2w/FLAIR can capture much larger extents of infiltration, lesions visible in FLAIR are primarily due to edema and inflammation and are not necessarily all tumor [14,15]. Therefore, standard clinical imaging fails to not only differentiate healthy tissue from infiltrating tumor, it also cannot capture the entire extent of infiltrating tumor leading to overtreatment of healthy tissue, undertreatment of tumor, and overall poor outcomes for patients even after undergoing the intensive Stupp protocol.

Spectroscopic MRI (sMRI) attempts to resolve some of the hurdles that standard clinical imaging faces. Thus far, when describing magnetization from protons in both T1 and T2w imaging, the predominant magnetization is from water and lipids. That is, protons precessing in water and lipid environments generate anatomic contrast in standard clinical MRIs. However, when suppressing signal from water and lipid, precession from protons in other chemical compounds can be detected. sMRI involves the detection and quantification of signal from metabolites and other chemicals that are usually not seen due to overwhelming signal from water and lipid without the need for any contrast agent.

Choline (Cho) is a metabolite that correlates with high cell turnover, is indicative of high proliferation rates, and is generally much higher in tissue with tumor. N-acetyl Aspartate (NAA) is a metabolite that is high in healthy neuronal tissue, and generally lower in tissue microenvironments disrupted by tumor. The ratio of Cho/NAA is a biomarker for tumor infiltration and can often detect the extent of tumor with greater sensitivity and specificity than standard imaging [12,16-20]. To this end, several of the chapters in this dissertation utilize sMRI and the Cho/NAA ratio to guide treatment of GBM, track brain tumors, as well as investigate the effects of certain medications like Belinostat on brain metabolism. While MR Spectroscopic Imaging (MRSI) has existed for over forty years, it has made few inroads into the clinic. Our efforts to utilize spectroscopy for GBM treatment has led to recent progress in bringing sMRI to the clinic and leading to improved patient outcomes [13,21,22].

1.3 Need for Predictive Analytics for Tumor Tracking

1.3.1 Importance of Tumor Recurrence Determination

Initial treatment of GBM involves surgery and radiation treatment along with chemotherapy [10]. Physicians then inspect clinical imaging (T1w-CE and FLAIR) every two to three months for abnormal lesions and tumor recurrence. Previously, I mentioned the limitations of clinical imaging in guiding surgeries and radiation treatment. These limitations are exacerbated during the post-treatment follow-up phase as radiation necrosis, radiation-related inflammation, surgical-inflammation, and other factors can present as lesion in both T1w-CE and FLAIR, confounding physicians and leading to difficult decision making [23,24]. Ultimately, clinicians need to know when tumor has recurred as soon as possible to guide future decision making and extend patient survival. As soon as tumor recurrence occurs, patients may have only months to live, which makes it critical for the physician team to respond quickly, proactively, and with objectivity when they suspect the patient's initial treatment has failed.

Radiological post-treatment tracking can be particularly challenging because two different physicians could describe their findings in a subjective manner with slightly different interpretations of the very same set of imaging. This can make decision-making for other clinical teams a challenge as the next steps for treating the patient are unclear. Disease-specific structured reporting is a method of addressing some of these concerns. Structured reporting is a method of categorizing imaging findings into quantitative scores that each have their own interpretation [25,26]. For example, if two different radiologists looked at the same patient's imaging and included a quantitative score along with a written description of their findings, and the scores align with each other, physicians can more confidently determine the next steps for treating the patient. The Breast Imaging Reporting and Data System (BI-RADS) is one such popular framework for assigning categorical

scores to patient imaging visits [27]. These scores have led to improved patient tracking, robust treatment of the patient, and have later been used in research to correlate quantitative scores to patient likelihood of survival [28,29].

In brain tumor imaging, one such framework is known as the Brain Tumor Reporting and Data System (BT-RADS) [30,31]. This framework depends on changes in lesion size over time, which can still be somewhat subjective as physicians currently only visually inspect imaging across one or two dates to determine whether a lesion is larger or significantly larger for example. To improve post-treatment tracking of brain tumor patients, as well as more robust BT-RADS classifications, volumetric segmentation of lesion as well as quantitative cutoffs for scoring can help clinicians in determining whether a patient's condition is cause for concern.

1.3.2 Age of Artificial Intelligence

In the recent decade, computer vision has made great leaps in classification and segmentation. Its applications in medical imaging have also grown exponentially. For the task of volumetric segmentation, I first describe a semi-automated approach using classical image processing techniques [32]. I also, build on that work by testing and training the latest deep learning segmentation models in medical imaging for post-surgical GBM lesions [33]. Using automated lesion segmentation algorithms, we can assist radiation oncologists in designing radiation therapy plans as well as improve post-treatment tracking. By calculating lesion volumes and setting volumetric cutoffs, we can generate automated disease-state classifications that can assist physicians in assessing tumor recurrence.

1.4 Closing the Gap to Clinical Translation

This dissertation will showcase our efforts to improve GBM treatment. Chapters 2 and 3 delve into the enhanced benefits of sMRI in directing RT for GBM [21,34]. Chapters 4-6 concentrate on post-treatment follow-up, where we devised a software tool and segmentation algorithm to detect tumor recurrence [32,33,35]. Chapters 7 and 8 explore additional applications of sMRI and present findings from another clinical trial involving an epigenetic drug for GBM treatment [22,36].

While many of our efforts in this dissertation have improved patient survival and provided tools for physicians to evaluate GBM patients, this dissertation should hopefully highlight the efforts we have made to house these tools in software that clinicians can use. While previous efforts of applying artificial intelligence to healthcare have led to impressive results, few efforts have made it to the clinic. From our web application leveraging sMRI for RT planning, to housing our segmentation models and visualization tools in software for easier decision-making, we want to ensure that the work that is completed in this dissertation can seamlessly integrate with clinical workflows so that ultimately patient lives are improved, which is the overall hope and promise of this work.

Chapter 2. A multisite pilot clinical trial of spectroscopic MRI-guided radiation dose escalation in glioblastoma patients: Interim results and toxicity reports

2.1 INTRODUCTION

Glioblastomas (GBMs) are the most common malignant primary brain tumor in adults with an annual incidence of 3.19 per 100,000 in the United States [37]. Standard-of-care treatment for patients with newly-diagnosed GBM consists of maximally safe surgical resection followed by radiation therapy (RT) with concomitant and adjuvant temozolomide (TMZ). Despite advances in these treatment regimens over the last two decades, GBM continues to be an aggressive disease with a median overall survival of 15-16 months since the introduction of TMZ [6,38-40].

Part of the challenge treating GBMs is its infiltrative nature. To account for this, a two-tier system of imaging is typically used to target disease. T1-weighted contrast enhanced (T1w-CE) MRI utilizes intravenous injection of gadolinium contrast agent to identify leaky vasculatures accompanying high grade gliomas and compromised blood-brain barrier, which is the hallmark of GBMs. Thus, T1w-CE is a reasonable diagnostic imaging method to differentiate GBMs from the lower grade gliomas. T2-weighted fluid attenuated inversion recovery (FLAIR) MRI is less specific, but identifies not only tumor infiltration, but other pathologies such as edema, inflammation, and medication or radiation effects. To accommodate both imaging phenomena, high dose RT (typically 60 Gy) is targeted to the T1w-CE region, including any surgical resection cavity, and a lower dose 45-54 Gy to the FLAIR hyperintensity, both delivered over 30 fractions [41]. Given the

infiltrative nature of GBMs, an imaging modality that could more completely identify the extent of tumor spread, even if the tumor has not yet disrupted local anatomy or induced leaky neovasculature, would be beneficial in improving disease targeting to avoid marginal or distant failures. Furthermore, there has been ongoing work to determine the optimal radiation dosing to prevent in-field recurrence of disease, with higher doses up to 75 Gy being studied in trials such as the NRG-BN001 study [42].

Magnetic resonance spectroscopic imaging (MRSI) can non-invasively identify the chemical composition of tissue based on the nuclear magnetic resonance phenomenon [18]. Tumor cells have altered metabolism which can be detected using MRSI. Choline-containing compounds (Cho) make up the phospholipid bilayer of the cell membrane and are found in increased concentration in cells that are rapidly proliferating. N-acetylaspartate (NAA) is a protein found in neurons and is diminished in tissue samples when there is destruction of the local neuronal environment. The ratio of choline to NAA (Cho/NAA) has been previously shown to be greatly elevated in patients with GBM and can serve as a biomarker to differentiate regions of tumor from healthy brain [18,20,43].

Based on these results, there have been studies in the past assessing the potential of MRSI for radiation treatment planning in GBM patients [16-20,44]. However, very few trials have managed to use MRSI for interventional treatment of brain tumors. SPECTRO-GLIO is one such trial where regions of the brain with a ratio of Cho/NAA > 2.0 received an escalated radiation dose of 72 Gy [45]. This study used a 3D CSI sequence on 1.5T scanners with slices as thick as 25 mm and a nominal voxel size close to 1 cc for high-dose radiation targets. Results of this trial have not yet been reported. We have concurrently been pioneering development of high spatial resolution, 3D echo-planar spectroscopic imaging

(EPSI), MRSI sequences with a full field of view, i.e. including cortical surface regions, which we have termed spectroscopic MRI (sMRI). With sMRI, we can acquire images with more than three-fold improved resolution compared to the 3D CSI sequence used in SPECTRO-GLIO as well as improved signal-to-noise (SNR) due to the use of 3T scanners. Further, we have developed clinical software tools and a web application to facilitate inspection of metabolite overlays and rapid generation of radiation treatment contours in a collaborative manner.

Use of sMRI aids in the more complete delineation of infiltrative GBMs than is possible with standard MRI sequences. Previously, we identified that regions of elevated Cho/NAA, specifically with greater than twice the mean value of Cho/NAA in normal appearing white matter (NAWM) outside of the radiation treatment fields, were later correlated with regions of disease recurrence in 81% of patients [12]. In the same study, samples of tissue with high Cho/NAA abnormality were acquired by surgical biopsies and were stained to measure SRY (sex determining region Y)-box 2 (Sox2), a transcription factor highly correlated with infiltrative tumor. Higher Cho/NAA was strongly correlated to elevated Sox2 density ($p < 0.0001$), even in regions without conventional MRI changes. Thus, targeting high-dose radiation to regions of metabolic abnormality based on sMRI may delay disease recurrence and improve outcomes in patients with GBM.

Based on this premise, we initiated a multi-institutional clinical trial utilizing sMRI to guide radiation dose escalation for newly-diagnosed GBM patients. In this report, we present the initial results of our single-arm pilot study assessing the feasibility, safety and efficacy of this treatment approach with high dose radiation to 75 Gy for this patient population.

2.2 METHODS

This study was performed across three institutions - Emory University (Atlanta, GA), University of Miami (Miami, FL), and the Johns Hopkins University (Baltimore, MD) – and was approved by the institutional review boards of all three institutions. The study was registered with the National Clinical Trials Network (NCT03137888).

2.2.1 Eligibility Criteria

Patients eligible for this study were at least 18 years old, with a newly diagnosed WHO grade IV glioblastoma confirmed pathologically by a board-certified neuropathologist, were able to undergo MRI scans, had a life expectancy ≥ 12 weeks, Karnofsky performance status ≥ 60 [46], had a negative pregnancy test if they were women of childbearing potential, and met the following laboratory criteria within 14 days of registration: white blood cell count ≥ 3000/μL, absolute neutrophil count ≥ 1500/μL, platelet count ≥ 75000/μL, hemoglobin ≥ 9.0 gm/dL, serum glutamic-oxaloacetic acid ≤ 2.0x the upper limit of normal, bilirubin ≤ 2x the upper limit of normal, and creatinine ≤ 1.5 mg/dL.

Exclusion criteria included having pacemakers or other implants that were MRI-incompatible, history of another invasive cancer that was not in complete remission for ≥ 3 years, active infection or other serious medical illness, receiving any other investigational agents, history of prior cranial radiation, or history of prior medical therapies for brain tumors. Once patients were enrolled, they underwent a series of MRI scans as described below. Two additional imaging-based exclusion criteria were implemented: a GBM located in regions known to have increased magnetic susceptibility and poor sMRI signal

(mesial temporal lobe, orbitofrontal cortex, brainstem, or cerebellum), and those with a dose-escalated radiation target (defined by Cho/NAA ≥ 2x normal) greater than 65 cc, in conformity with the NRG Oncology guidelines where dose-escalated targets with maximal dimensions greater than 5cm (corresponding to ~65 cc sphere) were not permitted on the BN001 study [42].

2.2.2 *Image Acquisition*

Enrolled patients underwent standard brain tumor imaging protocols at their treatment institution including T1w-CE and FLAIR sequences. Study-specific sMRI scans were obtained either in the same sessions as the standard sequences or at a separate scheduled session. An echo planar sMRI pulse sequence with GRAPPA parallelization was performed on Siemens 3T scanners at each institution using a 32-channel or 20-channel head and neck coil (echo time [TE] = 50 ms, repetition time [TR] = 1551 ms, flip angle [FA] = 71 degrees) [47-50]. The scan time was 15 minutes with a nominal voxel size of 314 uL, an FOV of 280 mm x 280 mm x 180 mm, and a matrix size of 50x50x18. After post processing, the matrix size is 64x64x32 leading to an interpolated resolution of 4.4 mm x 4.4 mm x 5.6 mm yielding a voxel size of 108 uL. In the same imaging session, a non-contrast T1w MRI with 1mm isotropic voxels was obtained. Data from the sMRI and non-contrast T1w sequences was sent to a centralized location and converted into co-registered spatial-spectral data using the MIDAS software suite (University of Miami, Miami, FL) [51].

2.2.3 Target Generation

A centralized target generation process was implemented as previously described [52]. Briefly, all imaging data obtained at each institution was sent in the DICOM format, and sMRI data sent in the internal format used by MIDAS, to a centralized HIPAA-compliant server hosted by Emory University. A custom-built web platform, the Brain Imaging Collaboration Suite (BrICS), co-registered all the images for each patient into a single coordinate system based on the isotropic T1w MRI space. Metabolite and ratio maps, including Cho/NAA, were interpolated into the high-resolution space and registered and overlaid on anatomic images. The Cho/NAA abnormality index, defined as the fold-increase in Cho/NAA in a voxel compared to the mean in contralateral NAWM, was automatically calculated as previously described to account for scanner and patient variations [12,52]. The BrICS software was used to identify and contour the region with a Cho/NAA $\geq$ 2x normal (**Figure 2.1a**).

During the centralized review process, a board-certified neuroradiologist and two MRS experts and their trainees evaluated the contours and made manual adjustments based on spectral quality and anatomy. The neuroradiologist identified any residual enhancing disease based on T1w-CE imaging, excluding resection cavity or gross blood; the union of residual disease and the Cho/NAA $\geq$ 2x volume was computed and saved as a target known as gross tumor volume 3 (GTV3). Next, two board-certified radiation oncologists, including one from the patient's local institution, reviewed GTV3 and made minor adjustments based on anatomy.

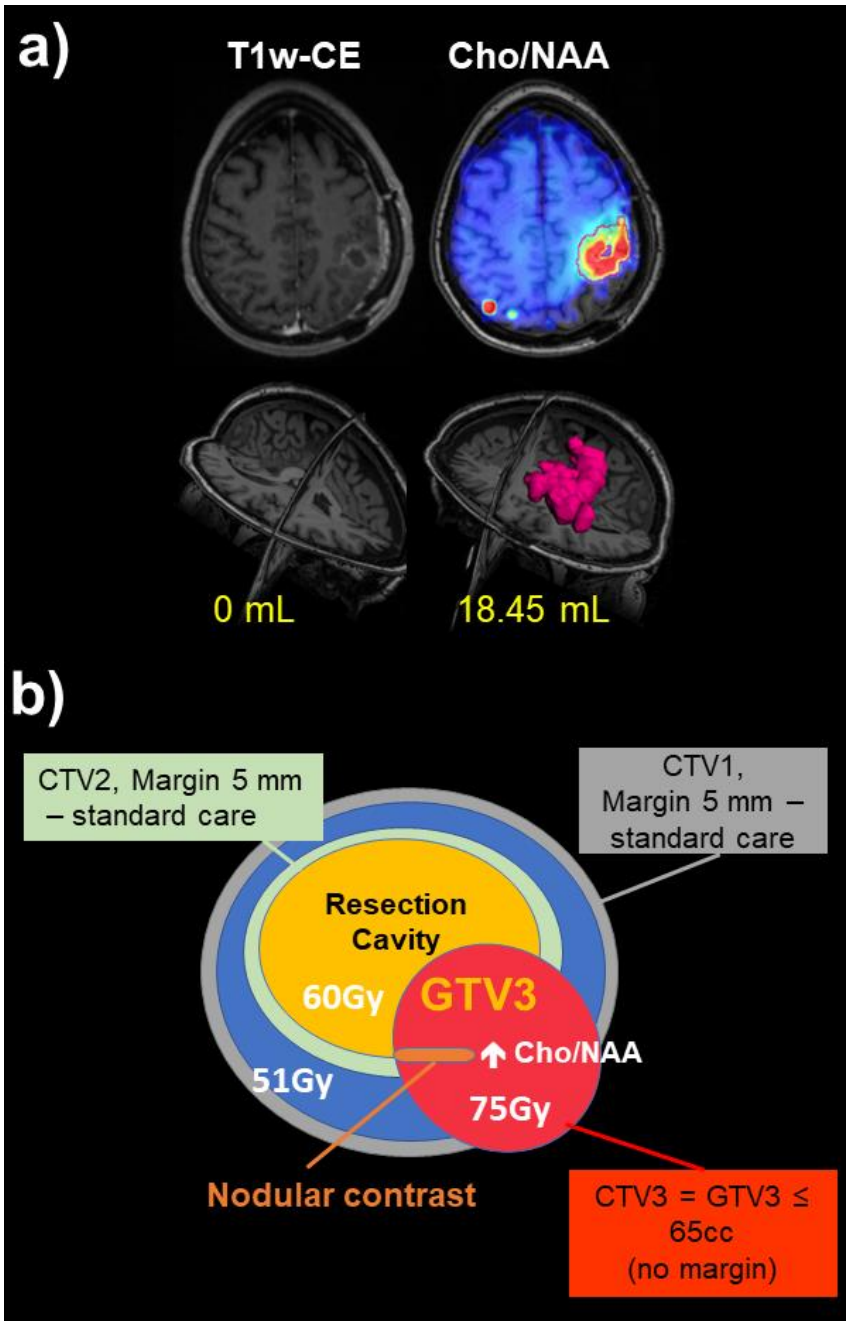

Figure 2.1. (a) Example subject after gross total resection with only expected linear post-operative enhancement around the resection cavity on T1w-CE MRI (left). A contour was generated in BrICS where the Cho/NAA ≥ 2x normal results in a GTV3 volume of 18.45 mL (right). This GTV3 received 75 Gy. (b) Summary of the RT target volumes and doses used in this study. All doses were delivered in 30 fractions of concurrent dose-painted intensity modulated RT.

GTV3 was then exported from BrICS in the DICOM-RT format and imported into the RT contouring/planning system at the local treating institution (Eclipse/VelocityAI, Varian Medical Systems, Palo Alto, CA; MIM, MIM Software, Inc., Beachwood, OH; and Pinnacle, Royal Phillips Electronics N.V., Amsterdam, Netherlands). Our certified medical physicist assessed the GTV3 overlay and ensured accurate registration. Standard gross tumor volume (GTV) targets based on T1w-CE (GTV2) and FLAIR MRI (GTV1) were generated by the local radiation oncology team. A margin of 5mm was added to create clinical tumor volumes (CTV2 and CTV1) to these two targets to account for microscopic invasion of tumor; no CTV margin was added to GTV3 (CTV3=GTV3). **Figure 2.1b** illustrates the three CTV targets and prescribed doses. An additional margin of 3mm was added to each CTV during RT planning to generate planning treatment volumes (PTVs) to which the RT would be delivered. **Figure 2.1a** shows an example patient on study with a large difference in volume between residual contrast enhancement and the Cho/NAA $\geq$ 2x normal. The dose volume histogram of each PTV volume as well as the dose cloud used to treat this patient and PTV contours overlaid on the patient's treatment planning CT are also shown (**Figure 2.2**).

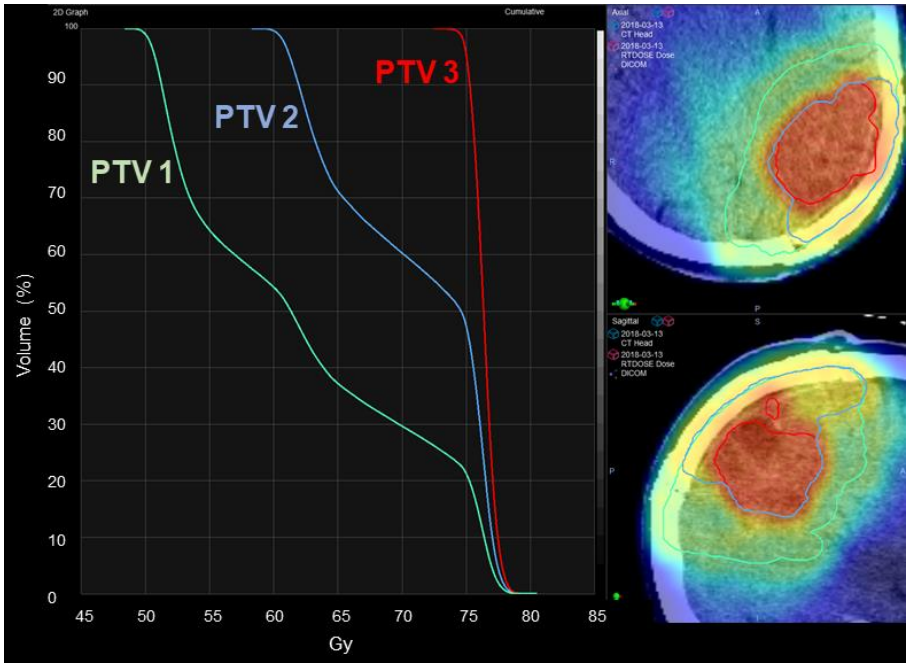

Figure 2.2. For the patient in Figure 2.1, an RT dose-volume histogram is shown on the left for each PTV volume. Overlays of each PTV (PTV1 green line, PTV2 blue line, PTV3 red line) as well as the radiation dose cloud over the patient's treatment planning CT are shown.

2.2.4 Treatment Plan

Patients in this study received RT in 30 fractions using simultaneous integrated boost (SIB) technique with three target volumes over 6 weeks (5 fractions per week), along with concurrent temozolomide (TMZ) at standard-of-care dosing (75 mg/m^2/day, 7 days/week) during RT. Following a one-month rest period after RT, patients continued adjuvant cycles of TMZ (150-200 mg/m^2/day days 1-5 every 28 days) per the standard-of-care as recommended by their treatment team [10]. Due to institutional differences in administering adjuvant TMZ, a minimum of 6 cycles of adjuvant TMZ were administered by each site unless there were signs of tumor progression or toxicity. Neuro-oncologists at each site were given the discretion to treat up to 12 cycles of adjuvant TMZ as long as patients were tolerating the treatment.

2.2.5 Follow-up

Patients were followed at least every three months for two years from the start of RT. Standard MRIs were obtained every 2-3 months unless shorter intervals were clinically indicated. Toxicities were graded according to CTCAE v4.0 and reported to the central clinical trials office from all sites. Progression free survival was assessed through follow-up imaging uploaded to a module within BrICS called the Longitudinal Imaging Tracker (BrICS-LIT) and reviewed by a neuroradiologist and the patient's oncology team [32]. If patients received any follow-up surgeries or biopsies, the pathology reports from those procedures served as the ground truth for tumor progression. If the report indicates that over 20% of sampled specimens contained tumor or that the specimens were positive for tumor (without mention of a percentage), the follow-up date immediately preceding the re-resection/biopsy served as the tumor progression date. There were instances where we could not rely on pathology reports due to patients either not having re-resections or having surgeries much earlier in their follow-up period. In those cases, we would graph CE-T1w and FLAIR lesion volumes, as well as structured reporting scores from the Brain Tumor Reporting and Data System (BT-RADS). BT-RADS is a framework used in over 80% of neuro-radiology reports at Emory University and spreading to institutions such as Johns Hopkins, Duke University, and UCLA [30,53]. By plotting these metrics over the patient's entire post-treatment timeline, we can assess for sudden increases in lesion volumes and structured reporting scores. In cases where structured reporting scores increase to 3c (increasing tumor burden) or 4 (highly suspicious for tumor), then we would overlay radiation dose maps over the co-registered follow-up imaging. If enhancing lesions spreads outside of the GTV3 radiation target, then those cases were marked as the disease

progression date; otherwise, the enhancing lesion was attributed to mainly radiation necrosis. If patients underwent salvage therapies as dictated by the standard-of-care, these were reported to the central clinical trial office. Overall survival was assessed through chart review and direct communication between the oncology team and patients or their families. For patients who left the study to seek care elsewhere, survival follow-up was obtained by communication with their new oncologist whenever possible.

2.2.6 Statistical Analysis

An as-treated analysis was performed for patients who completed the RT protocol. Overall survival from the date of surgery was calculated using the Kaplan-Meier estimator [54] with censoring for events not observed using the *lifelines* survival analysis library written in Python [55]. For this analysis, patients were censored at the date of last clinical contact or date of admission to hospice care if the date of death was not observed. Progression free survival from the surgery date was calculated in a similar manner with censoring for patients who had not yet progressed. Patients who died prior to confirmed tumor progression had their death date marked as their date of event. If there was a gap where interval MRIs were not available with a known date of death, these patients were marked as censored at their time of last MRI.

2.3 RESULTS

2.3.1 Study Participants

The study enrolled patients from September 2017 to June 2019. Enrollment continued until a total of 30 subjects were deemed eligible and completed dose-escalated

RT. A total of 45 patients initially provided informed consent for this study out of which 38 met initial laboratory and clinical eligibility criteria and underwent sMRI scans per the study protocol. Four patients did not meet imaging criteria due to poor quality sMRI scans or having the GTV3 target volume greater than the upper limit of 65cc. Two patients elected to drop out of the study after being deemed eligible but prior to beginning treatment. Of the 32 patients who began RT, two patients opted out of the study during the first two weeks of RT. A total of 30 patients successfully completed the dose-escalated RT according to protocol. The patient enrollment pipeline is shown as a diagram (**Figure 2.3**). Demographics and clinical data of the 30 patients included in this analysis are shown in **Table 2.1**. Mean/Median age was 56.4/58.9 years and sex showed slight male preponderance (19 of 30 patients). 30% (9 of 30) were MGMT hypermethylated and 6.7% (2 of 30) harbored an IDH mutation (IDH1 R132H in both cases). These characteristics are typical of a random cohort of GBM patients and do not appear to skew our cohort towards a more favorable prognosis. It is important to note that since the trial started, the definition of GBM has changed to exclude IDH mutant astrocytomas. If post-surgery T1w-CE lesion volumes were less than 1 cc, we marked the patient as having a gross total resection, otherwise patients were considered to have subtotal resection. Of the 30 patients who completed treatment, 11 had a gross total resection while 19 had a subtotal resection prior to the start of RT. For the 30 treated patients, the median volume of residual enhancement was 1.6 cc (0.0 - 15.4 cc), while the median GTV3, which is the union of residual enhancement and Cho/NAA $\geq$ 2x normal volume was 19.6 cc (0.9 - 65.0 cc).

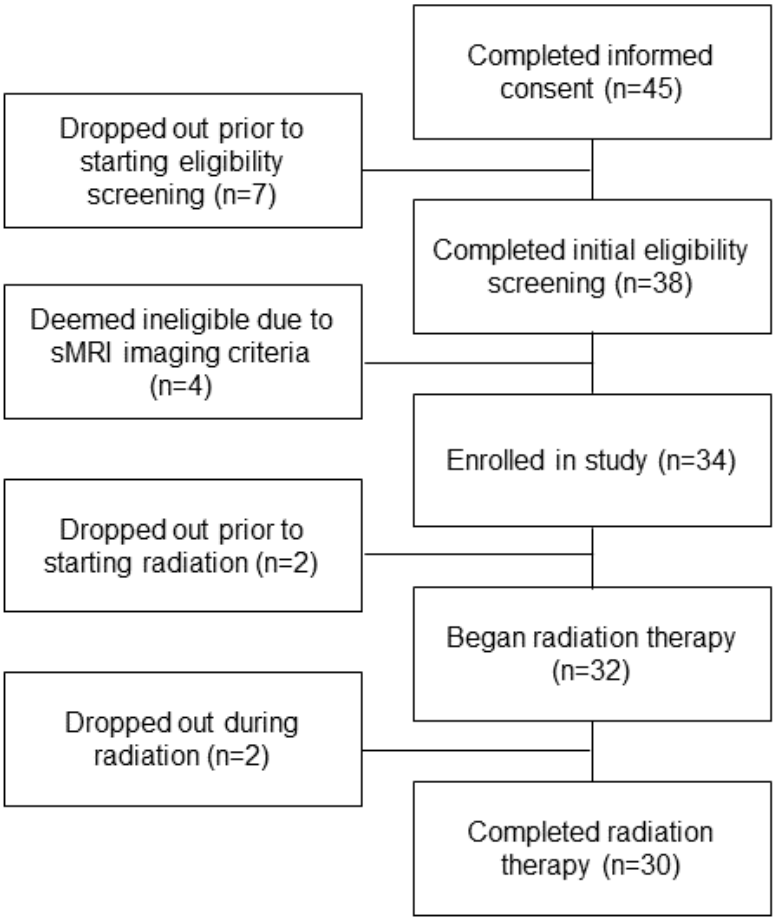

Figure 2.3. Patient enrollment pipeline for this trial.

Table 2.1 Subject Demographics and Clinical Data

	Number of patients (%)
Demographics	
Age	
< 65	23 (77)
≥ 65	7 (23)
Sex	
Female	11 (37)
Male	19 (63)
Genetics	
MGMT Methylation	
Wild-type	22 (73)
Hypermethylated	8 (27)
Not provided	0 (0)
IDH Mutation	
Wild-type	28 (93)
Mutated	2 (7)
Not provided	0 (0)
Pre-RT Surgery	
Gross Total Resection (GTR)	11 (37)
Subtotal Resection (STR)	19 (63)

In **Figure 2.4**, we plotted residual enhancing volume versus GTV3 for every patient on the trial to illustrate just how much larger the treatment volumes were for each patient. Only five patients on the trial had residual enhancing volume after surgery that was larger than 6 cc. It was common to see patients with visible enhancing lesion less than 2 cc and their GTV3 volume be larger than 15 cc due to the larger amounts of visible tumor unearthed via the Cho/NAA maps. Finally, with respect to use of Tumor-Treating Fields

(TTFs), no study patients used TTF as part of their initial management of GBM. Two patients did opt to be treated with TTF at salvage 13-14 months after their initial diagnosis.

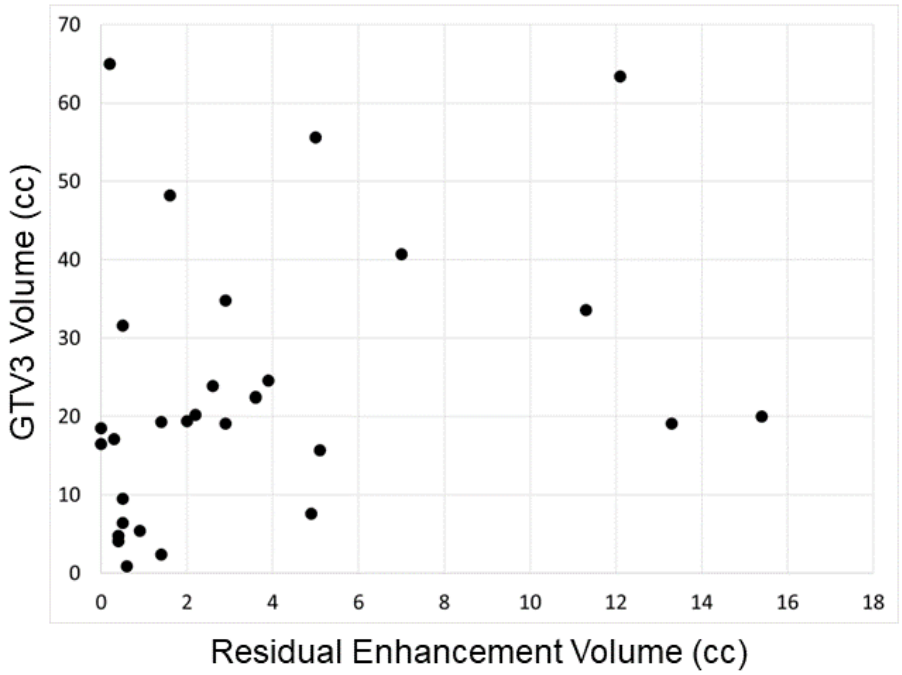

Figure 2.4. Scatter plot of GTV3 volume vs residual T1w-CE volume for each patient on the trial. While there isn't a clear correlation between T1w-CE and GTV3 volume, the GTV3 volume is consistently larger than the T1w-CE volume.

2.3.2 Survival Analysis

At the time of analysis, 16 patients had died. With a median time of 21.4 months to last follow-up for censored patients, the median overall survival (OS) was 23.0 months for the 30 patients that completed our protocol (**Figure 2.5a**). The median progression free survival (PFS) was 16.6 months, with 18 patients being marked as progressed and the remaining 12 patients censored due to either the patient not progressing yet or being lost to follow-up (**Figure 2.5b**).

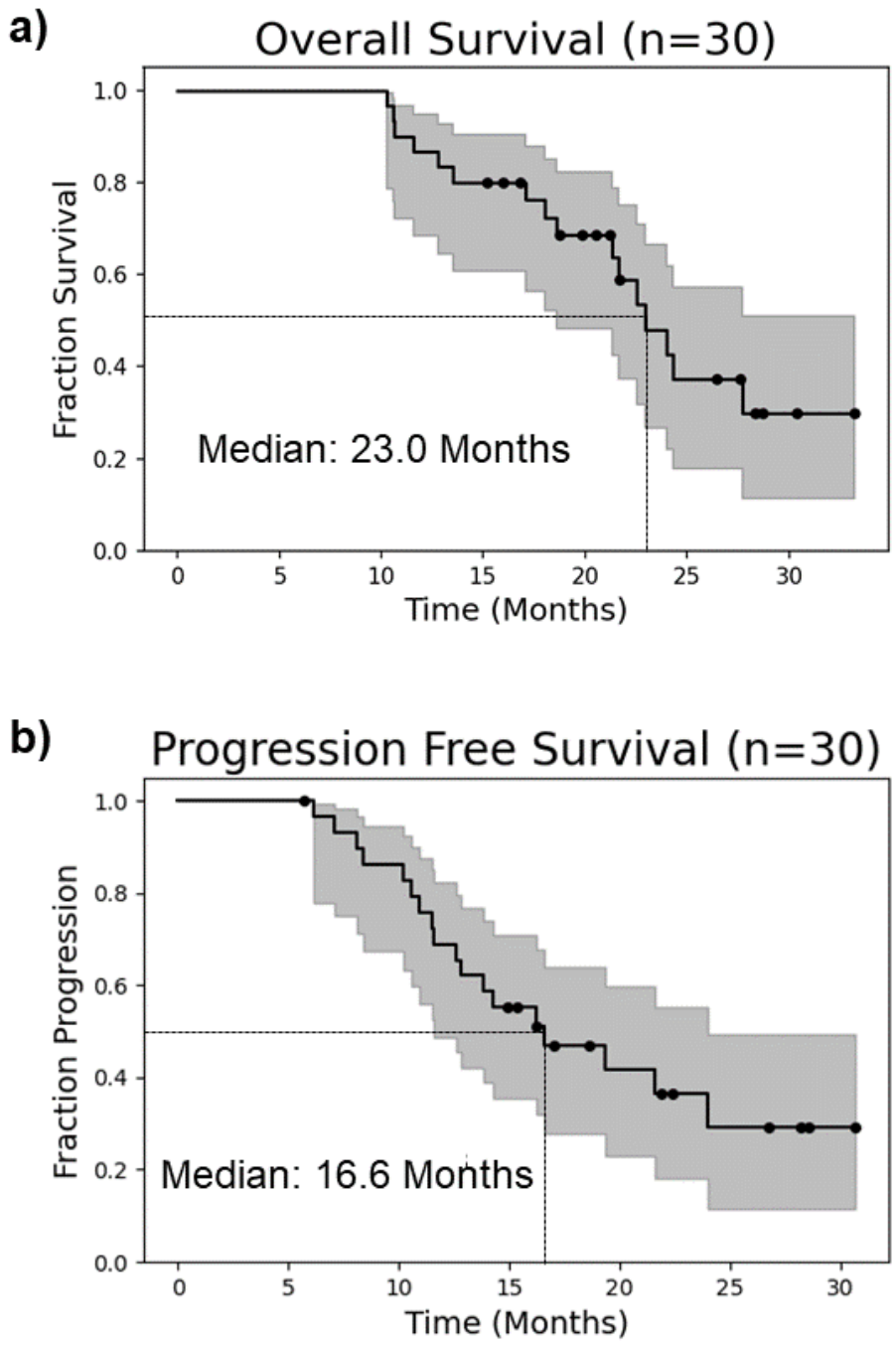

Figure 2.5. Kaplan-Meier estimator for (a) overall survival (OS) with median of 23.0 months and (b) progression free survival (PFS) with median of 16.6 months are shown. 95% confidence intervals are included (grayed out area).

2.3.3 Radiation Treatment Effects

Pseudoprogression is a phenomenon where new or increasing enhancement on T1w-CE MRIs appear to indicate tumor progression, but in fact represents treatment-related changes. This usually occurs early after RT (≤ 3 months) with the enhancing changes eventually subsiding with no alteration in treatment. Radiation necrosis is a phenomenon where tissue within and surrounding regions with malignant glioma experiences a severe reaction to radiation, generally occurring 3-12 months after RT, and is also visualized as new or increasing enhancement on T1w-CE MRIs [56]. In fact, this effect may be indistinguishable from pseudoprogression on MRI except by its timing and can also be termed "late pseudoprogression." We show two examples of these phenomena where pathologic confirmation was obtained (**Figure 2.6**). In Case #1, residual enhancement was noted at one-month post-RT (**Figure 2.6a**) with further increases over the ensuing four months (**Figure 2.6b**) indicating possible refractory tumor or pseudoprogression. Repeat resection was performed with histologic confirmation that the residual enhancement was, in fact, 100% necrosis, suggesting a treatment-induced response (**Figure 2.6c**). In Case #2, standard MRI appears to show recurrence eight months after completion of RT (**Figure 2.6d-e**). However, a repeat resection showed that the enhancing tissue was nearly all (99%) necrosis (**Figure 2.6f**). Due to the longer time after completion of RT, the enhancing lesion in the second case was called radiation necrosis. Because pathologic confirmation was not obtained in all cases of possible pseudoprogression and/or radiation necrosis, accurate assessment of true progression and progression free survival (PFS) was difficult to precisely determine. In this initial report,

we do present PFS, but plan to report the methodology of determining progression in more depth in a later report based on more detailed dose-response and local control analyses.

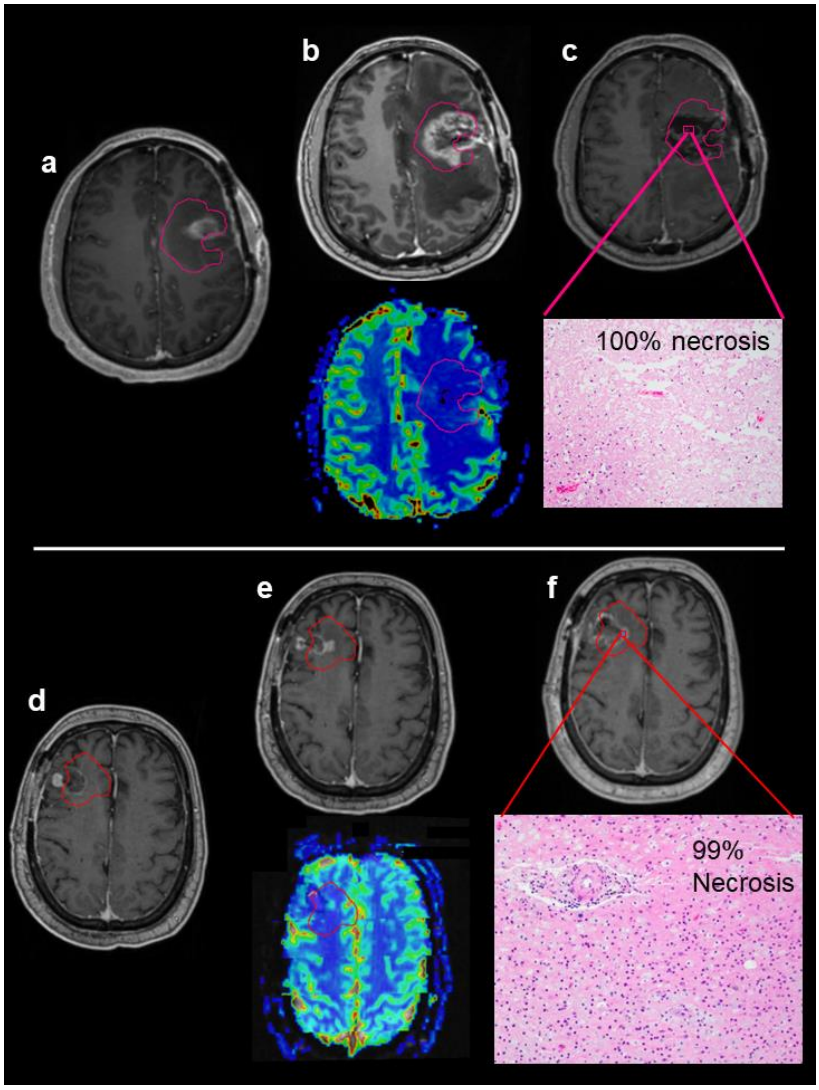

Figure 2.6. Examples of two cases with "late pseudoprogression," or radiation necrosis are shown. [**Case #1**] (a) At 1-month post-RT, residual enhancement is seen on T1w MRI within the pink PTV3 contour. (b) At 5 months post-RT, residual enhancement has increased, but the relative cerebral blood volume (rCBV) map on dynamic susceptibility contrast (DSC) perfusion MRI shows minimal to no perfusion. (c) Repeat resection demonstrated 100% necrosis on H&E-stained sections. [**Case #2**] (d) At 1-month post-RT, there is primarily linear, post-operative enhancement on T1w-CE MRI within the red PTV3 contour. (e) At 8 months post-RT, increasing enhancement is seen at periphery of cavity. The DSC perfusion MRI again shows no definitive hyperperfusion. (f) Repeat resection again found predominantly (99%) necrosis on H&E-stained sections.

2.3.4 Toxicity

Of the 30 patients who received dose-escalated RT, 11 patients experienced grade 3 or greater toxicity that was judged to be at least possibly attributed to their treatment. Of the 30 grade 3 or higher toxicities reported, 13 were thought to be at least possibly related to treatment. Five grade 3 toxicities occurred during adjuvant TMZ and were believed to be due mainly to TMZ rather than radiation. Three grade 3 toxicities occurred during the follow-up phase at least 1 year after RT. The three remaining grade 3 toxicities and two grade 4 toxicities occurred during RT/concurrent TMZ consisted of thrombocytopenia (2 cases), neutropenia, increased LFTs, and generalized weakness, with all except one case attributed to TMZ. As is evident by the listing of grade 3 or greater toxicities for our study cohort (**Table 2.2**), the majority of these toxicities were judged to be related to TMZ rather than dose-escalated RT.

Table 2.2. Grade 3 or Greater Toxicities At Least Possibly Due to Therapy

Category	**Grade 3**		**Grade 4**	
	No.	**%**	**No.**	**%**
Thrombocytopenia	4	13.3	1	3.3
Neutropenia	0		1	3.3
Transaminitis	1	3.3	0	
Hypokalemia	1	3.3	0	
Muscle weakness	2	6.7	0	
Fatigue	1	3.3	0	
Headaches	1	3.3	0	

2.4 DISCUSSION

GBM is a highly aggressive brain tumor with patients having a relatively poor median OS of only 16 months with standard therapies. While radiation can improve survival outcomes for patients with GBM, we hypothesize that dose-escalated radiation guided by Cho/NAA maps may further improve OS by treating a much larger extent of infiltrating, non-enhancing tumor. While other trials such as SPECTRO-GLIO attempted to similarly administer high-dose radiation based on the Cho/NAA ratio, we used an sMRI sequence that acquired images at a higher resolution, better SNR, and improved brain coverage. With that, our goal was to create a clinically translatable treatment pipeline from image acquisition to generation of high-dose radiation targets that could be inspected and assessed in a collaborative manner. Towards this goal, we demonstrate the clinical feasibility and early outcomes of sMRI-guided, dose-escalated radiation treatment for GBM. The volumetric sMRI acquisition had a scan time of 15 minutes and fit seamlessly with other clinical scans. Only 3 patients on our trial were excluded from starting treatment due to poor sMRI signal quality from patient motion. We are now developing the next version of the sequence with motion correction to overcome this issue. Raw data from the sMRI scan was transferred and processed before metabolite heat maps were generated in BrICS for visual assessment and contour generation. Clinicians and researchers from remote sites were easily able to login to BrICS and generate GTV3 treatment volumes collaboratively in real-time, as well as manually edit the contours per physician's discretion. With a turnaround time of 1.5 days from scan time to upload of GTV3 to standard RT planning systems [52], our workflow fit effortlessly into standard clinical procedures.

With a significantly larger volume of brain tissue also receiving a higher radiation dose, patient toxicity reports were carefully assessed for any negative responses to treatment. Of the 17 grade 3 or higher toxicities that occurred in 11 patients, all but one toxicity was attributed to TMZ, with the other toxicity being attributed to a combination of RT and TMZ. In the NRG-BN001 study, 229 patients were enrolled in the photon comparison randomized in a 1:2 fashion with treatment consisting of standard versus dose-escalated RT. The arm receiving dose-escalated RT, had a 75 Gy radiation dose administered to residual enhancement (including the resection cavity), while our trial used the union of Cho/NAA $\geq$ 2x and residual enhancement as the GTV3 target volume receiving 75 Gy. Preliminary findings from the BN001 study found no significant difference in grade 3 toxicity between patients who received dose-escalated RT and those who received standard RT [42], supporting our assertion that overall toxicity was not excessive.

Not unexpectedly, we did identify instances of radiation necrosis that were confirmed pathologically. However, symptoms were well managed with steroids, when necessary, and did not result in serious toxicities prior to their repeat resections. An optimal treatment plan for patients will always be a balance between increasing tumor control while minimizing potential risks of toxicity. While we are likely to see a slightly higher incidence of radiation necrosis with a dose-escalated RT treatment regimen, both our current results and the preliminary results of NRG-BN001, suggest that a radiation dose of 75 Gy in 30 fractions to a select volume for GBM patients is tolerable overall despite an increased necrosis risk. We hypothesize that the escalated dose used on NRG-BN001 that focused only on the resection cavity and contrast enhancing residual may have been of lesser benefit

since it is less likely to target the full extent of tumor compared to our sMRI-guided contours.

2.5 CONCLUSION

Ultimately, our goal in this study was to demonstrate the clinical feasibility of utilizing Cho/NAA ≥ 2x normal to guide radiation dose escalation in newly-diagnosed GBM patients. Through software suites and web applications like MIDAS and BrICS, we were able to generate GTV3 treatment volumes in a rapid manner with collaborative decision making among multisite investigators. Median OS in this study was 23.0 months with an appropriate toxicity profile, which compared favorably to 16 months for standard therapies [6,38,39]. Preliminary results from the NRG-BN001 study show a median OS of 18.7 months for dose-escalated patients and 16.3 months for patients on standard treatment. The improved specificity at identifying infiltrative tumor by utilizing sMRI has led to a median OS that is potentially longer than even the high-dose treatment arm in NRG-BN001, albeit with a sample size that is smaller. We have also determined a median PFS of 16.6 months, which is significantly longer than previously reported and even approaches median OS with standard therapies [6]. Based on these promising results, a randomized phase II trial is in development within ECOG-ACRIN (EAF211) that seeks to more definitively determine the efficacy of sMRI-guided dose-escalated RT.

Chapter 3. Spectroscopic MRI-Based Biomarkers Predict Survival for Newly Diagnosed Glioblastoma in a Clinical Trial

3.1 INTRODUCTION

Glioblastoma is the most common malignant primary brain tumor in need of novel treatment strategies due to its poor prognosis [10]. Despite improvements in the standard of care for glioblastoma patients, it is challenging to identify the extent of tumor infiltration with T1-weighted contrast-enhanced (T1w-CE) MRI and T2-weighted fluid-attenuated inversion recovery (FLAIR) MRI which are currently used to determine the targets of radiation therapy [14]. Glioblastomas are characterized by a compromised blood-brain barrier and leaky vasculature, which can be identified by a gadolinium-based contrast agent in T1w-CE scans. FLAIR is used to identify tumor, edema, inflammation, and radiation effects but is not specific to tumor [15,57]. The combination of imaging methods may not identify the full extent of tumor infiltration, resulting in undertreatment during radiation therapy. The standard of care radiation therapy target is the residual contrast enhancing contour and resection cavity treated with 60 Gy with a lower dose to the surrounding FLAIR abnormality [41]. Temozolomide is given concurrently during and after radiation. This treatment results in a median overall survival (OS) of 16 months and median progression-free survival (PFS) of 4-7 months in historical cohorts [10,40,58].

To better identify infiltrative tumors for treatment targeting, members of our group have been developing a whole-brain, high resolution, 3D echo-planar magnetic resonance spectroscopic imaging (MRSI) sequence that we have termed “spectroscopic MRI” (sMRI) [47-50]. Tumor cell metabolism differs from healthy brain tissue metabolism in that there

are increased choline and reduced N-acetylaspartate levels in proliferating tumor cells. The ratio of choline to N-acetylaspartate (Cho/NAA) has been shown to be a highly specific tumor biomarker by image-histology correlation studies and predated tumor recurrence patterns [12].

We recently reported results from a multisite clinical study (NCT03137888) where 30 newly diagnosed glioblastoma patients were treated with escalated dose radiation (75 Gy) guided by the Cho/NAA abnormality on spectroscopic MRI. This treatment paradigm resulted in a median OS of 23.0 months and PFS of 16.6 months, a significant improvement from patients treated with standard of care radiation therapy dosing [21].

In this report, we perform a retrospective analysis of the data from our previously mentioned clinical study. We aim to assess spectroscopic MRI-based biomarkers of patient OS and PFS. Because historical results show that extent of resection (EOR) and residual contrast-enhancing volume are factors that correlate with survival, we hypothesize that incorporating metabolic information from spectroscopic MRI will better predict survival outcomes. More specifically, we predict that patients with more residual spectroscopic abnormality will have worse survival outcomes. We tested this using the Kaplan-Meier estimator for predicting PFS and OS and analyzed the difference in survival distributions based on the residual contrast-enhancing and spectroscopic MRI-based volumes.

3.2 METHODS

3.2.1 Description of tumor volume determination/target generation

Patients enrolled in this study had pathologically confirmed newly diagnosed World Health Organization (WHO) grade IV glioblastoma, which at the time of enrollment included isocitrate dehydrogenase (IDH) mutant patients. In 2021, the WHO definition of grade IV glioblastoma excluded IDH mutants [59]. In accordance with the updated definition, we performed our analysis excluding the two IDH mutant patients (n=28). Further trial details including patient selection and sample selection, as well as initial outcome results for all 30 enrolled patients, have been previously reported [21]. The patients in this study provided informed consent for participation according to the institutional review board at each participating institution, and each institutional review board approved this study. After surgical resection and prior to beginning radiation therapy, a spectroscopic MRI was acquired in addition to standard MRI (T1w-CE and FLAIR MRIs). Spectroscopic MRIs were acquired on Siemens 3T scanners at each institution with an echo planar spectroscopic imaging pulse sequence with GRAPPA parallelization. Either a 20- or 32-channel head and neck coil was used with TE = 50 ms, TR = 1551 ms, and FA = 71° [21]. Scans were processed and registered to anatomic T1 MRIs for each patient before radiation treatment planning [51,60-63].

Pre-resection scans were obtained 0-18 days before surgery, and post-resection scans were obtained approximately 3-4 weeks after surgery and 1 week prior to the radiation therapy start date. For treatment planning, the contrast-enhancing regions of the pre-resection T1w-CE including necrotic centers were contoured. The residual postcontrast enhancement (rENH) tumor volume was semi-automatically generated on the Brain Imaging Collaboration Suite using the previously reported method by contouring only the contrast-enhancing regions of the T1w-CE scan for each patient inside of FLAIR envelope,

excluding the resection cavity [52,64]. All rENH volumes were checked and, if necessary, edited by a board certified neuroradiologist. The Brain Imaging Collaboration Suite also automatically generated a spectroscopic MRI contour for Cho/NAA ≥ 2x, which was then manually edited by site MRS experts based on spectral quality. The gross tumor volume 3 (GTV3) was calculated for each patient by combining the rENH volume with the Cho/NAA ≥ 2x volume to determine the escalated dose target. The GTV3 contours were inspected and approved by two board-certified radiation oncologists (one of them was the treating physician). This workflow was published in Gurbani et al. [52].

Briefly, for each patient enrolled, radiation treatment contours were guided by standard MRIs and spectroscopic MRI data as follows: FLAIR abnormal regions of the brain received 50.1 Gy of radiation, the resection cavity received 60 Gy, and the GTV3 contour received a boosted 75 Gy of radiation [52]. After completing radiation therapy, imaging was acquired every 2-3 months as per standard practice. This follow-up imaging was used to determine PFS, and OS was determined through chart review and communication between patients, their families, their oncology team, and published obituaries [21]. In this report, OS and PFS were calculated as of 17 months after completing enrollment of the last patient.

In **Figure 3.1**, an example patient from the completed clinical trial is shown. This patient had a gross total resection (GTR) with no residual enhancing tumor. For this patient, standard of care would have used the resection cavity with a margin for high-dose radiation (60 Gy). This figure demonstrates how even when using a 20 mm margin, some abnormal tissue in the GTV3 volume detected by spectroscopic MRI is left out. Further, most clinical

practices use a margin between 5 and 10 mm, which would have left out significant tumor that spectroscopic MRI can detect. It is important to note that the Dice similarity coefficients in the figure show how much of the cavity + margins overlap with the GTV3 contour. In addition, using large, homogeneous margins can lead to unnecessary treatment of healthy tissue with high-dose radiation. We calculated the percentages of volumes that would be outside of the GTV3 contour. For a 5, 10, and 20 mm expansion beyond the cavity, 41.3%, 49.7%, and 74.9% of each volume would fall beyond the GTV3 volume, respectively. While there is some overlap between standard of care high-dose targets and our GTV3 target, a target guided by spectroscopic MRI illustrates metabolically active tumors undetected by T1w-CE.

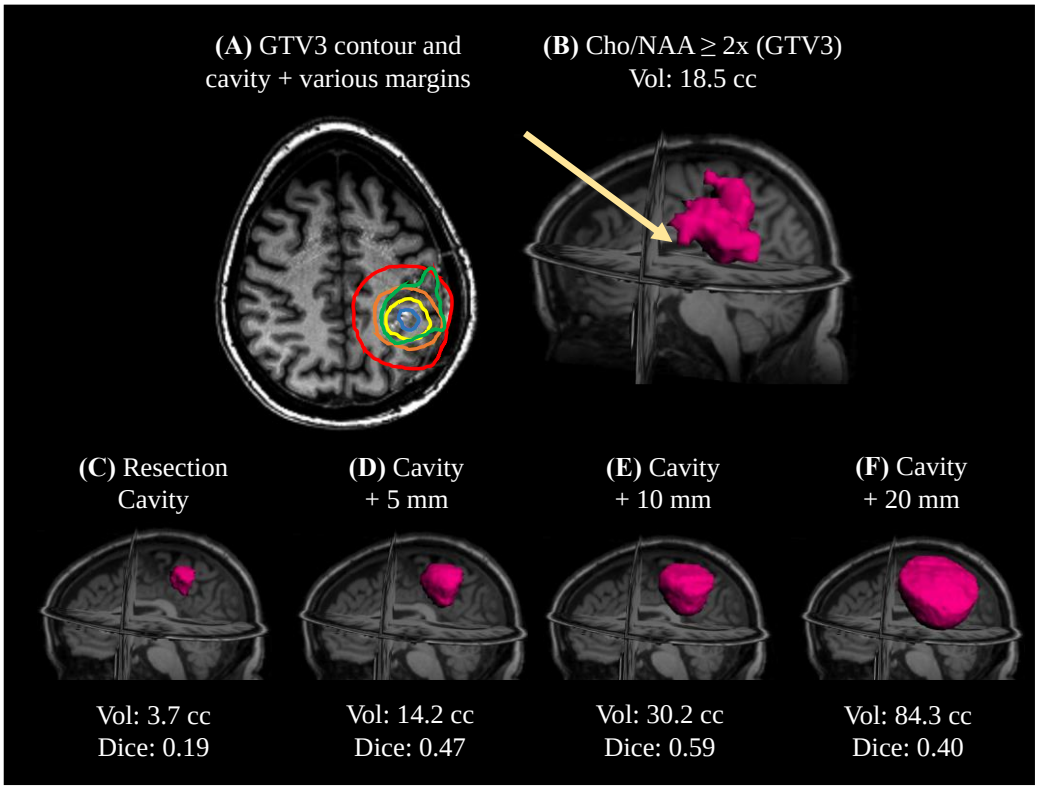

Figure 3.1. A comparison of an example gross tumor volume 3 (GTV3) treatment volume to the resection cavity with standard of care margins. Due to no residual enhancing tumor, standard of care would involve treating the cavity with a margin. (A) An axial view of the

GTV3 contour (green) that extends past the resection cavity (blue), resection cavity with 5 mm margin (yellow), 10 mm margin (orange), and 20 mm margin (red). (B) This 3D view of the GTV3 contour shows a small amount of infiltrating tumor (arrow) that extends even past the 20 mm margin. (C-E) 3D views of the resection cavity with various margins and volumes calculated. A Dice overlap score was calculated between each margin and GTV3. For (C), (D), (E), and (F), the Dice scores were 0.18, 0.47, 0.59, and 0.40, respectively. The percentages of volumes in (C), (D), (E), and (F) which are not included in (B) were 37.4%, 41.3%, 49.7%, and 74.9% respectively.

In **Figure 3.2**, two subjects are shown, where Case 2 is the same patient shown in **Figure 3.1**. The vast difference in rENH and GTV3 contour volumes for the two subjects is shown here, particularly in Case 2 where the volume of residual enhancement was 0 cc. Both contours are also rendered in 3D to emphasize the spatial differences between the rENH and GTV3 contours.

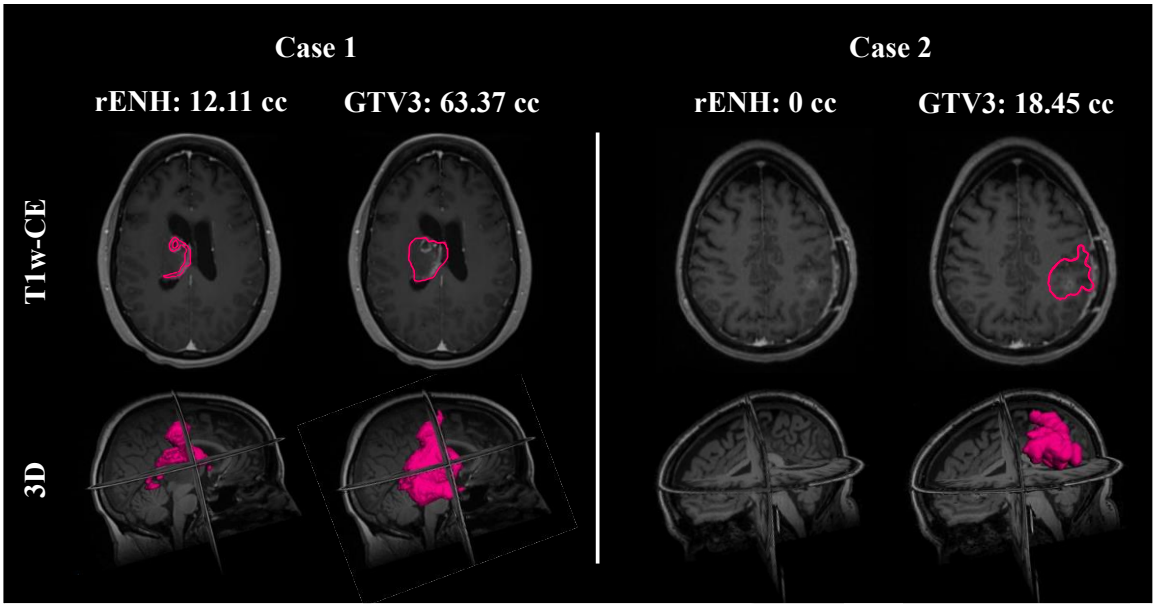

Figure 3.2. Two sample cases are shown. In the first case, the first column shows the residual postcontrast enhancement (rENH) contour with a volume of 12.11 cc, overlaid on the T1-weighted contrast-enhanced (T1w-CE) MRI (first row) for a 54-year-old female glioblastoma patient. The second column shows the gross tumor volume 3 (GTV3) contour over 5 times larger than rENH with a volume of 63.37 cc. The second row is a three-dimensional rendering of both contour volumes overlaid on a T1 precontrast image. In the

second case of a 56-year-old female glioblastoma patient, there is no residual contrast enhancement visible on the T1w-CE MRI, whereas the GTV3 volume is 18.45 cc.

3.2.2 Surgical resection classification

EOR was calculated based on the percent change between the pre-operative contrast-enhancing tumor volume and the rENH volume. When EOR $\geq$ 95%, the surgery was classified as gross total resection (GTR), while an EOR < 95% was considered subtotal resection (STR), excluding biopsy. A secondary method of surgical resection classification was also used, in which resection was classified as GTR if the rENH volume was $\leq$ 1.5 cc or STR if > 1.5 cc. Surgery classification by EOR and rENH volume was used to compare the 28 patients considered in this analysis to patients in large historical cohorts [6,38,65].

3.2.3 Statistical analysis/survival analysis

The Kaplan-Meier estimator was used to calculate survival curves based on OS and PFS, with survival measured as the time between surgical resection for each patient and their recorded OS and PFS dates [54]. Patients were first stratified into two groups using median rENH and median GTV3 volumes. Each Kaplan-Meier curve was compared using a log-rank test to determine differences between patients with rENH volumes greater than and less than the median rENH volume, and patients with GTV3 volumes greater than and less than the median GTV3 volume with regards to OS and PFS. Linear regression was performed and the associated R^2 value was used to determine any correlation between the rENH and GTV3 volumes, which would confound any comparisons. Statistical analysis was conducted using the Python lifelines analysis library [55]. The secondary analysis performed in this report was approved by the institutional review boards at each institution.

3.3 RESULTS

Of the 30 patients included in the original study, 2 had IDH mutations (IDH1 R132H) and 9 were MGMT hypermethylated. As reported previously, 16 patients had died with a median OS of 23.0 months [21]. Excluding the 2 IDH mutant patients, the median time to follow-up for censored patients was 22.4 months (5.7 – 30.1 months) and the median PFS was 16.2 months, as shown on a Kaplan-Meier curve in **Figure 3.3**. The median age for the 28 patients was 59.3 years with a range of 38.1 – 71.6 years (minimum – maximum) and there were 10 females and 18 males. Without the two IDH mutant patients, the median OS becomes 21.6 months and the median PFS becomes 16.2 months.

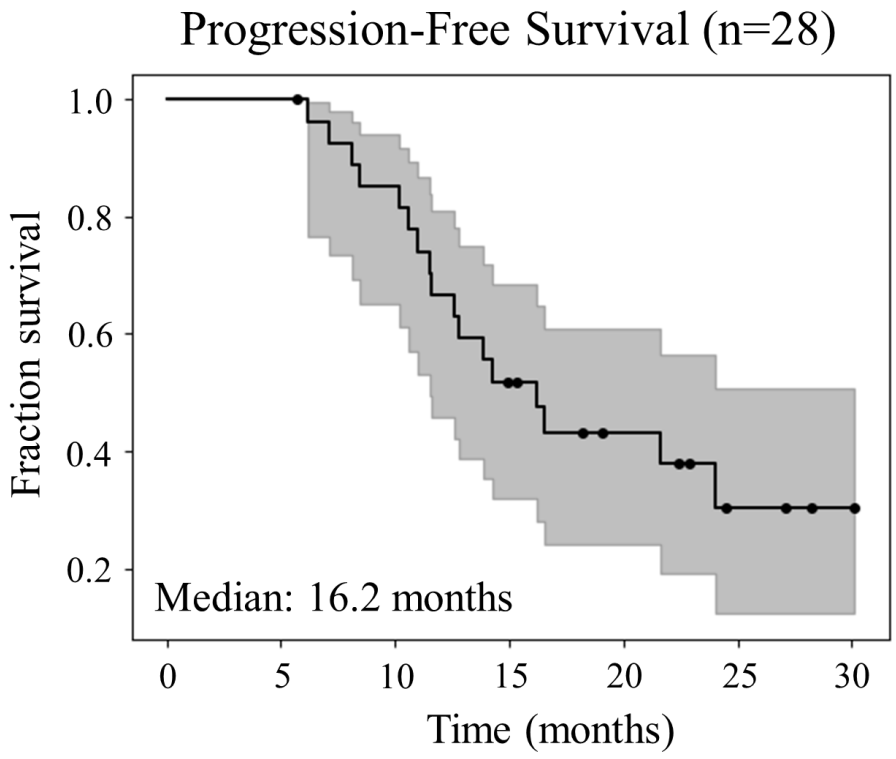

Figure 3.3. Kaplan-Meier survival curve of progression-free survival (PFS) for the 28 IDH wild type patients included in this analysis. The median PFS is 16.2 months and median time to follow-up is 22.4 months.

The volume of high-risk disease remaining should be a predictor of survival outcomes for glioblastoma patients. EOR or rENH are classic ways to identify the amount of high-risk disease and have been shown in multiple previous studies to be correlated with both OS and PFS. 12 of 28 patients in our cohort had GTR (defined by either EOR ≥ 95% or rENH ≤ 1.5cc), shown in **Table 3.1**. Using this cutoff (GTR versus less than GTR), we did not find a significant difference in survival outcomes. However, pre-treatment spectroscopic MRI scans present the opportunity to apply additional criteria for identifying high-risk disease that may be superior to rENH alone.

Table 3.1. Classification of all 28 patients based on extent of resection (EOR) and residual postcontrast enhancement (rENH) volume.

	Classification	**Number (%) of patients**
EOR	GTR (EOR ≥ 95%)	12 (42.9%)
	STR (EOR < 95%)	11 (39.3%)
rENH	GTR (rENH ≤ 1.5 cc)	13 (46.4%)
	STR (rENH > 1.5 cc)	15 (53.6%)

On our pilot study, GTV3 volume was hypothesized to provide a better representation of residual high-risk disease than rENH alone. For our cohort, median rENH was 2.1 cc (range: 0.0 – 15.4 cc) and median GTV3 was 19.2 cc (range: 0.9 – 65.0 cc). The GTV3 volumes were always greater than rENH volumes (median of 8.2 times larger). In

Figure 3.4, a scatterplot of rENH vs GTV3 volumes for each patient indicates a low correlation between the volumes (R^2=0.127, p=0.063).

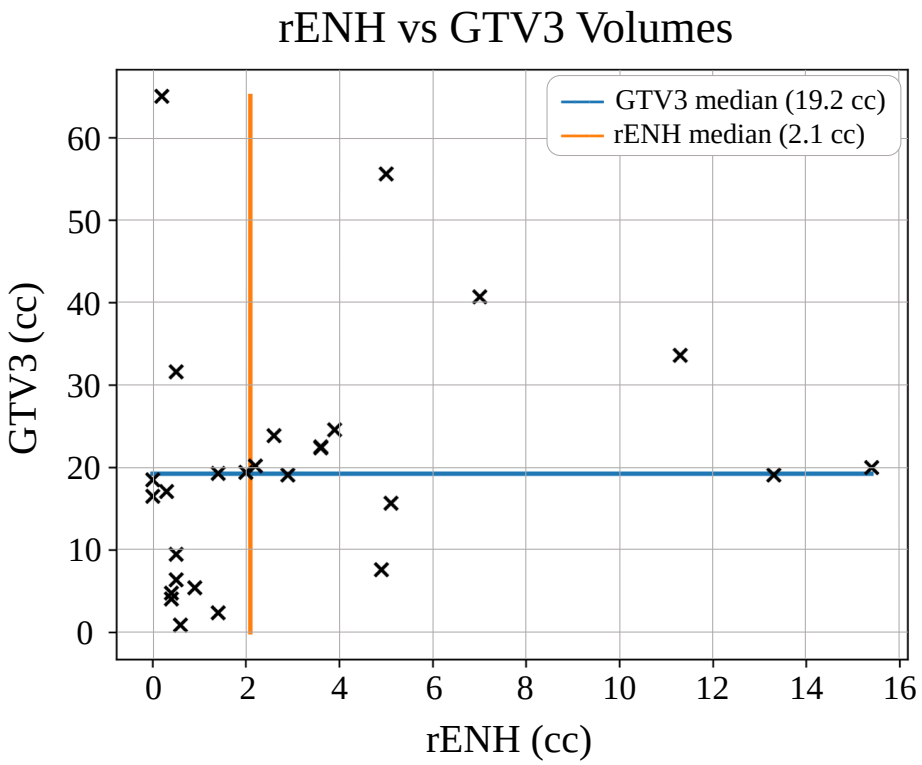

Figure 3.4. Gross tumor volume 3 (GTV3) and residual postcontrast enhancement (rENH) plot indicating low correlation between the two volumes based on R^2=0.127 (p=0.063). The horizontal blue line indicates the median GTV3 volume (19.2 cc), and the vertical orange line indicates the median rENH volume (2.1 cc).

Figure 3.5 shows Kaplan-Meier curves for OS and PFS using the rENH and GTV3 volumes as predictive markers. **Figures 3.5A and 3.5B** show Kaplan-Meier curves for OS. In **Figure 3.5A**, the 28 patients are stratified by those with an rENH volume below and above the median (2.1 cc). Similarly, in **Figure 3.5B**, the 28 patients are stratified by those with a GTV3 volume below and above the median (19.2 cc). The difference in medians for the groups stratified by rENH is 1.7 months (p=0.373), while the difference in medians for

the groups stratified by GTV3 is 10.3 months (p=0.020), indicating that GTV3 volume is a significant biomarker of OS. For patients with rENH < 2.1 cc, the median OS was 23.0 months; for rENH > 2.1 cc, the median OS was 21.3 months. For patients with GTV3 < 19.2 cc, the median OS was 23.0 months; for GTV3 > 19.2 cc, the median OS was 17.1 months.

Figures 3.5C and 3.5D show Kaplan-Meier curves for PFS using the same predictive markers as the OS graphs. The difference in medians for the groups stratified by rENH is 6.2 months shown in **Figure 3.5C** (p=0.286), while the difference in medians for the groups stratified by GTV3 is 11.4 months shown in **Figure 3.5D** (p=0.019), indicating that GTV3 volume is a better predictive marker for PFS. For patients with rENH < 2.1 cc, the median PFS was 19.0 months; for rENH > 2.1 cc, the median PFS was 12.8 months. For patients with GTV3 < 19.2 cc, median PFS was 24.0 months; for GTV3 > 19.2 cc, the median PFS was 12.6 months.

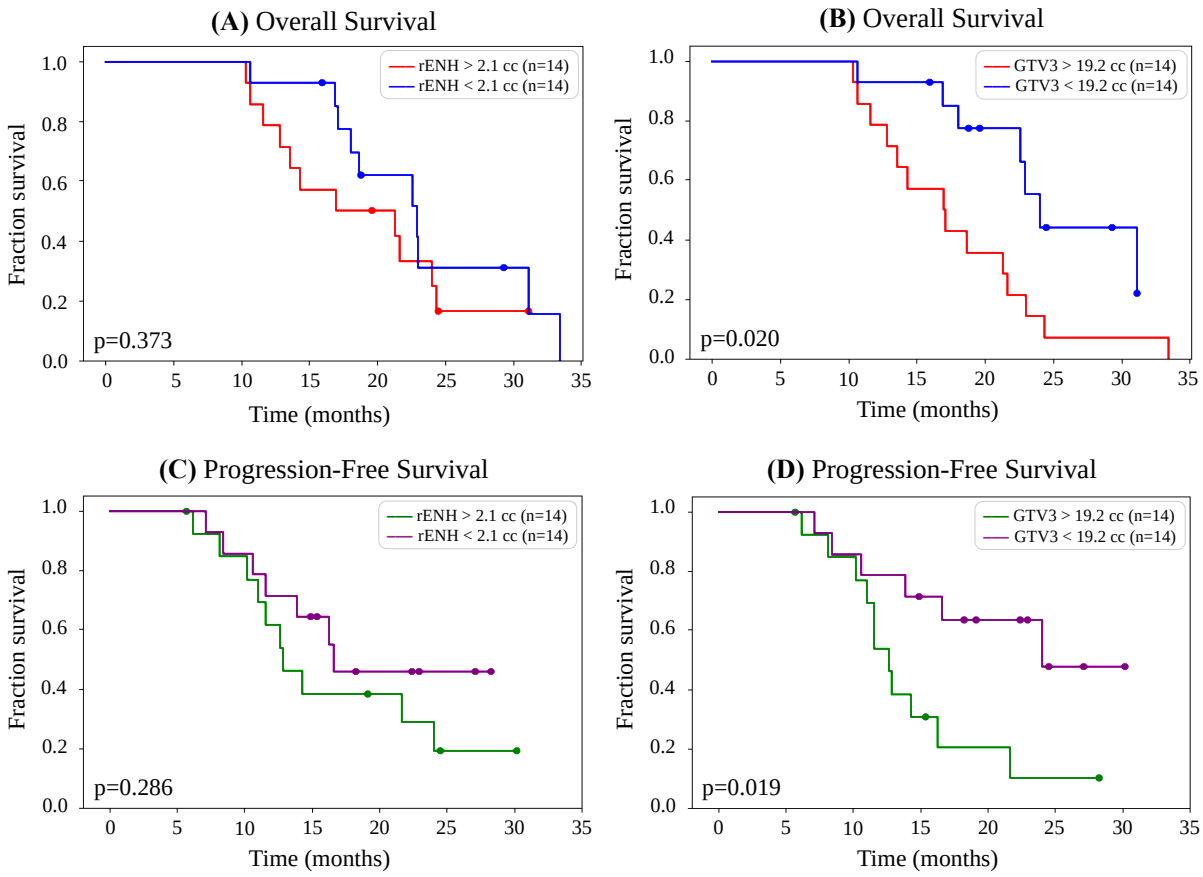

Figure 3.5. (A) Kaplan-Meier survival curve for overall survival (OS) stratified into equal groups by the median residual contrast enhancing (rENH) tumor volume (2.1 cc). The median OS for patients with rENH > 2.1 cc is 21.3 months, and the median for OS for patients with rENH < 2.1 cc is 23.0 months. (B) Kaplan-Meier survival curve for OS stratified into equal groups by the median gross tumor volume 3 (GTV3) (19.2 cc). The median OS for patients with GTV3 > 19.2 cc is 17.1 months, and the median OS for patients with GTV3 < 19.2 cc is 23.0 months. (C) Kaplan-Meier survival curve for progression free survival (PFS) stratified into equal groups by the median rENH tumor volume (2.1 cc). The median PFS for patients with rENH > 2.1 cc is 12.8 months, and the median PFS for patients with rENH < 2.1 cc is 19.0 months. (D) Kaplan-Meier survival curve for PFS stratified into equal groups by the median GTV3 (19.2 cc). The median PFS for patients with GTV3 > 19.2 cc is 12.6 months, and the median PFS for patients with GTV3 < 19.2 cc is 24.0 months.

3.4 DISCUSSION

In this paper, we have used data from a clinical trial using spectroscopic MRI to guide dose escalation therapy to glioblastoma to assess the relationship between rENH tumor, metabolically active tumor as detected by spectroscopic MRI, and survival outcomes (PFS and OS) to determine if residual spectroscopically abnormal tumor (GTV3) was a biomarker for survival. For every subject, the rENH volume was smaller than residual non-enhancing tumor that was detected using spectroscopy, since GTV3 contains both residual enhancing tumor and non-enhancing metabolically active tumor. Additionally, there was low correlation between GTV3 and rENH volumes (R^2=0.127). The lack of a linear relationship between the volumes is further supported by the insignificant p-value (p=0.063).

The amount of residual spectroscopically abnormal tumor, as measured by the GTV3 volume, was a statistically significant biomarker for both OS (p=0.020) and PFS (p=0.019). We hypothesize that these results are attributed to the metabolically active tumor within the GTV3 volume that is not accounted for in the rENH volume. The large gap and lack of crossover between the GTV3-stratified Kaplan-Meier curves suggest that GTV3 is a better indicator of OS and PFS than rENH in this patient cohort. For this reason, GTV3 may be a better predictor of PFS and OS because it more accurately reflects how much non-infiltrating tumor is left post-resection. It also provides more precise targeting compared to adding a 1-2 cm margin around the resection cavity for the high dose target, allowing high radiation doses to be used with decreased risk of damaging healthy tissue. Unlike prior studies, there was no relationship between rENH and survival or EOR and survival [12]. This result may be attributed to the relatively low amounts of residual contrast-enhancing

tumor on most patients in this study due to aggressive resection or higher radiation doses given to these regions.

For this study, the EOR classified using rENH volume (using a threshold of 1.5 cc) or EOR percentage (using a threshold of 95%) was similar to large historical cohorts such as RTOG 0825 (637 patients), AVAGlio (921 patients), and EF-14 (695 patients) [6,38,65]. A 2005-2010 study of 128 patients from Cleveland Clinic reported a similar distribution based on rENH and EOR [66]. Their study resulted in a median survival of 16 months for patients with rENH $\leq$ 1.5 cc and a median survival between 14 and 15 months for patients with EOR $\geq$ 95%. Spectroscopic MRI-guided dose-escalation resulted in a median survival of 23 months for patients with rENH $\leq$ 1.5 cc and a median survival of 27 months for patients with EOR $\geq$ 95%, which are more favorable outcomes. Similar studies have been previously reported, often with factors such as GTR versus STR, diffusion, or other volumes. Haj et al. perform a survival analysis between patients that received GTR versus STR [67]. They identified a 4-month difference in OS (GTR = 18.5 months, STR = 14.5 months) and a 1.6-month difference in PFS (GTR = 9.4 months, STR = 7.8 months). Awad et al. performed a survival analysis using only EOR and a combination of EOR and pre-resection contrast enhancing volume [68]. Their EOR-only comparison failed to identify a relationship with survival outcomes; however, their EOR/pre-resection contrast enhancing volume comparison was identified as a significant predictor of patient survival. Compared to the studies mentioned above, the number of patients in our trial is smaller and a larger study is warranted for fairer comparisons.

Limitations of this analysis include the relatively small cohort size, a treatment paradigm which was not clinical standard of care, and data from only 3 clinical sites. More data is needed to determine if the amount of spectroscopically abnormal residual tumor after resection continues to have this predictive effect in larger patient groups, but this preliminary data is supportive of further study of using the extent of metabolically abnormal tissue to predict patient outcomes.

3.5 CONCLUSION

Due to the infiltrative nature of glioblastoma, T1w-CE and FLAIR MRIs may not optimally characterize the extent of tumor, resulting in undertreatment during radiation therapy. Our goal was to use data from a previously performed clinical trial to determine how spectroscopic MRI-based biomarkers predicted PFS and OS for patients in the trial. In this group, the volume of spectroscopically abnormal tissue (GTV3) was a statistically significant biomarker of both OS and PFS and performed superior to the extent of resection and residual enhancing tumor. The results of this analysis support using spectroscopic MRI to guide high-dose radiation and suggest that the non-enhancing component of glioblastoma is an important biomarker of survival and should be treated accordingly.

Chapter 4. The Longitudinal Imaging Tracker (BrICS-LIT): a cloud platform for monitoring treatment response in glioblastoma patients

4.1 INTRODUCTION

Glioblastoma (GBM) is the most aggressive primary brain tumor in adults, with a two-year survival around 17% [69]. The standard of care includes surgical resection followed by high-dose radiation therapy (RT) and chemotherapy [6,40]. Despite these aggressive therapies, median progression free survival remains 5-7 months post-chemoradiation [58]. After initial chemoradiation, patient monitoring is guided by standard MR imaging performed at routine intervals, typically 2-3 months, to monitor disease progression. However, there is often considerable overlap between treatment effects and tumor progression in follow-up imaging, making it difficult to discern post-treatment radiation effects (pseudoprogression) from true progression [23,24]. Lack of quantitative longitudinal tracking hinders appropriate clinical decision making and slows the development of new treatments. A quantitative system that quantifies patient condition post-treatment has the potential to guide management decisions, improve patient outcomes, reduce treatment cost, and validate novel treatment strategies.

Disease specific structured reporting attempts to reduce variability in clinical imaging results by implementing pre-defined outcome categories, well-defined imaging criteria, and standardized language [25,26]. Such a framework has been implemented in the monitoring of disease in other organ systems including breast imaging (BI-RADS), neck imaging (NI-RADS), and prostate imaging (PI-RADS) [27,70,71]. In particular, the BI-

RADS framework has found considerable success in decreasing interobserver variability and predicting malignancy for patients with suspicious lesions in the breast [28,29]. The poor prognosis associated with brain tumors raises the stakes for clear and accurate radiology reporting, as there may be limited opportunities to make changes in clinical management. Further, the desire to standardize assessment of brain tumor response has been discussed extensively for several years. The FDA, along with organizations such as the Brain Tumor Imaging Standardization Committee and National Cancer Institute (NCI) have reached a consensus in the past that although overall survival (OS) is the current gold standard for determining treatment efficacy, a structured framework is necessary for "the accuracy of determining true response to a particular therapy" [72]. Multiple response criteria have been developed to assess brain tumors, including the Levin, World Health Organization (WHO), MacDonald, and the Response Assessment in Neuro-Oncology (RANO) criteria. Although RANO is widely used in the research setting, it has not yet achieved wide clinical adoption in radiology reports because of complex interpretation criteria, need for multiple manual measurements, high inter-observer variability, and limited understanding among practicing physicians [73-77].

Clinicians at Emory University developed the Brain Tumor Reporting and Data System (BT-RADS) to address some of the clinical hurdles that previous reporting systems face [30,53,78]. The BT-RADS framework involves multiple metrics to generate a disease score, including volumetric measurements based on contrast enhanced T1 weighted (CE-T1w) MRIs and T2-weighted fluid-attenuation inversion recovery (FLAIR) MRIs. While BT-RADS has grown in popularity at Emory and other institutions, physicians need timesaving, accurate metrics to assist with scoring and objectivity. In order to assist

physicians with implementing BT-RADS into standard clinical workflows, we developed a web application known as the Longitudinal Imaging Tracker (LIT). LIT is built as a module on top of our previously described platform, the Brain Imaging Collaboration Suite (BrICS) [52]. Within LIT, clinicians can simultaneously view T2 FLAIR and CE-T1w MRIs for up to five timepoints and scroll through slices of each volume together. Images are automatically co-registered and interpolated to allow for easier visualization and tracking. LIT is also designed to interact with REDCap databases [79] using an API to retrieve de-identified metadata that are relevant to BT-RADS scoring. Further, LIT contains semi-automated segmentation algorithms to calculate lesion volumes in both T2 FLAIR and CE-T1w MRIs. Incorporating such algorithms and visualization features could lead to more objective and less variable volumetric assessments, improve adoption of the BT-RADS structured reporting system for monitoring GBM, and generate sensitive metrics to discern tumoral recurrence in clinical and research settings. We plan on using LIT to assess the efficacy of an interventional pilot study where metabolic abnormalities, detected by spectroscopic MRI, were used to guide a boosted RT dose in patients with GBM (NCT03137888) [80]. In this paper, we describe the architecture and features that LIT offers as well as demonstrate its potential in monitoring GBM patients after initial treatment through example cases from our clinical trial that has recently completed accrual.

4.2 METHODS

4.2.1 Software Architecture

To implement BT-RADS criteria in an objective fashion, we developed a new module for our BrICS web-based imaging platform called the Longitudinal Imaging

Tracker (LIT) [52]. LIT consists of a server-side module that handles image processing and storage, and a frontend user interface. The LIT backend uses C++ and PHP scripting languages that leverage the Insight Toolkit's (ITK) image processing library [81,82]. Many of LIT's algorithms such as segmentation, registration, interpolation, and interconversion of images between DICOM and other formats use ITK's well-established library. LIT also leverages many of the inherent advantages of BrICS, including a lightweight browser client with a JavaScript frontend, which ensures that medical staff do not need to download any additional software to use it, a feature of key importance in clinical practice where installation of standalone applications is undesirable.

Users can import CE-T1w and FLAIR DICOM images, which are then automatically co-registered using 3D versor rigid registration, and aligned using trilinear interpolation [83]. Users can select five different time points and observe changes in FLAIR abnormality or CE-T1w enhancement (**Figure 4.1**) as well as overlay radiation dose clouds (**Figure 4.2**). While the module helps users visualize patient images for longitudinal tracking, segmentation algorithms are necessary to quantitatively report imaging abnormalities. With LIT, users can easily monitor changes in imaging at a three-dimensional level rather than simply using representative 2-D slices, which would improve objectivity when assessing a patient's overall disease-state [84,85].

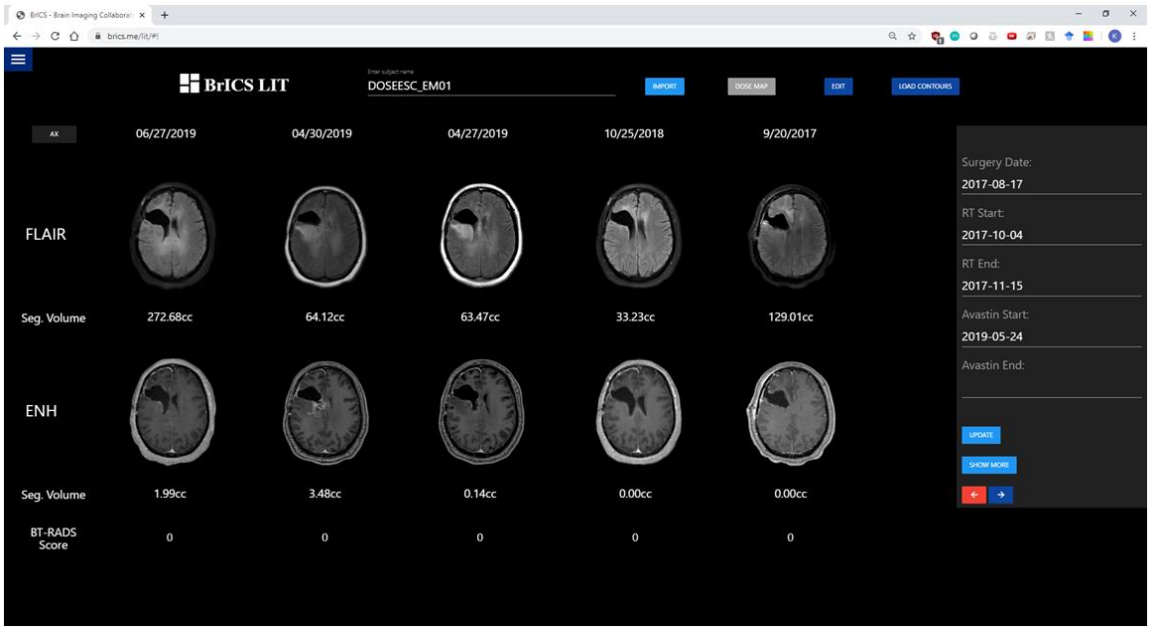

Figure 4.1. An example GBM patient enrolled in our dose escalation trial at Emory site. Follow-up images are displayed from the earliest date on the far right (pre-RT) to the most recent date on the left. T2 FLAIR (top row) and CE-T1w MRIs (bottom row) are co-registered and interpolated to allow for simultaneous scrolling through all slices.

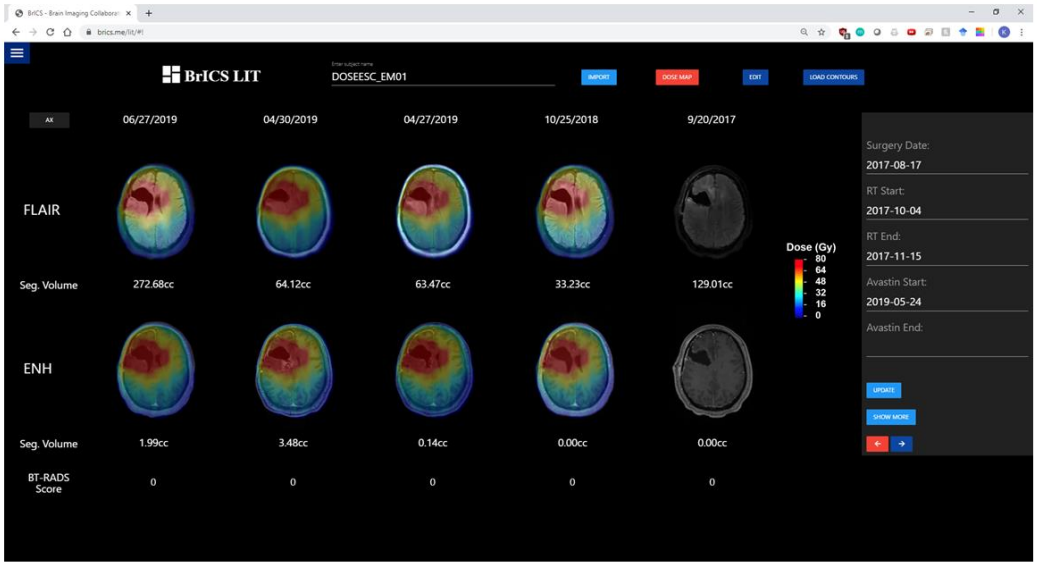

Figure 4.2. The same patient from Figure 1 with their radiation planning dose map overlaid. The MRIs on the far right do not have radiation overlaid as that visit preceded the start of radiation treatment.

4.2.2 Semi-Automated Segmentation of Lesion

To allow for volumetric tracking of brain tumors, we developed segmentation algorithms for T2 FLAIR and CE-T1w MRIs. Current iterations of these tools are semi-automated as they require initial (manual) seeding by the user, but the eventual goal is to implement automated tools which do not require user intervention. A schematic of the CE-T1w segmentation is shown in **Figure 4.3a-d**. The segmentation tool requires a user to select a representative "seed" in the image within the lesion of interest. Next, Otsu thresholding, an approach where thresholds are iteratively applied to cluster voxel intensities by minimizing the intra-cluster variance, was applied to the image [86]. The image, with intensities now separated into four clusters, is then registered to an atlas and the skull removed through a skull stripping algorithm [87]. A region growing algorithm starting from the user input seed is applied to identify connected components sharing the specified Otsu cluster. The binary image goes through a series of morphological filtering techniques to remove blood vessels and choroid plexus, and to smooth out spurs along the tumor edge [88,89].

We also developed a semi-automated FLAIR segmentation algorithm which focuses on increasing spatial contrast to homogenize intensities within FLAIR boundaries and excluding connected components extraneous to the lesion. Much like the CE-T1w algorithm, the FLAIR algorithm requires a user to first select a representative "seed" within the lesion of interest **(Figure 4.3e-g)** after which a curvature flow algorithm is applied to "blur" the image and effectively increase spatial contrast [90]. The algorithm then applies a series of ITK filters to dilate and fill holes within clusters of voxels sharing similar

intensities. After these preprocessing steps, Otsu thresholding is applied to cluster the image voxels into four classes. A region growing algorithm is then applied from the user input "seed" to segment connected components sharing the specified Otsu threshold. Both algorithms take <15 seconds to perform their respective segmentations and do not require any additional imaging for segmentation of lesion.

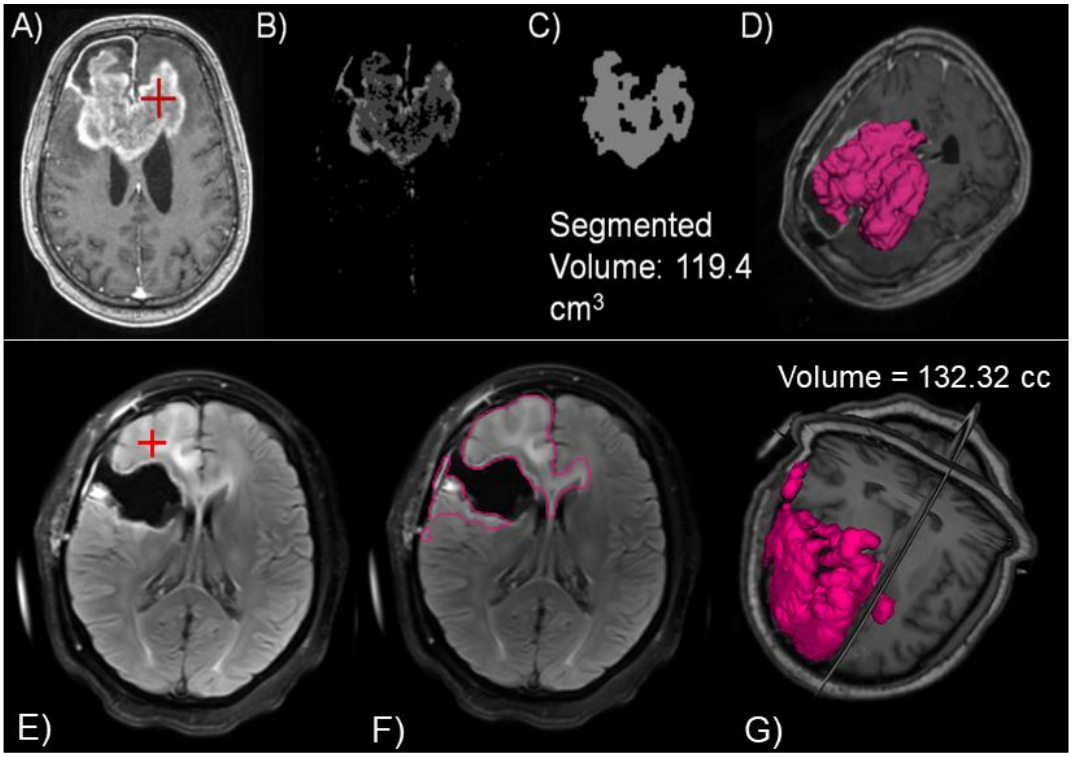

Figure 4.3. For the semi-automated CE-T1w segmentation, (A) a clinician must place a seed in the region of interest. (B) Otsu thresholding and filtering identifies extent of enhancement. (C) Indicates the segmented contour for a representative slice after region growing. (D) The entire volume of segmented lesion. The FLAIR segmentation also requires (E) users to make a seed within the hyperintense region. (F) After smoothing, thresholding, and region growing the contour has segmented the extent of hyperintensity. (G) A volumetric representation of FLAIR hyperintensity for this patient.

BrICS-LIT has also been designed to allow for new segmentation algorithms to be easily incorporated – eventually allowing users to choose the best segmentation algorithm in a case-by-case basis.

4.2.3 Visualization and Manual Editing

While our segmentation algorithms save physicians considerable time in calculating the size of lesions, we realize the value in providing rapid, manual editing tools for segmented volumes that can easily be incorporated in clinical workflows. Therefore, even if the segmentation algorithms are not perfect, they can provide a good, rapidly-obtained starting point; the LIT interfaces provides tools for users to then edit these segmentations. A digital audit trail tracks any changes that are made.

We use a Javascript library known as the Web Graphics Library (WebGL) to render images in our web application. Overlaid contours, dose clouds, and co-registered MRIs all utilize this API for visualization. While all imaging including contours are saved on our server as DICOM datasets, they are converted to PNG textures that WebGL uses for rendering. Clinicians can view contours overlaid on clinical MRIs to observe lesion volume changes over time. Users can also overlay radiation dose maps to determine the spatial similarity between regions of abnormality and regions of treatment.

4.2.4 BT-RADS Scoring and REDCap Integration

In addition to volumetric measurements of tumor, the BT-RADS's framework also incorporates additional clinical criteria such as timing of surgery and radiation, use of medications which can affect imaging appearance (such as Avastin and steroids), and worsening clinical condition, which are important in assessing disease recurrence [53]. These criteria are typically identified by chart review by the clinician; we seek to streamline the incorporation of this information and calculation of BT-RADS scores. Since LIT itself is not HIPAA compliant, it uses a pipeline to retrieve de-identified clinical information

from a HIPAA compliant REDCap database. REDCap is a secure database system that is currently used by thousands of institutions and over one million users for secure and convenient storage of patient information in clinical trial settings [79]. Using a PHP API, LIT connects to pre-specified REDCap databases and retrieves clinical information that are relevant for BT-RADS scoring (**Figure 4.4**). With REDCap integration, LIT can interface with several REDCap databases for brain tumors.

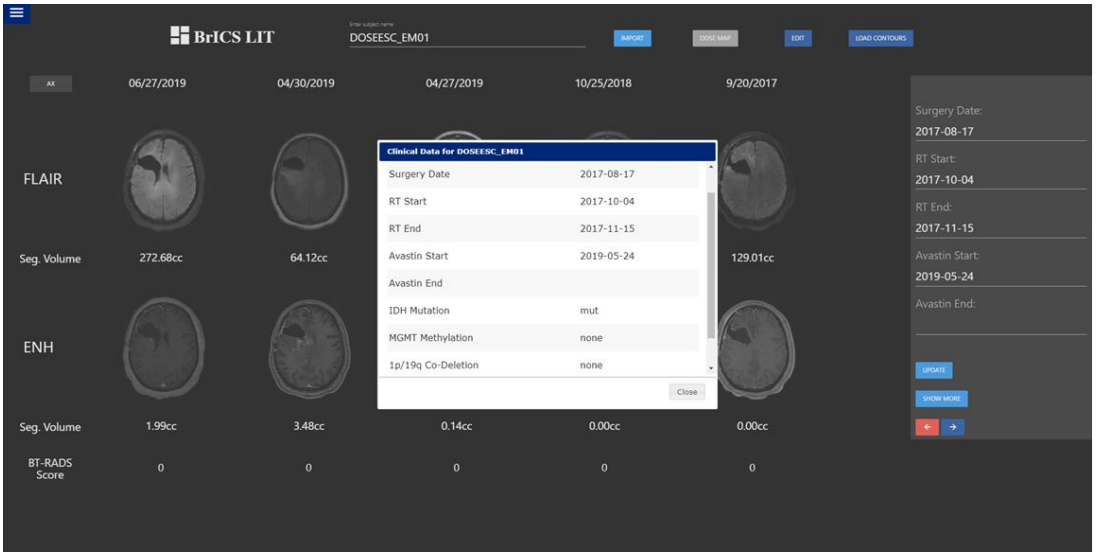

Figure 4.4. Clinicians and researchers can open a window within LIT that displays relevant clinical and genomic data automatically retrieved from a REDCap database that can assist in BT-RADS scoring.

4.3 RESULTS

Follow-up imaging and clinical data are collected for patients on the GBM dose escalation clinical trial. BrICS-LIT is also being used to assess follow-ups from a pilot study treating patients with melanoma brain metastases with stereotactic radiosurgery (SRS) and immunotherapy.

In **Figure 4.5**, follow-up images from a GBM patient enrolled in our dose escalation trial at Johns Hopkins have been uploaded into LIT, with contoured lesions displayed and BT-RADS scores assigned by a neuroradiologist. The images on the far right represent the baseline and occurred shortly after the patient's surgery but before starting their radiation treatment. The patient has minimal contrast enhancement (2.02cc) and some FLAIR hyperintensity (43.85cc) and was assigned a score of 0 (baseline scan). From the baseline through the next two follow-up dates, the volume of abnormal FLAIR and contrast enhancement continues to increase, leading to assigned BT-RADS scores of 3A (imaging worsening, but favor treatment effect) and 3C (imaging worsening, but favor tumor progression). The first follow-up was given a score of 3A because while the imaging had worsened, that follow-up occurred shortly after completion of radiation treatment. Therefore, the clinician suggested the increase in lesion volume is largely due to treatment effects (pseudoprogression) rather than true progression. Between dates 12/28 and 01/02, the patient's lesion volume in both types of MR images subsequently decreased. The fact that this decrease occurred over such a short period of time lead clinicians to believe the patient was possibly medicated with either Avastin or steroids, and the patient therefore received a score of 1B. This was confirmed by a treating neuro-oncologist that the patient was treated by high dose steroid. The decrease in lesion volume between these two dates would be particularly difficult for clinicians to discern if they simply picked one representative slice and made measurements or manually inspected all the slices for both images. Depending on the slice chosen and the subjective opinion of the interpreting radiologist, two clinicians could have made different conclusions about the patient's disease-state between those two dates. The semi-automated software that BrICS-LIT offers

can avoid discrepancies in clinical interpretation by calculating lesion volume in a precise manner.

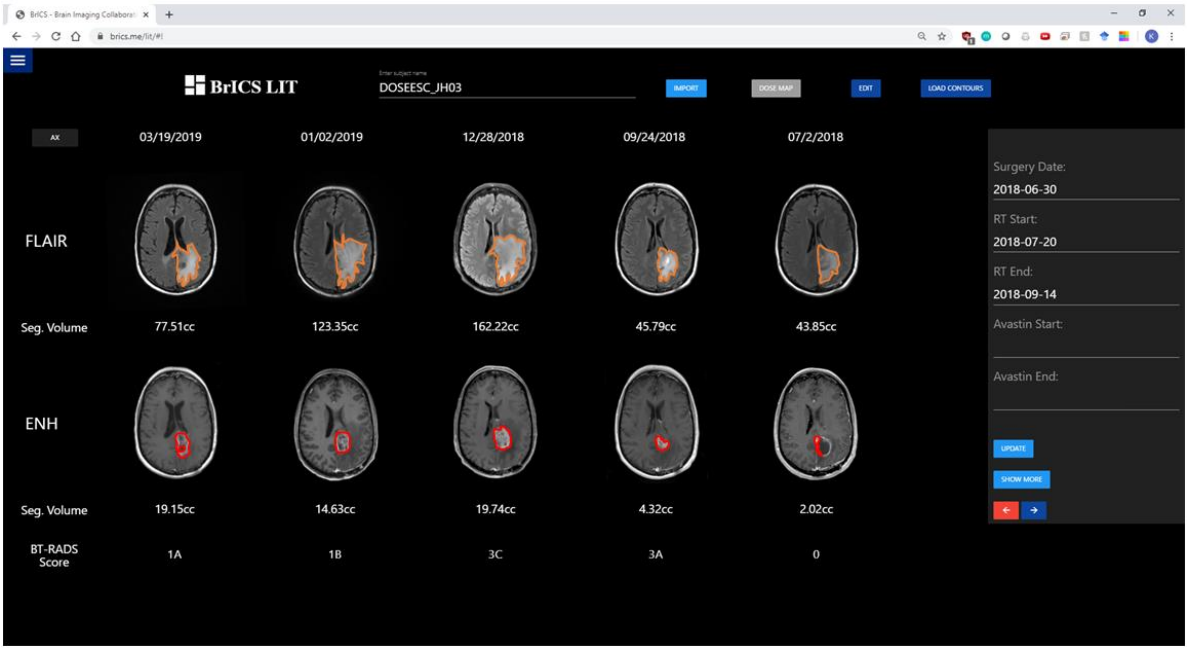

Figure 4.5. An example Johns Hopkins GBM patient with follow-up imaging co-registered and ready to view in BrICS-LIT. Contours have been generated semi-automatically with respective volumes of lesion calculated. A neuroradiologist used the segmented volumes, along with REDCap data on the right panel to assign BT-RADS scores for each visit date.

Another example where BrICS-LIT can provide insights is in **Figure 4.6**. This patient, from the University of Miami, received radiation treatment starting on 6/25/2018 for 6 weeks. Every follow-up image except for the pre-RT baseline has a radiation dose map overlaid. By overlaying a dose cloud for every follow-up, clinicians can determine whether lesions are spreading outside of radiation treatment zones or whether new lesions are forming in areas that received lower doses of radiation. The patient received a high dose of radiation (75 Gy in 30 fractions prescription dose per the clinical trial) in the left occipital lobe where there was significant contrast enhancement and FLAIR abnormality

at the time of initial radiation treatment. However, on 1/29/2019, a new contrast enhancing lesion appears in the left frontal lobe along with significant FLAIR abnormality, a sure sign of recurrence as the lesion is outside the tissue which received a significant radiation dose. This increases physician confidence that this is truly disease progression and not a delayed effect of radiation.

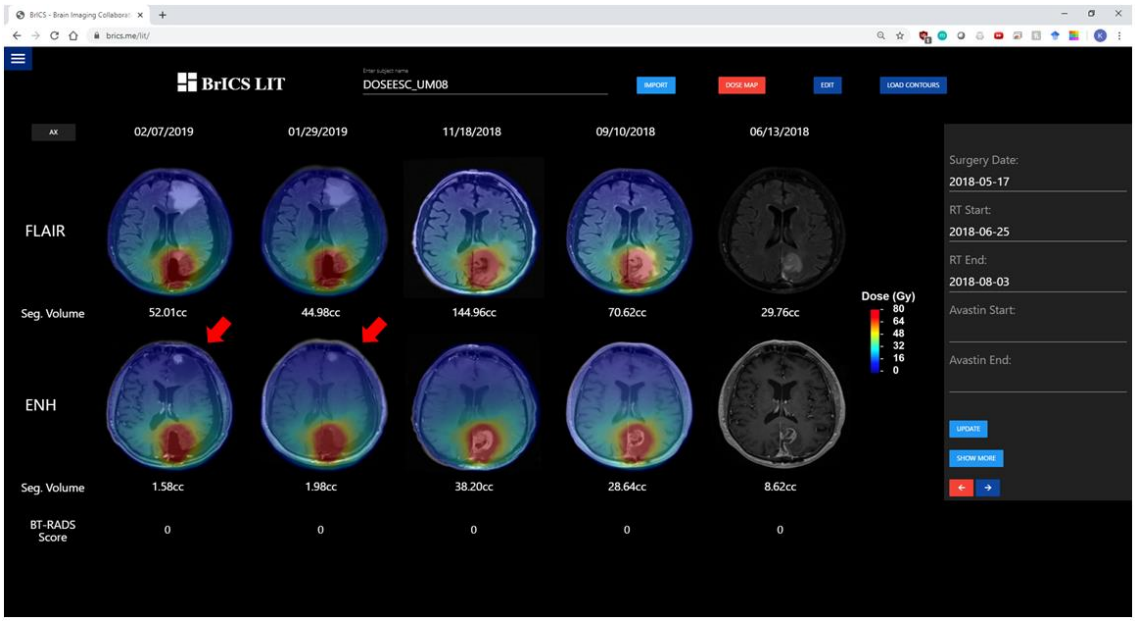

Figure 4.6. A GBM patient from our dose escalation trial at University of Miami who initially received a radiation dose of 75 Gy in the left occipital lobe. However, by 1/29/2019, a distant contrast enhancing lesion appears in the left frontal lobe, away from the radiation treatment zone (indicated by red arrow).

4.4 DISCUSSION

Structured reporting has been widely adopted in clinical workflows for several different cancers including breast and prostate. By standardizing imaging findings and using precise criteria, clinicians can confidently establish patient disease-state and manage patient treatment efficiently. While structured reporting for brain tumors is starting to make

an impact in research settings, it has yet to be adopted in clinical settings. BT-RADS is a framework developed by clinicians at Emory University and has started to spread to other institutions such as Duke University and Johns Hopkins University. The BrICS-LIT web application is designed to provide objective metrics as well as visualization tools to assist clinicians and researchers in classifying patient follow-ups with BT-RADS scores. Thirty patients from a GBM dose escalation clinical trial are currently having their follow-up imaging collected before importing into the BrICS-LIT platform. For those patients, the LIT application will be able to quantify changes in lesion volume in T2 FLAIR and CE-T1w MRIs and help neuroradiologists assign BT-RADS scores with more confidence. By overlaying radiation dose maps, LIT users can more easily identify whether lesions are spreading outside of radiation treatment zones.

While LIT offers several tools to assist clinicians in assigning BT-RADS scores, future plans involve automating several of the features to minimize clinician and researcher effort and decrease outcome variability. By developing a fully automated segmentation algorithm leveraging convolutional neural networks and other deep learning techniques, lesions can be segmented more accurately with minimal user intervention afterwards. Further, the BT-RADS framework is designed to follow a systematic, quantitative flowchart in assigning disease-state classifications. With automated lesion volumes and relevant clinical data acquired through REDCap, suggested BT-RADS scores can be assigned programmatically without intervention. Physicians in clinical settings, including neuro-oncologists seeing patients in clinic and radiologists generating clinical radiology reports, can review the suggested BT-RADS scores and modify them when necessary to obtain the most clinically accurate criteria for monitoring patients during their follow-up

period. Similarly, suggested scores for other metrics such as RANO can be implemented for comparison with research trials. While progression free survival and overall survival are classic metrics used to assess the efficacy of novel therapies in research settings, more sensitive metrics like BT-RADS scores can help discern whether there was improvement between two cohorts during specific time periods of patient follow-up and whether those differences in scores are significant.

Chapter 5. A Novel Approach to Determining Tumor Progression Using a Three-Site Pilot Clinical Trial of Spectroscopic MRI-Guided Radiation Dose Escalation in Glioblastoma

5.1 INTRODUCTION

Glioblastoma (GBM) is a highly aggressive cancer that originates in glial cells in the brain, with a very poor prognosis for every age group. The disease has a median survival of 15–16 months [4,6], a median progression-free survival (PFS) of 4–8 months [6,91], and an annual incidence of 3.19 per 100,000 in the United States [37]. Very few interventions in recent decades have significantly improved outcomes for these patients. Standard therapies for GBM involve the surgical resection of visible tumor followed by radiation therapy (RT) with concurrent and adjuvant temozolomide (TMZ) chemotherapy. Medical imaging plays a central role in this treatment pipeline with clinical MRIs guiding the surgical team and RT planning as well as the follow-up phase after initial treatment where patients are monitored for symptoms and imaging is assessed for concerning abnormalities.

Standard-of-care therapy for GBM patients is guided by a combination of T1-weighted contrast-enhanced MRI (T1w-CE) and T2-weighted fluid-attenuated inversion recovery MRI (FLAIR). T1w-CE indicates areas of high-grade tumor where gadolinium-based contrast agents can accumulate due to breakdown of the blood–brain barrier and is used to guide surgical resection. However, T1w-CE MRI usually underestimates the extent of tumor infiltration [14]. FLAIR identifies areas of surrounding tumor infiltration but cannot differentiate tumor from edema, inflammation, and radiation effects. In standard

clinical practice, T1w-CE lesions combined with the resection cavity are targeted with a higher radiation dose (usually 60 Gy) and surrounding FLAIR hyperintensities are targeted with a lower radiation dose (45–54 Gy), both delivered over 30 fractions [41]. However, these techniques may not adequately target tumor, and imaging methods that detect tumor with high specificity while preserving normal brain may improve outcomes for GBM patients. We have been developing a high-resolution, 3D magnetic resonance spectroscopic imaging (MRSI) sequence with whole brain coverage that we have termed spectroscopic MRI (sMRI) [21]. sMRI is a non-invasive metabolic imaging technique that can non-invasively detect tumor without contrast agents by detecting areas of metabolically abnormal tumor which have elevation of choline (Cho) due to high cell turnover and decreased N-acetylaspartate (NAA) due to displacement of normal neurons and axons by tumor [18,92,93]. In addition, some studies have found a relationship between Cho levels and grade of astrocytoma, with a higher grade being associated with higher Cho [94]. The ratio of metabolite signals Cho to NAA (Cho/NAA) is highly associated with the presence of tumor even in regions of the brain that appear healthy on standard MRI sequences [18,20,43], and a Cho/NAA ratio greater than two times that in normal-appearing white matter (NAWM) are correlated with regions of tumor recurrence in 81% of patients [12]. This information can be used in brain tumor patients to treat invasive tumor with higher radiation doses while minimizing doses to normal brain, potentially delaying recurrence for GBM patients without excessive risk of toxicity.

We recently completed a multi-institutional, single-arm pilot clinical trial for newly-diagnosed GBM patients where brain regions with a Cho/NAA $\geq$ 2x normal were treated with an escalated radiation dose of 75 Gy [21]. Patients had a median overall survival (OS)

of 23.0 months, seven months longer than that in historical controls [5,6,38,40]. During the post-treatment follow-up period, serial MRIs including T1w-CE and FLAIR were acquired at routine intervals, but the interpretation of post-treatment imaging was confounded by the overlapping appearance of tumor recurrence and post-treatment effects including pseudo-progression and radiation necrosis. Both pseudo-progression and radiation necrosis are phenomena characterized by worsening of T1w-CE enhancement and FLAIR hyperintensity after RT due to tissue injury from radiation, with pseudo-progression occurring within 90 days of radiation and radiation necrosis peaking 1 to 2 years post-RT [56,95]. We saw these effects exacerbated in our pilot clinical trial where larger volumes of tissue were treated with escalated radiation dosage. While sMRI could be helpful with tumor detection after treatment, extensive necrosis can lead to a low Cho peak, with signals from lipid and other metabolites such as lactate often suppressing the Cho signal [93,96]. Further, sMRI acquisitions were not available during follow-up for these patients.

To address these challenges, we developed novel quantitative and visualization tools to track patients after initial treatment, minimize the effects of confounding treatment changes, pinpoint tumor recurrence timepoints, and perform PFS analysis. These tools use a combination of a quantitative imaging platform and structured reporting methods. The Brain Imaging Collaboration Suite Longitudinal Imaging Tracker (BrICS-LIT) is a custom-built web application for the purpose of longitudinal MRI imaging follow-up of brain tumor patients [32,52]. Within BrICS-LIT, lesions on FLAIR and T1w-CE imaging are segmented and displayed, radiation dose maps can be overlaid upon anatomic imaging, and patient clinical information can be displayed. Structured reporting can be used for a more objective interpretation of the patient's disease status and has gained popularity for

applications such as breast and prostate imaging [25,26], but remains underutilized in brain tumor imaging. RANO, or the Response Assessment in Neuro-Oncology criteria, has found success in clinical trial applications but is less commonly used in general clinical practice. While we previously reported the (PFS) from our clinical trial, we did not provide details as to how we determined tumor progression, especially when considering the high rates of pseudo-progression and radiation necrosis [21]. In this study, we demonstrate how we determined progression for these patients by applying the Brain Tumor Reporting and Data System (BT-RADS) framework of structured imaging classification to imaging obtained as part of our clinical trial [30,53,78]. BT-RADS scores and lesion volumes were calculated for the quantitative assessment of patient disease-status, and along with the visualization features, served to determine true tumor recurrence timepoints.

5.2 METHODS

5.2.1 Clinical Trial Treatment Protocol

After newly diagnosed GBM patients completed surgery, sMRI scans were acquired along with standard imaging to guide radiation treatment. At each participating site, a Siemens 3T scanner was used to perform an echo planar sMRI pulse sequence with GRAPPA parallelization with either a 32- or 20-channel head coil. The scan was acquired with an echo time of 50 ms, repetition time of 1551 ms, and flip angle of 71 degrees, leading to a scan time of 15 min and a nominal voxel size of 108 μL [12,52]. Raw sMRI DICOM data were processed by the MIDAS software suite (University of Miami, Miami, FL) [51], before being imported into the Brain Imaging Collaboration Suite (BrICS) for visualization and RT planning. Within BrICS, metabolite maps generated by MIDAS were registered

and interpolated to the higher resolution T1w MRI space before being overlaid as heat maps. Contours containing Cho/NAA ≥ 2x normal were generated within BrICS for use as the high-dose radiation target and inspected by radiation oncologists at each respective site to ensure that these contours were appropriate and did not include organs-at-risk such as the brain stem to a significant extent.

In **Figure 5.1**, we show three example patients on the trial. For each patient, the contour which includes Cho/NAA ≥ 2x normal is significantly larger than the extent of contrast enhancement. In standard therapies, only the volume of contrast enhancement (indicated on the right for each patient) would have received high-dose radiation, potentially ignoring significant amounts of infiltrative tumor demarcated by the Cho/NAA metabolite maps. In our trial, the volumes on the left, represented by the 2x contours, received an escalated radiation dose of 75 Gy to potentially delay in-field tumor recurrence. Two additional radiation targets were generated for each patient on the trial—the resection cavity and any residual contrast within the cavity were prescribed 60 Gy and regions of FLAIR hyperintensity were prescribed 50.1 Gy of radiation. The latter two RT targets had a 5 mm margin expansion to account for microscopic invasion of tumor, and all three targets had an additional 3 mm margin added to generate planning target volumes. Radiation was split into 30 fractions and administered over a six-week period. Concurrent TMZ chemotherapy was also administered at standard-of-care dosing (75 mg/m2/day every day) during RT. After completion of RT, adjuvant TMZ was administered for each patient (150–200 mg/m2/day days 1–5 every 28 days) per standard-of-care [10].

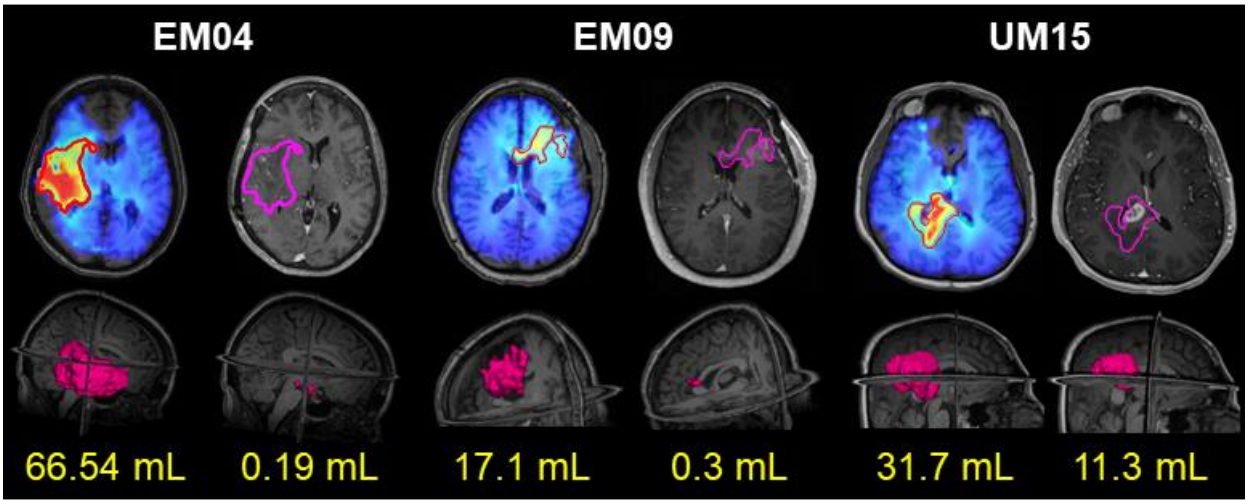

Figure 5.1. A comparison between the ratio map of choline to N-acetylaspartate (Cho/NAA) and T1-weighted contrast-enhanced (T1w-CE) imaging for three patients on the trial. For each patient, the top left image contains the Cho/NAA ratio map superimposed on the T1w image along with a contour encompassing all voxels with a Cho/NAA ≥ 2x normal. That contour is overlaid on the T1w-CE image on the top right image which shows enhancement from residual tumor and recent surgery. The bottom left image shows a 3D volume rendering of the volume of tissue that received 75 Gy of radiation guided by the Cho/NAA ≥ 2x contour, while the bottom right image shows a 3D volume rendering of the residual contrast enhancing lesion, which normally receives 60 Gy of radiation along with resection cavity in standard therapies. In all cases, the Cho/NAA ≥ 2x contour was significantly larger than the contrast-enhancing lesion.

For the cohort of 30 patients who received treatment, 2 had an IDH mutation, 9 were MGMT hypermethylated, 11 had a gross total resection (defined by whether their pre-RT T1w-CE lesion volumes were less than 1 mL), and 19 had a subtotal surgical resection [21]. Informed consent was acquired for every patient in this trial prior to their first sMRI scan, with acknowledgment that follow-up imaging would be collected to monitor treatment response. Both the study and informed consent were approved by the Institutional Review Boards (IRBs) at each participating institution. The following analyses were performed with de-identified datasets from the trial.

5.2.2 Follow-Up

After patients completed RT, they returned for follow-up imaging every 2–3 months. At University of Miami and Emory University, follow-up occurred every 2 months, while patients at Johns Hopkins University had follow-up visits at 3-month intervals. Standard clinical follow-up was performed using the institution standard brain tumor protocol. T2 FLAIR and T1w-CE MRIs from each follow-up visit were uploaded to BrICS-LIT [32]. In BrICS-LIT, each MRI uploaded is rigid registered and interpolated to a higher-resolution, thin-sliced atlas MRI to enable slice-by-slice comparisons across extended time. Enhanced lesions on T1w-CE MRIs and hyperintensity on FLAIR MRIs were contoured in a semi-automated manner with manual editing and inspection by clinicians afterwards [32]. Clinical information about the patient such as the medication they were prescribed, their genetics, and treatment-related information were stored in a REDCap database. BrICS-LIT is configured to automatically retrieve relevant, de-identified clinical information from REDCap. With these segmented lesion volumes, as well as relevant clinical information about the patient, our neuro-radiologist prospectively assigned BT-RADS scores for each follow-up date. In cases with indeterminate imaging findings, additional clinical imaging sequences, such as diffusion-weighted imaging (DWI), and dynamic susceptibility perfusion-weighted imaging (PWI) were reviewed.

In **Figure 5.2**, we show the follow-up imaging of a patient on the trial in BrICS-LIT. Users can simultaneously view 5 study dates at a time and scroll through previous follow-up dates that are available, enabling a comprehensive view of disease state over time. Within BrICS-LIT, segmented contours are highlighted in red, with lesion volumes and BT-RADS scores for each date displayed below. As an example, the earliest follow-up date on the right received a baseline BT-RADS score of 0 as it was immediately post-

surgery and pre-RT. The four follow-up dates to the left occurred 1–11 months post-RT. The next follow-up date to the left received a score of 3A due to increased lesion volumes suggesting a possible cause for concern, however, as the imaging was performed less than 3 months post-RT it more likely reflected pseudo-progression rather than true tumor progression. The imaging in the subsequent two dates received scores of 1A and 2, indicating improvement and stable control of disease, as the lesion volumes remained relatively stable compared to previous follow-ups. The far-left study date, occurring 11 months after completion of RT, received a score of 4 due to a large increase in FLAIR and T1w-CE lesion volumes. In the bottom row of the figure, a radiation dose map is overlaid on T1w-CE imaging, which can help determine whether a patient has experienced out-of-field recurrence, common signs of true tumor progression. This patient's enhancing lesion in T1w-CE started in-field and spread slightly outside of the high-dose boundary margins delineated in red, suggesting possible marginal failure.

Often, if an enhancing lesion grows suspiciously fast, patients will undergo additional surgeries during this follow-up period. Many patients on this trial had second or even third surgeries to remove an enhancing lesion that was suspicious for tumor. After those surgeries, clinical pathologists at each respective site assessed tissue samples for presence of tumor and reported findings in pathology reports.

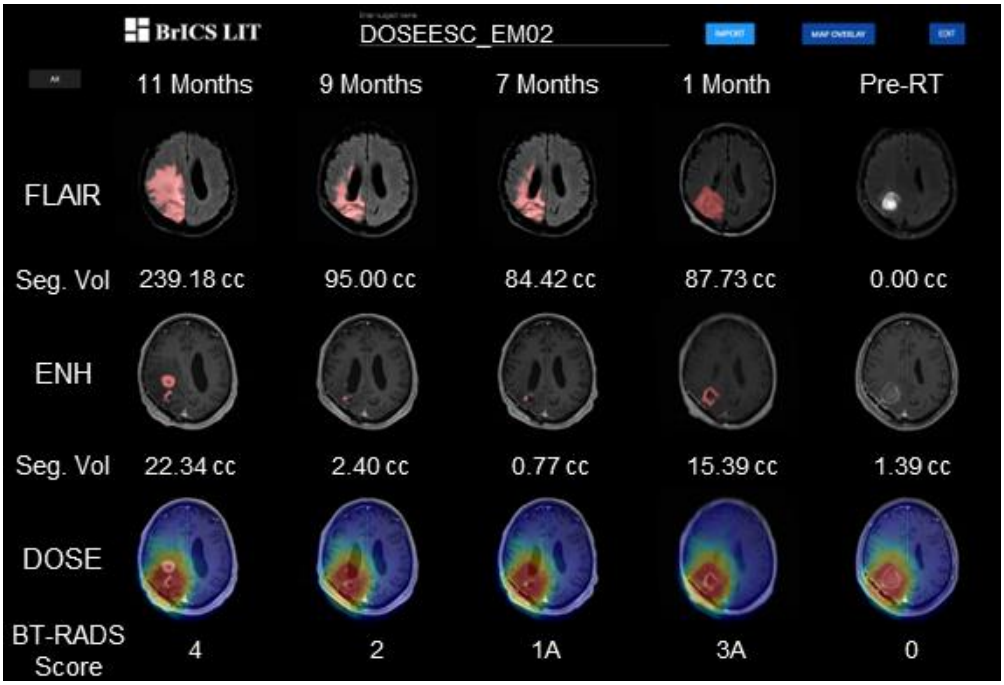

Figure 5.2. A view of the Brain Imaging Collaboration Suite Longitudinal Imaging Tracker (BrICS-LIT). The top row consists of T2-weighted fluid-attenuated inversion recovery (FLAIR) MRIs and the middle row of T1w-CE MRIs co-registered and interpolated to an atlas for easier comparison. Studies are longitudinally arranged from newest (left column) to oldest (right column). Segmented lesions are overlaid in the top two rows, while the radiation dose map is overlaid on the T1w-CE MRI in the bottom row to intuitively determine the radiation dose received of the suspected recurring tumor.

5.2.3 Tumor Recurrence Determination

With BrICS-LIT, we graphed lesion volumes and BT-RADS scores over each patient's follow-up period to observe long-term trends. As tumor-mimicking treatment effects such as pseudo-progression and radiation necrosis are commonly associated with high-dose radiation, we sought to use BrICS-LIT and clinical pathology reports to determine true tumor recurrence dates on a case-by-case basis. The following criteria were established across all patients to label the date of first disease progression. First, if the patient received any follow-up surgery and biopsy, then their pathology report served as the ground truth for tumor progression. If the re-resection or biopsy specimens contained

over 20% tumor as described in the pathology report, the previous date was labeled as progression. When the pathology report did not include a percentage but mentioned positive tumor presence, the previous follow-up was labeled as progression. While other factors included in pathology reports such as mitosis or elevated proliferation index could have been used as cutoff points for progression, these factors were not present in every report we received. Therefore, we used a defined cutoff based on information that every report shared. This cutoff was set a priori and not changed in the analysis. For patients who did not receive re-resection, follow-up imaging was evaluated by comparing volumetric changes of contrast-enhancing and FLAIR lesions over time. Dates where significant increases in segmented tumor volume leading to BT-RADS scores of 3c and 4 were further examined using RT dose map overlays. By overlaying an RT dose map over follow-up anatomic imaging, we could look for cases where an enhanced lesion continued to expand and significantly spread outside of the high-dose target (appearing red in the overlaid dose maps). If the enhancing lesion spread outside the high-dose radiation field, the corresponding follow-up date was defined as the tumor recurrence date. Otherwise, if the enhancing lesion volume stabilized within the high-dose region of the brain, the enhancement was attributed to radiation necrosis. Every case where the enhancing lesion extended past the high-dose radiation target was verified and agreed upon by a neuro-radiologist and the patient's treating radiation oncologist.

5.2.4 Survival Analysis

All survival outcomes were assessed using the lifelines Python survival analysis library [55]. PFS curves were calculated starting from the date of surgery using the Kaplan–Meier estimator method [54]. The PFS was defined from the date of surgery to first disease

recurrence. If a patient died from known causes or surgeries before confirmed tumor recurrence on imaging, their date of death was used as the progression date. For these cases, often the last follow-up imaging acquired was very close to their date of survival. For patients who had not yet progressed or who were lost to follow-up, their last date of contact without tumor recurrence was right-censored.

5.3 RESULTS

5.3.1 Survival Analysis

Eighteen months after completing enrollment, the median PFS time was 16.6 months (**Figure 5.3**) with a median time to follow-up of 20.3 months in censored patients. The Kaplan–Meier estimator with 95% confidence intervals is included. Out of the 30 patients enrolled and who completed treatment, 19 patients had confirmed disease progression at the time of last follow-up. Of the 19 patients either with disease progression or who expired before evidence of progression, 7 had tumor recur within the high-dose radiation field, 3 patients had out-of-field recurrence, 4 patients had new lesions discovered in areas that received minimal to zero radiation, and 5 patients died prior to imaging progression. Out of the 11 censored patients, 5 are still alive without signs of disease progression in follow-up imaging, and 6 are dead without sufficient follow-up imaging to determine when or if tumor recurred before their deaths. These patients were often lost to follow-up with their death date independently confirmed via obituary. For these patients that did die, their last date of contact without tumor recurrence was used and right-censored because of lack of information about the cause of death.

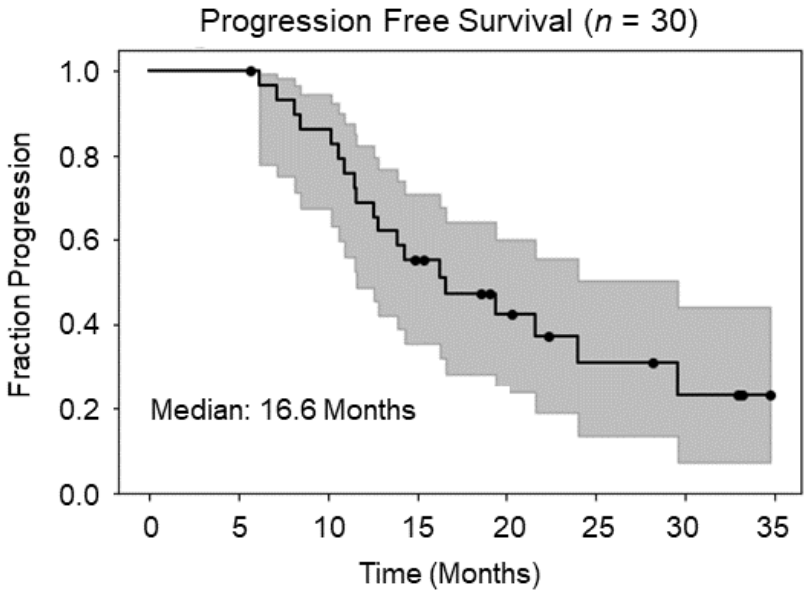

Figure 5.3. Kaplan–Meier estimator for PFS; median PFS: 16.6 months with a median time to follow-up of 20.3 months.

As mentioned previously, fourteen out of nineteen patients with tumor progression had confirmed progression before their deaths. The criteria we outlined for determining progression were applied to this subgroup with additional details in **Table 5.1**. For this patient subgroup, one had an IDH mutation, while five were MGMT hypermethylated status. Due to a small sample size, it is difficult to discern any relationship between, for example, MGMT status and progression type or PFS. However, three of the five patients with MGMT hypermethylation had a PFS that falls below the median for the cohort; however, this could also be due to the post-op residual enhancing volume, which we label as the extent of resection (EOR), and other factors. Of note, patients with multifocal lesions, which received minimal to zero radiation or surgical intervention, led to poorer outcomes and lower PFS values.

Table 5.1. Compiled genetic and PFS data for 14 of the 19 patients with confirmed tumor progression.

Patient	PFS (Months)	IDH	MGMT	EOR (cc)	Progression Type
1	19.0	1	1	1.6	In-Field
2	14.3	0	0	2.6	In-Field
3	16.6	0	0	0.3	Out-of-Field
4	12.6	0	1	2.2	In-Field
5	13.9	0	0	0.5	In-Field
6	8.4	0	0	1.4	In-Field
7	8.1	0	0	12.1	Multifocal
8	6.2	0	0	3.9	Multifocal
9	10.2	0	1	7	Out-of-Field
10	7.1	0	0	0.4	Multifocal
11	11.0	0	1	5	Multifocal
12	11.5	0	0	2	In-Field
13	16.2	0	0	0.5	In-Field
14	29.6	0	1	2.9	Out-of-Field

5.3.2 Example Assessments of Recurrence Using Patient Follow-Up

Due to the difficulty of distinguishing tumor progression from necrosis in a systematic manner when follow-up surgical pathology was not available, we assessed patient follow-up data on a case-by-case basis. Representative examples of imaging evaluation are included below.

The first case is an IDH wild-type, MGMT hypermethylated patient who exhibited progression-like imaging characteristics that were ultimately attributed to treatment effects. **Figure 5.4b** graphs this patient's BT-RADS scores from their initial surgery before RT until their latest follow-up visit. This patient had two surgical resections after RT marked with red stars. After the first surgery, the neuropathologist found minimal tumor even after a one-year gap from completion of RT. About nine months later, the patient received a second surgical resection due to increased enhancement volume on clinical imaging; 80% of sampled cells were necrotic. Leading up to each follow-up surgery, FLAIR and T1w-CE lesion volumes trended upward leading to BT-RADS scores generally above 2, suggesting the possible presence of tumor. **Figure 5.4c** shows follow-up imaging that corresponds to each visit in the graph above. While FLAIR lesion volumes appear to increase after month 12 as indicated by **Figure 5.4a**, the tumor does not appear to spread contralaterally or compress against tissue in the midline of the brain as is visible in the top row of **Figure 5.4c**. The middle row of **Figure 5.4c** shows enhancing volumes from T1w-CE MRIs. The rim of enhancement around the surgical resection cavity appears to spread radially. Despite this, the enhanced rim stays within the high-dose radiation field demarcated in red in the third row. Despite trends in increasing enhancing lesion in **Figure 5.4a**, the volume stabilizes after month 20. During standard clinical follow-up, the increasing enhanced rim and FLAIR hyperintense volumes would lead to an early designation of tumor recurrence. However, both pathology reports in this case failed to identify significant amounts of tumor, suggesting that most enhancement and FLAIR lesions were due to inflammation and necrosis from high-dose radiation for years after they completed RT. This patient is still alive.

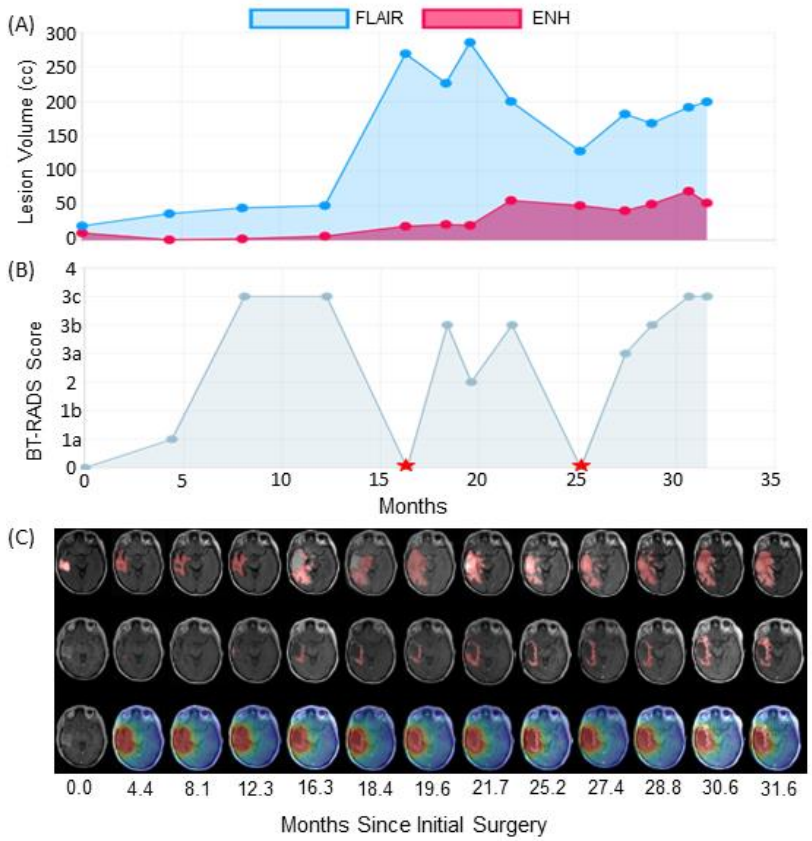

Figure 5.4. With our web platform, clinicians assessed (**A**) graphs of lesion volumes from FLAIR and T1w-CE (labeled ENH) imaging, as well as (**B)** A graph of Brain Tumor Reporting and Data System (BT-RADS) scores during a patient's follow-up. The red stars indicate re-resection of suspected lesions. In this case, the patient had two re-resections (16.3 and 25.2 months) with significant treatment effect and necrosis found in both cases. (**C**) For each follow-up visit in the above graph, the FLAIR MRIs (top row), T1w-CE MRIs (middle row), and radiation dose map overlaid on T1w-CE MRIs (bottom row) are displayed from oldest (left column) to newest (right column). While the increasing enhancing rim as well as FLAIR volumes were cause for concern, this patient had still not had confirmed disease progression.

Figure 5.5 is an example patient with initial in-field tumor recurrence followed by out-of-field progression. In this case, the surgical pathology report indicated 30% tumor in sampled tissue, with the follow-up visit before re-resection (indicated by the red star) labeled as the tumor progression date (indicated by the orange diamond).

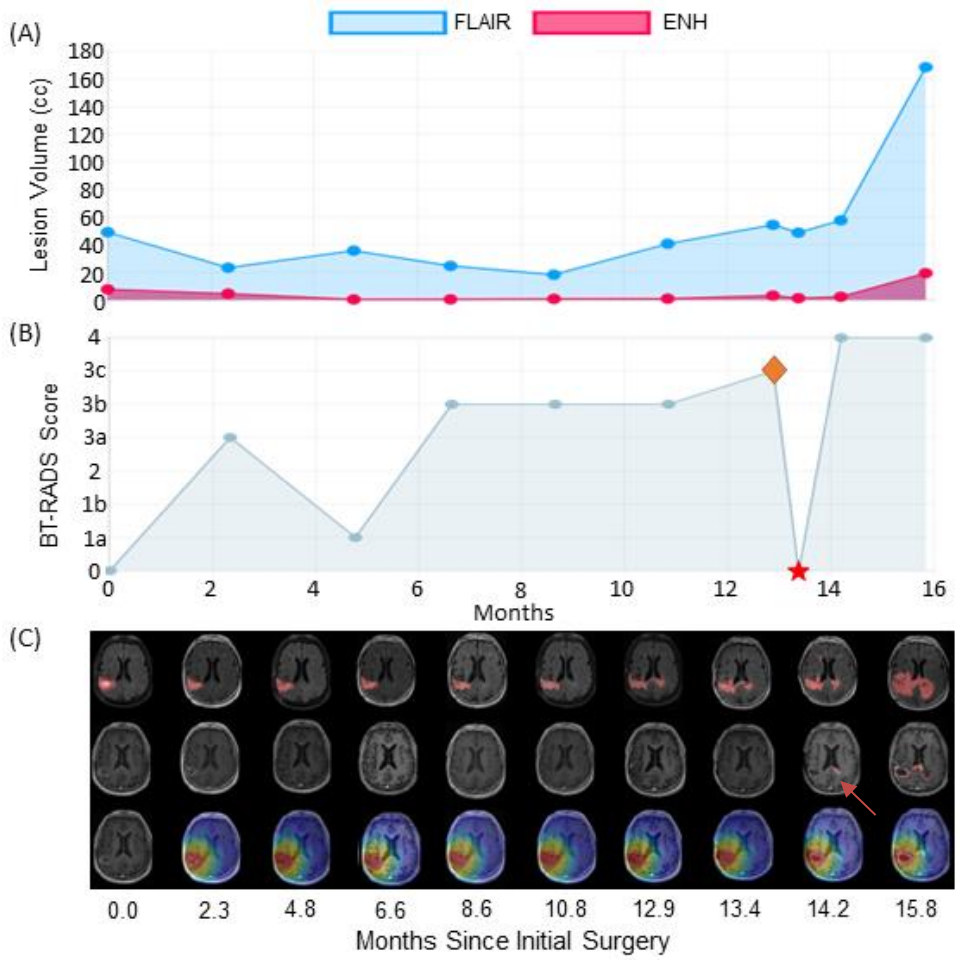

Figure 5.5. (A) A graph of changing lesion volumes from FLAIR and T1w-CE (labeled ENH) imaging can help assess suspicious trends, especially after re-resection in this case. (B) A graph of BT-RADS scores during a patient's follow-up. The red star indicates re-resection of suspected lesions. This patient had one follow-up surgery that found 30% tumor in samples biopsied (13.4 months). Therefore, their recurrence date (orange diamond) was set before their follow-up surgery. (C) For each follow-up visit in the above graph, the FLAIR MRIs (top row), T1w-CE MRIs (middle row), and radiation dose map overlaid on T1w-CE MRIs (bottom row) are displayed. From the 14th month onwards, a second lesion is apparent on the contralateral side of the brain outside of the radiation treatment zone.

This is a case that demonstrates the value of overlaying radiation dose maps. Even after this patient received a follow-up surgery, another enhancing lesion appeared on the contralateral side of the brain. This lesion is outside of the radiation treatment zone. Less than one month after this patient's follow-up surgery, their tumor had infiltrated

contralaterally and was not evident in contrast enhanced imaging before their follow-up surgery. This second focal lesion continues to increase on both FLAIR and T1w-CE imaging shortly after. Both follow-up visits were assigned BT-RADS scores of 4, suggesting true tumor progression. By co-registering follow-up imaging and overlaying radiation dose maps, BrICS-LIT proves useful not only in retrospectively assessing imaging for tumor recurrence but also prospectively identifying out-of-field recurrence in this case. While FLAIR abnormality does spread contralaterally before the second surgery, this could have easily been attributed to treatment-related inflammation, especially due to lack of significant contrast enhancement in the same area.

5.4 DISCUSSION

In this study we describe the use of novel imaging visualization tools and structured reporting to analyze the results to date of our 30-patient clinical trial utilizing dose-escalated radiation guided by Cho/NAA sMRI maps. With standard-of-care therapy including standard RT with concurrent and adjuvant TMZ, GBM prognosis remains poor with a median OS that is consistently limited to about 16 months and an incidence of recurrence at one year from start of treatment of 60–70% [6]. Our results from our single arm study show a substantial improvement with a one-year incidence of recurrence of 30% and median PFS of 16.6 months. For the sake of comparison, Avastin, an anti-angiogenic therapy commonly used for newly-diagnosed GBM patients, minimally improved OS to a timepoint lower than the median PFS calculated in our pilot study (16.1 months) [38]. While these results are promising, we must caution that our pilot study had a much smaller sample size compared to historical controls and the Avastin trial and at the very least, justifies a larger consortium-level trial to determine a true effect size. We have previously reported a

median OS for this cohort of 23.0 months [21,97]. In another trial (NRG Oncology BN001 NCT02179086) that escalated radiation dose guided only by standard imaging [42], there was no significant difference in median OS between standard treatment groups and the dose-escalated group. Guiding radiation targets using sMRI led to larger, more specific treatment volumes that contain high quantities of tumor not visible in standard imaging. By using an imaging technique with a higher degree of specificity, we appear to show a lower one-year incidence of recurrence and improve survival outcomes in this cohort, justifying a larger prospective trial to assess the efficacy of sMRI-guided high-dose radiation.

While escalated radiation shows promising results, a large number of patients on the trial exhibited pseudo-progression and radiation necrosis that lasted far longer than patients on standard radiation therapies. In standard clinical practice, T1w-CE imaging is the mainstay for defining tumor recurrence. However, under high-dose irradiation, post-treatment radiation effects often mimic those of tumor recurrence on clinical images, prompting labeling of disease progression before true tumor recurrence. Multiple patients on the trial were recommended for additional surgeries due to the apparent increase in contrast enhancing volume on T1w-CE imaging; however, these lesions were often in-field of the high-dose target and were later confirmed to be either pseudo-progression or radiation necrosis via pathology reports. The pathology reports for the first patient from our results section showed zero and minimal tumor both one year and two years after completion of RT. It was common to see pathology reports five to even nine months after completion of RT finding minimal tumor in samples biopsied. Our dependence on pathology reports from biopsy for in-field recurrence determination is a limitation for our

criteria, especially in cases where there were not additional surgical interventions at critical timepoints. However, repeat surgical sampling has high morbidity in the clinical setting and is often reserved for the most confusing cases.

While we acknowledge that quantitative tools such as BrICS-LIT do not necessarily solve the problem of differentiating tumor from necrosis, they were helpful in tracking the patient's disease-state during follow-up. Using our LIT database, radiation dose maps, and post-surgery pathology reports, we performed a retrospective analysis showing a ten month improvement of PFS compared to standard therapy using sMRI-guided dose escalation. With BrICS-LIT, we can graph lesion volumes and structured reporting scores throughout the patient's follow-up period. Rather than manually inspecting independent images and qualitatively assessing the patient across their latest few follow-up dates, with BrICS-LIT we can use segmentation algorithms to calculate lesion volumes and make comparisons quantitatively. If, for example, enhancing lesion volume is increasing at an exponential rate, there is good reason to be suspicious for tumor progression. However, if the lesion volume stays within-field and remains stable over several months, the enhancing lesion could be mostly radiation necrosis unless proven otherwise through biopsy. An argument could be made that BrICS-LIT can select for patients who would most benefit from a biopsy. A limitation of this study is that we did not use MRI perfusion-weighted imaging or other advanced imaging to further differentiate imaging findings. While some studies have shown benefits in using MRI perfusion to characterize indeterminate cases, there is wide variation in how it is applied, including at the three trial sites on this study, which would lead to variations in interpretation [98]. A further study is warranted to determine how to incorporate perfusion into follow-up imaging in the clinical trial setting. By using

BrICS-LIT to overlay radiation dose maps, we can visualize whether the lesion has spread outside of the high-dose radiation target and find multi-focal lesions far more easily than the standard clinical tools available.

Future plans involve fully automating lesion segmentation in both FLAIR and T1w-CE MRIs as well as generating suggestive, structured reporting scores for each follow-up visit. While escalating the radiation dosage to 75 Gy led to minimal clinical toxicity for patients on this trial, there was one patient who had grade 3 toxicities as a result of their radiation, with edema on FLAIR imaging pushing across the midline of their brain. Additionally, there were a handful of cases where 75 Gy was not sufficient to control tumor as at least seven cases had in-field recurrence. External factors such as MGMT hypermethylation and IDH mutation likely contribute to how patients respond to different amounts of radiation [24]. Through the imaging data, radiation dosages, sMRI data, genetics, and medication data we have collected in BrICS-LIT as well as REDCap, we are currently working on a time-to-recurrence predictive algorithm that attempts to predict tumor recurrence risk for each voxel in pre-RT imaging. By generating Cho/NAA $\geq$ 2x, 3x, and 4x normal contours and calculating the median recurrence risk within each of these contours, we hope to generate automated radiation-dose plans within each Cho/NAA contour that reduces recurrence risk as much as possible while also minimizing patient toxicity. Finally, with the encouraging survival data from our pilot study, a randomized, phase II clinical trial (EAF211) is planned with the Eastern Cooperative Oncology Group (ECOG)-American College of Radiology Imaging Network (ACRIN) to guide escalated radiation with Cho/NAA sMRI maps.

5.5 CONCLUSION

With a median time to follow-up of 20.3 months for censored patients, guiding escalated radiation dose to glioblastoma patients through spectroscopic MRI led to a median PFS of 16.6 months with a one-year incidence of recurrence from treatment of 30%, half that of standard therapy. These results are extremely encouraging and suggest the need for sMRI to be a part of standard clinical practice. While escalated radiation doses over larger treatment volumes show promising results towards improving survival, differentiating between true tumor recurrence and radiation-related necrosis even one year after completion of radiation therapy remains a challenge.

By developing quantitative web applications such as BrICS-LIT, we have managed to segment lesions and calculate structured reporting scores for each patient during the follow-up phase of their treatment with the hope of more easily delineating recurrence. Through radiation map overlays, graphing lesion volumes for observable trends, and patient pathology reports, we present our methodology for calculating the tumor progression date. Through the quantitative data we have collected in BrICS-LIT, we plan to develop automated, optimized radiation treatment plans that operate at a voxel-level granularity, with the hope of delaying recurrence for as long as possible.

Chapter 6. A Fully Automated Post-Surgical Brain Tumor Segmentation Model for Radiation Treatment Planning and Longitudinal Tracking

6.1 INTRODUCTION

Due to its heavy reliance on imaging, treatment and follow up of brain tumors is an area that could benefit heavily from artificial intelligence (AI) physician guidance. For example, glioblastoma (GBM) is a severe form of brain cancer with a median survival of 15–16 months [5,6,10,40,58]. Standard treatment of GBM first requires resection of as much contrast-enhancing tumor on contrast-enhanced T1-weighted (CE-T1w) MRI as possible. The remaining tumor is treated with adjuvant temozolomide chemotherapy coupled with radiation therapy that targets a high dose of radiation to any residual enhancing tumor in CE-T1w and a lower dose towards hyperintense edema on T2-weighted fluid-attenuated inversion recovery (T2w/FLAIR) MRI. Each of these steps is highly dependent on imaging interpretation, and clinically assistive AI tools could help physicians track and treat GBM patients more accurately and more quickly.

6.1.1 Related Work

While there have been several efforts to segment brain lesions from MRIs, such as through the Brain Tumor Segmentation Challenge (BraTS), those efforts have focused on pre-surgical brain MRIs, and have yet to make a substantial translation into clinically useful tools [99-102]. There have been minimal efforts to develop segmentation algorithms to assist RT planning after surgery. Post-surgical MRIs have altered morphology that includes a

cavity with blood product and heterogenous hyperintensity on FLAIR. In **Figure 6.1**, we show an example patient with CE-T1w and T2w/FLAIR MRIs prior to surgery, shortly after completing RT, and three months after completing RT. The CE-T1w MRIs often only contain trace amounts of residual enhancing tumor post-surgery. The cavity coupled with the small remaining lesion leads to a more difficult task for segmentation models to capture the lesion and the entire cavity. Overlaid on each MRI is the segmentation from the highest-performing Swin-UNETR model trained on the BraTS dataset [103]. We only show these segmentations not to critique the model or approach, but to suggest that previous efforts of brain tumor segmentation solve a different problem and may not be generally applicable to treated tumors.

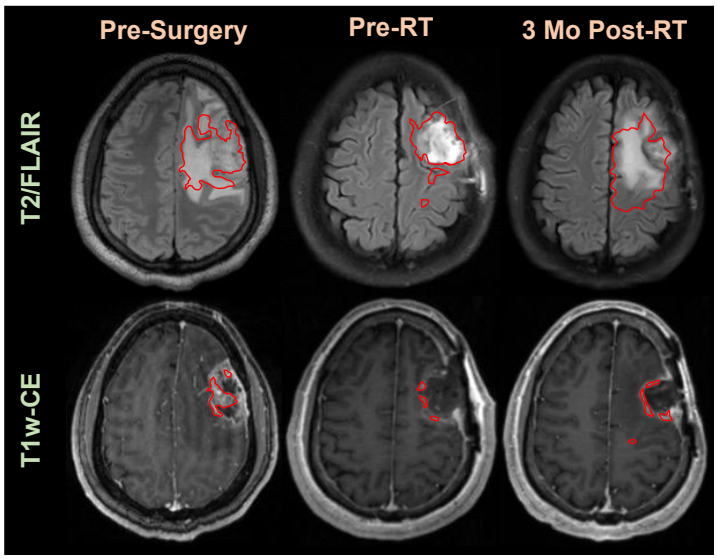

Figure 6.1. FLAIR and CE-T1w segmentation overlays (in red) from a BraTS competition-winning segmentation model over MRIs prior to surgery, prior to receiving radiation therapy, and 3 months after completing radiation therapy.

In standard clinical practice, radiation oncologists generate gross tumor volume (GTV) targets that encompass the residual enhancing lesion and cavity in CE-T1w MRI (GTV2) and edema and cavity on T2w/FLAIR (GTV1). Due to the infiltrative nature of GBM, these targets usually have a margin added to generate clinical target volumes (CTVs) and planning treatment volumes (PTVs). There have been publications that focused on cavity segmentation and performing CTV segmentations with GTVs as input [104-106]. However, this is one of the first efforts to directly train a model for GTV segmentation. Furthermore, previous brain tumor segmentation approaches utilized four sets of images (T1w-pre contrast, CE-T1w, T2w, and T2w/FLAIR) for segmenting lesions in CE-T1w and T2w/FLAIR. In an effort to develop a lighter-weight model, we are attempting to use only CE-T1w and T2w/FLAIR to perform GTV segmentations. Such models that require fewer inputs could be more clinically translatable and require less effort due to lesser data requirements for segmentation by physicians and researchers.

6.1.2 Purpose

Due to the unique visual morphology of post-surgical lesions, and a clinically unmet segmentation approach for these brain MRIs, we sought to develop a lightweight deep learning algorithm that could assist radiation oncologists in generating RT volumes. Finally, with a sophisticated deep learning segmentation algorithm for post-operative brain tumors, we hope to integrate our algorithm within our web application, the Longitudinal Imaging Tracker (BrICS-LIT), to track post-treatment brain tumors and assign automated structured reporting scores [32]. In **Table 6.1**, we summarize the added value of our proposed effort compared to previous approaches of brain lesion segmentation. With BrICS-LIT, physicians can visualize changes in brain lesions over time, as well as assign

structured reporting scores such as the Response Assessment in Neuro-Oncology (RANO) and Brain Tumor Reporting and Data System (BT-RADS) to classify their findings by patient disease-state [30,31,78,107-110].

Table 6.1. A comparison of strengths and weaknesses between previous efforts in brain lesion segmentation and our proposed effort.

Brain Lesion Segmentation	Strengths	Weaknesses
Previous Efforts	• Utilizes pre-contrast T1w and T2w MRIs. • High segmentation performance for pre-surgical lesions. • BraTS includes a larger training dataset from multiple institutions.	• Requires more imaging for each segmentation. • Cannot segment post-operative cavity.
Proposed Effort	• First effort to segment post-operative lesions (including cavity) for RT planning. • Model can also be used for post-RT longitudinal tracking. • Longitudinal lesion volumes can be used to generate automated disease-state classifications. • Ground truth contours generated and reviewed by radiation oncologists and a neuro-radiologist.	• By only using CE-T1w and T2/FLAIR, models utilize less information for prediction, leading to potentially lower segmentation performance. • Training dataset is smaller than BraTS, but larger than other published efforts.

6.2 METHODS

6.2.1 Preparation of Training Data

Imaging from a de-identified database of 225 GBM patients who were treated at Emory University with intensity modulated radiation therapy over the past 10 years was used to train our segmentation model. For each patient, post-operative T2w/FLAIR and CE-T1w MRIs were collected as well as their corresponding GTV1 and GTV2 contours. In **Figure 6.2**, we show an example patient in our training dataset where the extent of

GTV1 includes not only the hyperintense lesion, but also cavity and blood product. In the same figure, GTV2 in CE-T1w MRI includes the cavity and residual enhancing lesion. As per standard-of-care, GTV2 typically receives a higher radiation dose of 60 Gy, while GTV1 receives a lower dose of 50–51 Gy [10,40]. Due to the range of possible margins physicians add to their GTV targets, we had a radiation oncologist resident tighten the treatment contours to only include visible lesions in both sets of images. These tightened contours were then reviewed by an independent radiation oncologist and neuroradiologist with any differences resolved by consensus until agreement was reached.

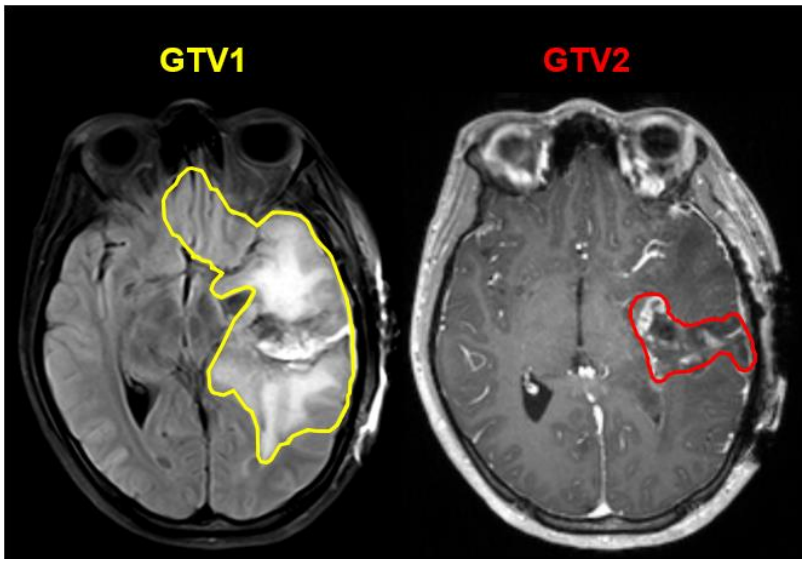

Figure 6.2. Example contour overlays from our training dataset of GTV1 (yellow contour) overlaid on T2w/FLAIR MRI and GTV2 (red contour) on CE-T1w MRI that includes cavity and blood product.

For image preprocessing, T2w/FLAIR MRIs were registered and interpolated to their CE-T1w counterparts. All images were skull-stripped and resampled to a (256,256,160) volume before nonzero voxels underwent zero-mean, unit-variance normalization. For GTV1 segmentation, models were fed a 3-channel input with skull-stripped T2w/FLAIR MRI as the first channel, skull-stripped CE-T1w MRI as the second

channel, and with-skull T2w/FLAIR MRI as the third channel. For GTV2 segmentation, CE-T1w MRI was used for the first and third channels, while skull-stripped T2w/FLAIR was used for the middle channel (**Figure 6.3A**). A third channel with skull was included to help the model delineate the extent of resection cavities that reside close to the skull. For 2D segmentation, slices of size (256,256) were fed in batches for training, while 3D segmentation models trained on volumes of size (128,128,128). The 225-patient dataset was split into a training set of 202 patients and a validation set of 23 patients. For the training data, on-the-fly augmentation was performed with random flipping and rotation with 0.5 probability. An independent test dataset containing T2w/FLAIR and CE-T1w MRIs with corresponding GTVs for 30 post-operative GBM patients from three different sites (Emory University, Johns Hopkins University, and University of Miami) was used to evaluate segmentation performance (**Figure 6.3A**).

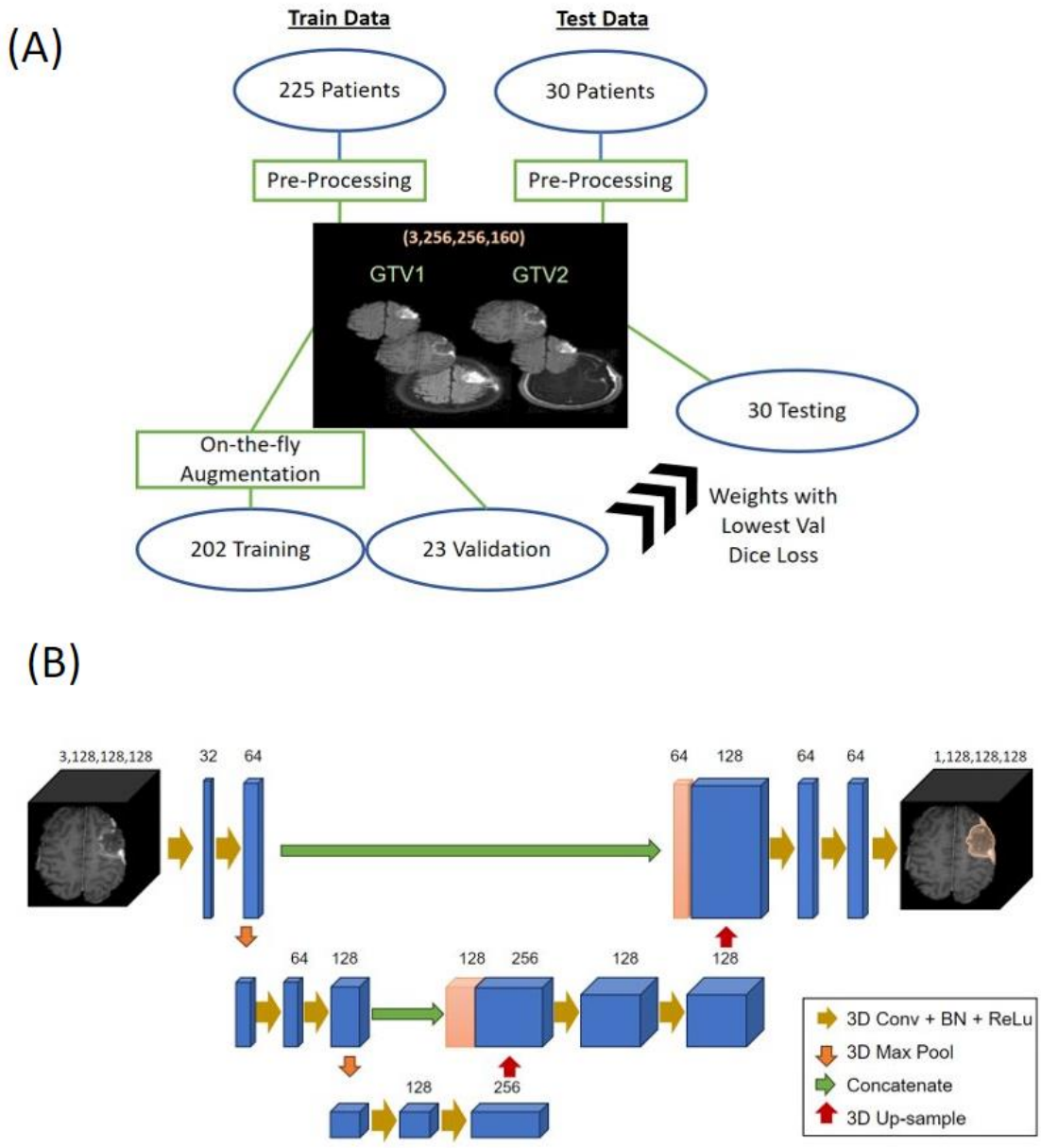

Figure 6.3. (A) Training pipeline for our segmentation models. During the pre-processing step, a 3-channel input was used with the first two channels using skull-stripped T2w/FLAIR and CE-T1w MRIs and the third channel including skull to assist in delineating cavity margins. The model weights that performed the best with the validation data were tested on the independent test dataset. (B) Network architecture for 3D Unet, which has a depth of 3, and was trained on our post-operative MRIs after pre-processing. The number of filters is listed above each block.

6.2.2 Segmentation Models and Training

We compared 2D and 3D segmentation approaches with the goal of incorporating the most robust models in clinical workflows. Three of the most popular 2D segmentation models for medical image segmentation are the standard U-net, ResUnet, and Shifted-Window (Swin)-Unet [111-113]. The ResUnet model has the structure of Unet but with added residual connections in the encoder and decoder blocks to prevent vanishing gradient problems, as well as atrous convolutions and pyramidal pooling to garner more information from larger receptive fields. The 2D Swin-Unet structure is similar to Unet, but replaces standard convolutional neural network (CNN)-based encoder and decoder blocks with Swin transformers, which use tokenized image patches as input and attention-based shifted-window vision transformers to garner global image features [111,114]. Finally, we compared the CNN-based 3D Unet with Swin-UNETR—both 3D segmentation models that have found great success with pre-operative brain tumor segmentation [102,103,115]. The 3D Unet is similar in structure to Unet but uses 3D filters to convolve over image volumes as inputs (**Figure 6.3B**), while Swin-UNETR uses 3D Swin transformers as encoders and standard CNNs for decoding and generating the segmentations.

For the 2D models and 3D Unet, a five-fold cross validation procedure was used to determine the optimal hyperparameters for each model [116]. We used the same hyperparameters as the authors of Swin-UNETR for brain tumor segmentation [103]. The Dice similarity coefficient was used to evaluate segmentation accuracy between model predictions and physician-generated segmentations and Dice loss was used during training [117]. During training, a learning rate scheduler and early stopping criteria were used to reduce learning rate based on validation accuracy to fine-tune optimization, and to stop training when validation accuracy had not improved for 10 epochs. Three-dimensional

models were trained on an NVIDIA RTX 6000 with GPU memory of 48 GB, while 2D models were trained on an NVIDIA V100 with GPU memory of 32 GB. Models were then tested on the independent 30-patient test dataset to calculate test Dice scores, Hausdorff distances, and Jaccard coefficients for comparison and evaluation.

6.2.3 Application of Segmentation in Longitudinal Tracking

We incorporated our best-performing segmentation algorithms into our web application BrICS-LIT for longitudinal tracking and calculated lesion volumes for an example patient. Due to our model including the resection cavity in CE-T1w lesion segmentation, we use Otsu thresholding to cluster GTV2 segmentations into four different groups before removing the lowest intensity cluster to only include the residual enhancing lesion for longitudinal tracking purposes *[86]*. We then used the same volumetric percent change cutoffs used to predict RANO scores from Kickingereder et al. for BT-RADS prediction *[108]*. More specifically, if a T2w/FLAIR lesion changed in volume by 100% or greater or a CE-T1w lesion increased in volume by 40% or greater, then tumor had recurred and BT-RADS score of 4 was assigned. If CE-T1w lesion increased in volume by 20% or greater or T2w/FLAIR lesion volume increased by 50% or greater, then imaging was considered "worsened" and BT-RADS scores of 3 or higher were assigned. Otherwise, imaging was considered improved or stable and scores of 1 or 2 were given. Finally, if for two consecutive visits a patient's imaging had worsened by less than the tumor recurrence cutoff, a score of 3c was assigned to the latest patient visit, suggesting they are highly likely to experience tumor recurrence. By using these cutoffs in a decision-tree-based approach, along with the lesion volumes and relevant clinical and medication information retrieved from REDCap, BrICS-LIT makes automated disease-state classifications.

6.3 RESULTS

6.3.1 Segmentation for RT Planning

In **Table 6.2**, we compare our 2D and 3D fully automated segmentation models. When comparing the purely CNN-based 2D Unet and Resunet models to the 2D Swin-Unet model, we see a similar segmentation performance during training for both GTVs. However, the Resunet outperforms the 2D Swin-Unet model for GTV2 segmentation in the test dataset with a Dice score of 0.57. The 2D Swin-Unet model outperforms the other 2D approaches for GTV1 segmentation with a test Dice score of 0.64, which is comparable to even the 3D approaches.

Table 6.2. A comparison of 2D and 3D approaches to post-surgical GTV segmentation. The CNN-based 3D Unet outperforms the other models on our test dataset with the highest Dice scores (bolded).

Model	GTV1				GTV2			
	Train (Dice)	**Test (Dice)**	**Test (Hausdorff)**	**Test (Jaccard)**	**Train (Dice)**	**Test (Dice)**	**Test (Hausdorff)**	**Test (Jaccard)**
2D Unet	0.93	0.43	78.50	0.19	0.92	0.56	75.41	0.34
2D Resunet	0.93	0.58	58.50	0.36	0.91	0.57	35.57	0.35
2D Swin-Unet	0.89	0.64	60.71	0.44	0.86	0.51	35.63	0.31
3D Unet	0.77	**0.72**	12.77	0.51	0.79	**0.73**	10.75	0.58
3D Swin-UNETR	0.64	0.60	38.32	0.36	0.65	0.64	23.33	0.44

While both 3D Unet and Swin-UNETR have found great success in brain tumor segmentation tasks in the past, the 3D Unet outperformed 3D Swin-UNETR for our task of segmenting radiation treatment contours and, importantly, this was inclusding the surgical resection cavity. Interestingly, with the early stopping criteria we had in place for each training task, the Swin-UNETR model converged at a lower training Dice score of

0.64 for GTV1 and 0.65 for GTV2, whereas the 3D Unet model converged at higher GTV1 and GTV2 training Dice scores of 0.77 and 0.79, respectively. The difference in Dice scores between training and testing was at most 0.06 for the 3D models. The table also includes the Hausdorff distance and Jaccard coefficient for the test dataset. A higher Hausdorff distance indicates a greater disagreement between prediction and ground truth as it calculates the largest distance between a point in the ground truth and its closest point in the prediction, while the Jaccard coefficient generally scales with the Dice score but penalizes poor predictions more, and is therefore consistently lower in the table.

In **Figure 6.4**, we show example GTV segmentations from our best-performing model, the 3D Unet. The first two columns contain CE-T1w MRIs and the second two columns contain T2w/FLAIR MRIs for three patients from three different institutions. We show a 2D contour in axial orientation as well as a 3D volume rendering of the overlap between GTV prediction and clinician-derived contours in sagittal orientation. Our model's GTV predictions are almost identical to those created by clinical experts, and we believe these examples illustrate the unique task that our model was trained to solve. For both GTVs, the resection cavity was included, as it typically receives a higher dose of radiation. During radiation treatment planning, clinicians can use the segmentations from CE-T1w to generate high-dose GTV2 contours and subtract the GTV2 contour from the GTV1 contour to generate a lower dose targeted towards edema and infiltrative disease.

When evaluating the performance of the 3D Unet model further, about 75% of the test patients had a Dice score greater than 0.70 for GTV1 and greater than 0.67 for GTV2. This suggests that outliers in roughly a quarter of the test dataset caused the average performance of the model to decrease. To that end, **Figure 6.5** shows some of the poorer-

performing examples. In **Figure 6.5A**, while the model appears to segment the T2w/FLAIR hyperintensity and blood product quite well, it completely misses the small enhancing lesion in CE-T1w MRI, possibly missing it due to a lack of cavity nearby or its relatively small size. **Figure 6.5B** is an example where GTV2 is segmented in CE-T1w MRI, but the model underestimates the extent of T2w/FLAIR hyperintensity. This is possibly due to the relatively low contrast between abnormal and normal tissue on some of the 3D T2w/FLAIR acquisitions. **Figure 6.5C** is a case where the model confused the ventricle for a cavity as there was hyperintense T2w/FLAIR lesion in the same area.

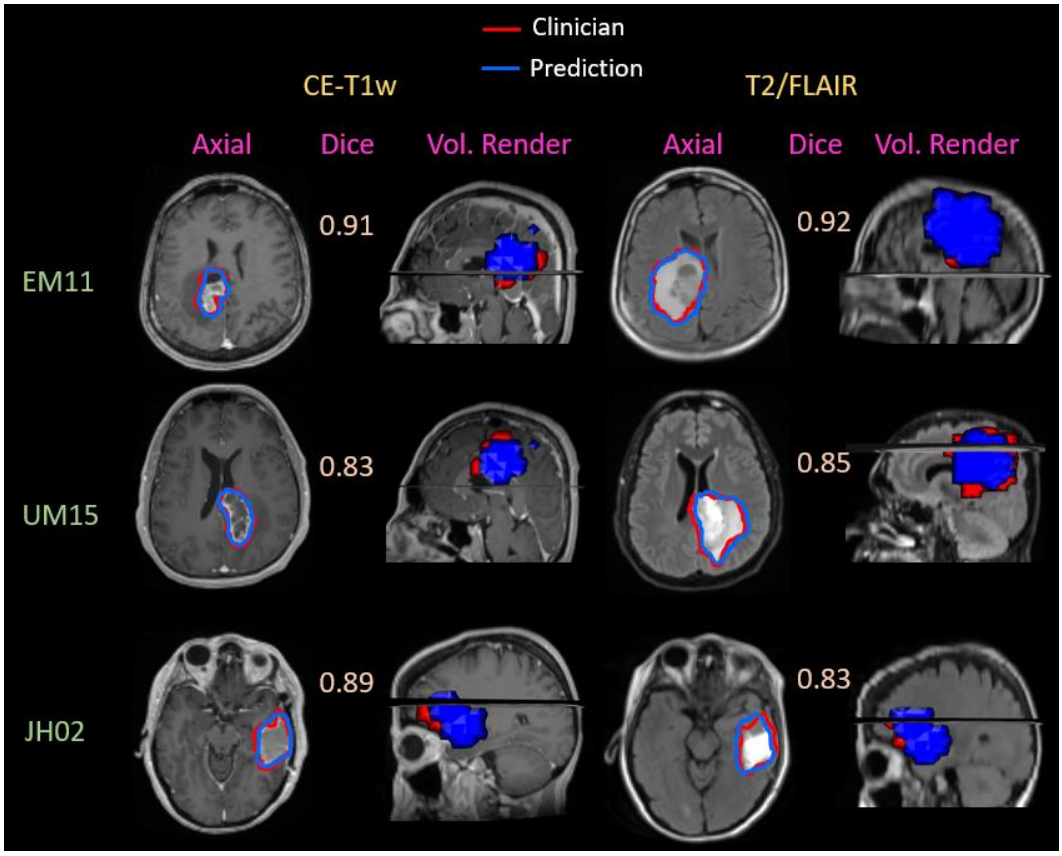

Figure 6.4. Example GTV2 (CE-T1w target) and GTV1 (T2w/FLAIR target) segmentations for patients from three different institutions with our best-performing 3D Unet model. For GTV2 and GTV1, we have included an axial view of the clinician GTVs (red) and the prediction (blue) as well as a volume-rendered view of the contour overlap in

the sagittal orientation. Dice scores are included between the 2D and volume rendering for each example.

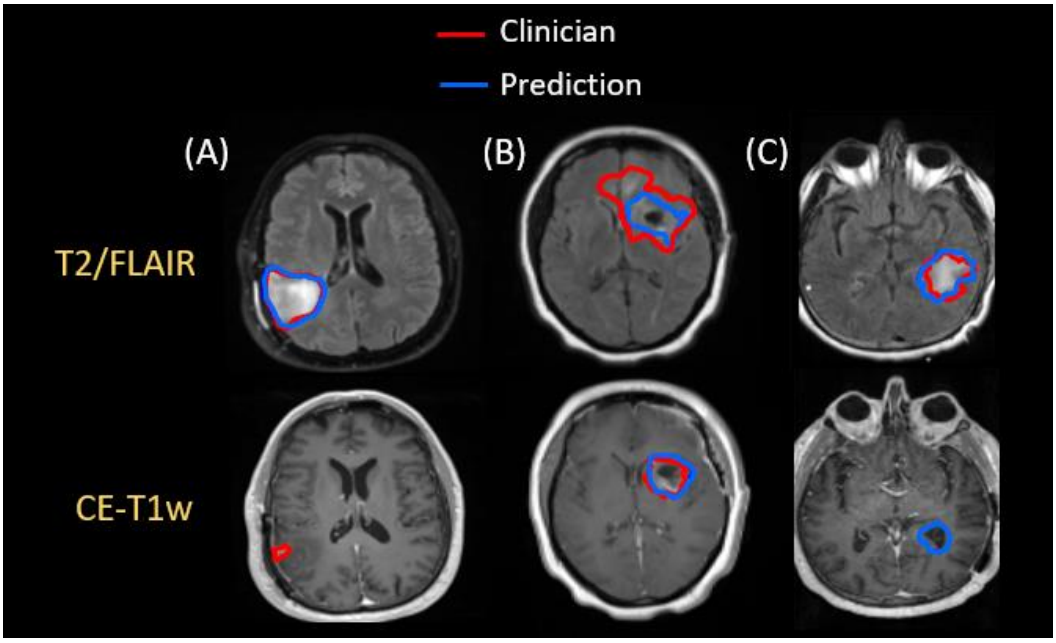

Figure 6.5. The three worst-performing cases of our 3D Unet model. In (**A**), the small CE-T1w lesion is missed, possibly being confused for blood vessel. In (**B**), the model has difficulty capturing the entire extent of hyperintensity from the 3D T2w/FLAIR acquisition, and in (**C**), the model confuses the ventricle for the shape of a cavity, especially when there are T2w/FLAIR edema in the same region.

6.3.2 Application of Segmentation in Longitudinal Tracking

With a fully automated segmentation model trained on post-operative MRIs, we sought to test our model in our web application BrICS-LIT for automated longitudinal tracking. To that end, **Figure 6.6** shows an example patient's pre-operative/pre-RT and post-RT follow-up MRIs. Our 3D Unet model performed segmentations of T2w/FLAIR and CE-T1w lesions, and after Otsu thresholding, the cavity was removed from the CE-T1w segmentations. Then, volumetric cutoffs that were used for RANO classification were applied to this patient's lesion volumes. As per BT-RADS, the baseline score at post-surgery, on the far right, received a score of 0. In the next follow-up visit after the

completion of RT, the CE-T1w lesion grew by almost 25% while the FLAIR lesion grew by slightly over 25%. A score of 3A was automatically given as imaging had worsened, but the visit was shortly after the completion of radiation treatment, and the increased volumes were attributed to radiation-related inflammation. In the following visit, lesion volumes increased by 37% and 27% for T2w/FLAIR and CE-T1w lesions, respectively. Due to the lesion volumes increasing for consecutive dates, a score of 3C was given, suggesting the lesion was highly likely to experience tumor recurrence. In the next visit, the T2w/FLAIR lesion volume had decreased but enhancement was similar or slightly larger. These mixed findings resulted in assigning the indeterminate BT-RADS score of 3B. On the latest visit, the CE-T1w lesion volume increased by 70%, well over the 40% cutoff, immediately causing BrICS-LIT to assign a score of 4, highly probable for tumor recurrence. This also meets the criteria for RANO progressive disease.

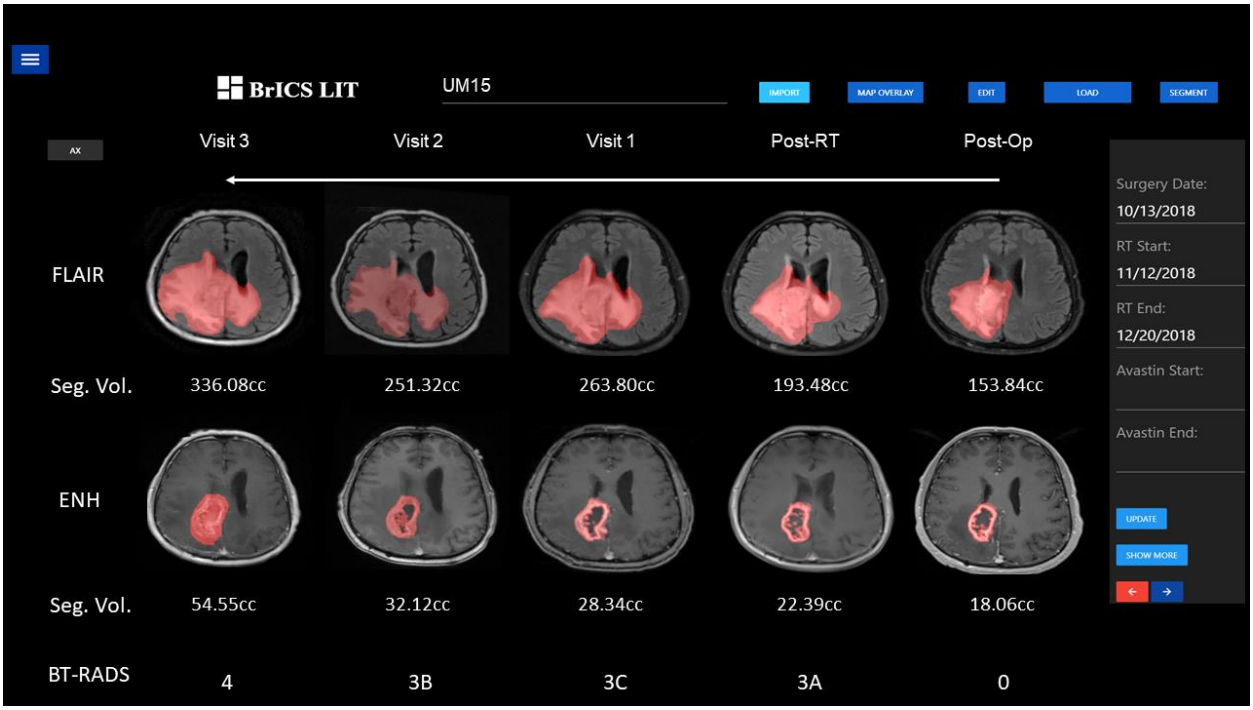

Figure 6.6. The 3D Unet segmentation model implemented into our web application BrICS-LIT, displayed for an example patient's post-operative and post-RT follow-up MRIs. Automated lesion segmentations (red overlay) and lesion volume cutoffs assist in generating automated structured reporting scores (bottom row) for post-treatment longitudinal tracking.

Figure 6.7 shows a graph of changes in T2w/FLAIR and CE-T1w lesion over time, as well as corresponding BT-RADS scores for the same patient generated by BrICS-LIT for physician viewing. The sharp increase in both lesion volumes is apparent 6 months after surgery, signaling true tumor recurrence.

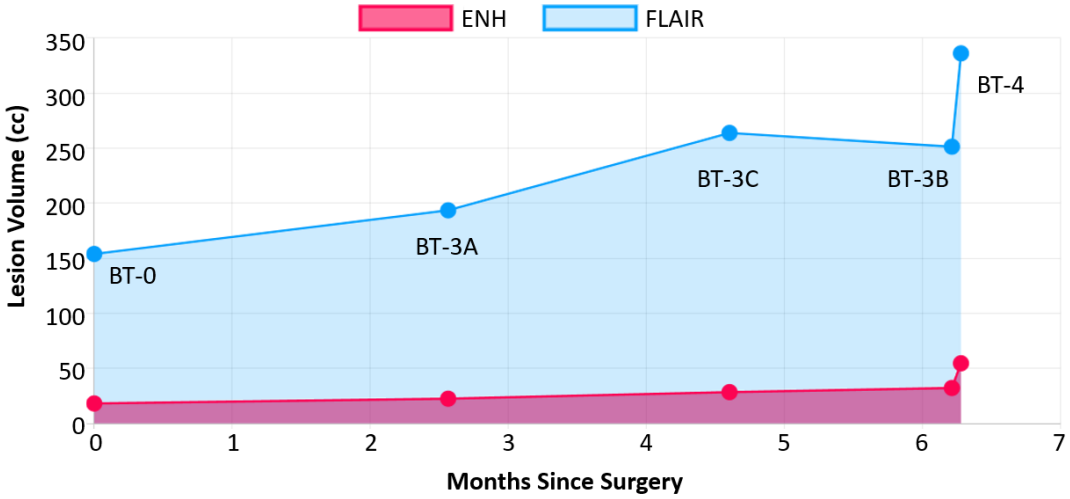

Figure 6.7. Interactive chart tracking changes in CE-T1w lesion volume (ENH), T2w/FLAIR lesion volume, and structured reporting scores for the patient shown in Figure 6.6. A drastic increase in lesion volume is seen 6 months after surgery.

6.4 DISCUSSION

With the advent of artificial intelligence in many domains of our daily lives, a question remains as to when it will be included in standard-of-care medical treatments. While there has been an entrepreneurial boom in integrating deep learning and machine learning to the domain of personalized medicine, there are still many challenges in including AI-based tools in clinical imaging workflows [118-120]. Some of these challenges

include the need for physicians to have efficient image processing software that can easily pre-process clinical imaging, handle computationally heavy algorithms, and perform inference, all while requiring minimal effort by the physician [121]. Furthermore, visualization tools can help physicians understand the reasoning behind predictions and decisions that AI algorithms make [121]. To that end, we trained the first deep learning segmentation algorithm for post-operative brain tumors for the purpose of radiation treatment planning and longitudinal tracking. With reliable GTV1 and GTV2 segmentation models that can perform segmentations in less than a minute, radiation oncologists can expediently generate GTV targets and add margins depending on their preferences to generate larger CTVs and PTVs for radiation treatment. These tools could potentially be integrated into radiation planning software commonly used by radiation oncologists. By using volumetric cutoffs, we can suggest completely automated disease-state classifications for the longitudinal tracking of post-treatment brain tumor patients, which we implemented using the BT-RADS rating scale in our online BrICS-LIT platform.

In comparing our 2D and 3D segmentation approaches, it is evident that the 2D models are overtrained, as the training Dice scores were above 0.90 while the testing Dice scores ranged between 0.43–0.64. We set early stopping criteria which would cause our models to stop training when the validation accuracy failed to improve after 10 epochs. This suggests that the 2D models were still learning some generalizable information, even if the gap between training and validation accuracy was steadily increasing. The benefit of using 3D approaches is that while their training accuracy was lower than the 2D models, the testing accuracy was somewhat aligned with the training accuracy, leading us to believe the 3D approaches are more robust with test images.

Our best-performing segmentation model was the CNN-based 3D Unet, with test Dice scores of 0.72 and 0.73 for GTV1 and GTV2, respectively. In comparison, segmentation models that won the BraTS challenge typically achieve test Dice scores close to 0.90 or higher. The distribution of Dice scores in our test dataset suggests that there were a few cases that severely decreased the mean Dice score, which gives us room for improvement. The models struggled with small residual enhancing lesions in CE-T1w with minimal cavities, which can easily be confused for blood vessels. In such cases, physicians would need to know in advance whether there is sufficient cavity/lesion for the model to segment more accurately. They also struggled with the task of differentiating cavity from ventricle, especially when there was T2w/FLAIR hyperintense lesion in the same area. Finally, the model appears to struggle with capturing the entire extent of the lesion boundary in 3D T2w/FLAIR, where the acquisitions prioritize higher spatial resolution over contrast. Although we implemented several augmentation techniques such as random intensity shifting and random k-space sampling to mimic various levels of spatial resolution, we found that augmentation did not improve our models' ability to generalize to the test data. Future efforts will involve curating a more diverse training dataset that also includes smaller residual enhancing lesions and a higher number of 3D T2w/FLAIR acquisitions. Ensuring that models have good-quality, high-contrast 3D FLAIR acquisitions can also help with segmentation.

Many brain tumor segmentation efforts use four sets of images to help segment lesions—T1w pre-contrast MRI, CE-T1w, T2w MRI, and T2w/FLAIR. The Swin-UNETR model achieved high Dice scores with the pre-operative BraTS dataset by utilizing all four sets of images. The encoder region of the model utilizes Swin transformers, which in theory

would help the model determine affinities between different regions of the image. We believe it may have underperformed with our smaller training dataset with fewer image channels due to its complexity. A model of that complexity may have overfit the dataset, and with our early stopping criteria, converged too quickly even with small learning rates compared to the 3D Unet model. We chose to train our models with only CE-T1w and T2w/FLAIR MRI in order for our models to fit within clinical workflows with minimal effort, since CE-T1w and T2w/FLAIR are the sequences most heavily relied on by radiologists, radiation oncologists, and neurosurgeons to identify tumors. When housing our models in web applications like BrICS-LIT or even attempting to integrate them in clinical software like Velocity (Varian Medical Systems), we wanted our models to have as few requirements as possible to enable easy integration. For example, our goal with BrICS-LIT is the longitudinal tracking of brain tumor patients in clinical and research settings. It is far easier for researchers and clinicians to use our models in BrICS-LIT if the models only require the imaging that the clinicians were currently viewing as inputs. We do acknowledge that extra imaging, and most importantly the T1w pre-contrast MRI, could potentially improve our models' segmentation accuracy. To address this concern, efforts are currently underway to train generative adversarial networks (GANs) on the BraTS 2021 dataset to artificially generate T1w-pre contrast and T2w MRIs from CE-T1w and T2w/FLAIR MRIs [122-124]. With a complete dataset from four imaging modalities, we plan to use previous BraTS competition-winning models that are trained on pre-operative MRIs and perform transfer learning on our dataset to finetune the task of including cavities, blood product, and the entire extent of hyperintense edemas.

As demonstrated in **Figure 6.6**, we have already integrated our model in our web application (BrICS-LIT) that is actively used by clinicians and researchers. By performing automated lesion segmentation and using quantitative volumetric cutoffs, we have shown our post-operative segmentation algorithms can help us generate automated disease-state classifications for BT-RADS and RANO. While borrowing volumetric cutoffs used for RANO classification have led to interesting BT-RADS classifications, we acknowledge that both structured reporting criteria may require different volumetric cutoffs that are more suitable for each. To mitigate this issue, we have a de-identified, independent database of over 150 patients with clinician-assigned BT-RADS scores that we will treat as the gold standard to help determine new volumetric cutoffs specific to BT-RADS. Furthermore, simply using percentage changes in lesion volume has its own limitations. For example, a patient could have a residual enhancing lesion that is only 0.4 cc. In their next visit, that lesion could grow by 50% to 0.6 cc. While our automated algorithm would likely say the tumor has recurred purely based on percent change, that 0.2 cc increase in lesion volume could simply be a rounding error in our segmentation algorithm. To address this point, we are investigating the use of classification and regression tree-based machine-learning approaches to predict disease-state classifications using lesion volumes and other relevant clinical information.

6.5 CONCLUSION

While there have been several successful efforts in the past to segment brain tumor lesions in an automated manner from MRIs, they tend to focus on pre-operative brain MRIs, which may limit their usefulness in clinical use and in clinical trials. Here, we have trained popular medical image segmentation algorithms for post-operative, residual brain

tumors for the purpose of radiation treatment planning and longitudinal tracking. The best-performing 3D Unet can segment lesions with over 70% accuracy for most of our test cases and has already been integrated into our BrICS-LIT web application for clinician and research use.

Chapter 7. Final report on clinical outcomes and tumor recurrence patterns of a human pilot study assessing efficacy of belinostat (PXD-101) combined with chemoradiation in treating newly diagnosed glioblastoma

7.1 INTRODUCTION

Glioblastoma (GBM) is the most common primary brain tumor in adults. It is highly aggressive and associated with poor prognosis (despite multimodal treatment). The current treatment paradigm consists of maximal safe neurosurgical resection followed by radiation therapy (RT) with concurrent and adjuvant temozolomide (TMZ). This regimen consists of focal RT to 60 Gy over 6 weeks with concurrent TMZ given at 75 mg/m^2/day followed by adjuvant TMZ given at 150–200 mg/m^2/day for days 1 to 5 of a 28-day cycle for up to 12 months. Despite comprehensive treatments, median overall survival (OS) remains at 16 months [6,10,40,42,58,125].

Histone deacetylases regulate a wide variety of cellular functions and play a role in re-differentiation of various tumors. Histone deacetylase inhibitors (HDACi) have been shown to improve outcomes for patients with gliomas [126]. In 2006, suberanilohydroxamic acid (SAHA), a first-generation HDACi which targets multiple class I and class II HDAC family members, became the first HDACi to receive FDA approval for advanced cutaneous T-cell lymphomas [127].

Belinostat (PXD-101, Acrotech Biopharma, LLC, East Windsor, NJ), a later generation pan-HDACi, improves upon SAHA with increased potency and BBB

penetration [128,129]. Belinostat received FDA approval for patients with relapsed/refractory peripheral T-cell lymphoma in 2014 [130]. Preclinical investigations have shown antitumor effects in orthotopic glioma animal models [131]. This suggests that development of a potent HDACi capable of penetrating the BBB has the potential to improve outcomes of patients with GBM. In addition to anti-tumor effects, we reported that belinostat restores the bottle neck enzyme levels of normal brain metabolites, N-acetylaspartate (NAA) and myo-inositol, *in vitro* to a greater extent than other HDACis [131]. Furthermore, spectroscopic magnetic resonance imaging (sMRI), a quantitative imaging technique that assesses metabolic responses *in vivo* without any contrast agent injection, has been used to show a GBM patient with an IDH mutation (without MGMT promoter hypermethylation) exhibited remarkable response to belinostat combined with chemoradiation therapy [132]. In that case restoration of NAA, creatine and myo-inositol, reached the levels of healthy subjects.

We previously reported interim PFS and sMRI findings in GBM patients receiving belinostat [131,132]. With 50 months of median follow-up, we report the final clinical outcomes and tumor recurrence patterns of patients enrolled in this study.

7.2 METHODS

7.2.1 Patient Enrollment

Patients with newly diagnosed GBM were enrolled in either the control or treatment arm of the Institutional Review Board (IRB)-approved clinical trial at Emory and Johns Hopkins (ClinicalTrials.gov ID NCT02137759). Patients on the treatment arm received

intravenous belinostat (Acrotech Biopharma, LLC, East Windsor, NJ, USA) as an investigational therapeutic.

7.2.2 Treatment

This was not a randomized study; patients were serially enrolled into the control arm from 2014 to 2015 and then the belinostat treatment arm from 2015 to 2018. All patients, if surgical candidates, underwent maximal safe tumor resection before enrolling in the study. Patients in both arms received standard treatment including daily TMZ (75 mg/m^2) and focal radiation doses of 51 Gy to T2/FLAIR abnormality (GTV1) and 60 Gy to the resection cavity/residual contrast-enhancing (CE) tissue (GTV2) on T1-weighted contrast-enhanced MRI (T1w-CE). Margins of 5 to 10 mm were added to generate clinical tumor volumes (CTVs) and 3 to 5 mm to generate planning treatment volumes (PTVs) to account for microscopic disease spread and treatment setup uncertainty, respectively. PTV1 is the FLAIR abnormal volume receiving 51 Gy while PTV2 is the T1w-CE volume receiving 60 Gy. The choice to use two radiation target volumes is common practice for participating institutions in this trial and recognized by organizations such as RTOG and ASCO [133,134]. Further, a two-target regimen has been conducted in other clinical trials to success [21,41,42,133-135]. Enhancing lesions in T1w-CE imaging are highly specific for tumor as those regions of the brain have experienced a breakdown of the BBB, justifying a higher radiation dose of 60 Gy. While spreading hyperintensities in T2/FLAIR are indicative of infiltrating tumor, they also include edema and inflammation, justifying a lower radiation dose.

In the treatment arm, patients received daily intravenous doses of belinostat for five consecutive days in three cycles, three weeks apart, beginning one week before the start of chemoradiation. The first three patients received 750 mg/m^2 of belinostat. However, due to two of the patients having adverse hematologic toxicity during the course of belinostat, TMZ, and radiation, the belinostat dose was lowered to 500 mg/m^2 for the remaining patients in the trial. Patients were followed with standard MRIs for 12 months post-treatment or until radiographic progression of disease. The study timeline for the belinostat cohort is summarized in **Figure 7.1**. Patients in both the control and belinostat cohorts underwent the same radiation therapy dose plan guided by T1w-CE and T2/FLAIR imaging. PFS is reported for patients based on time to radiologic confirmation of disease progression from the date of surgery. Data are right censored for patients who were lost to follow-up. Kaplan-Meier curves for OS were generated.

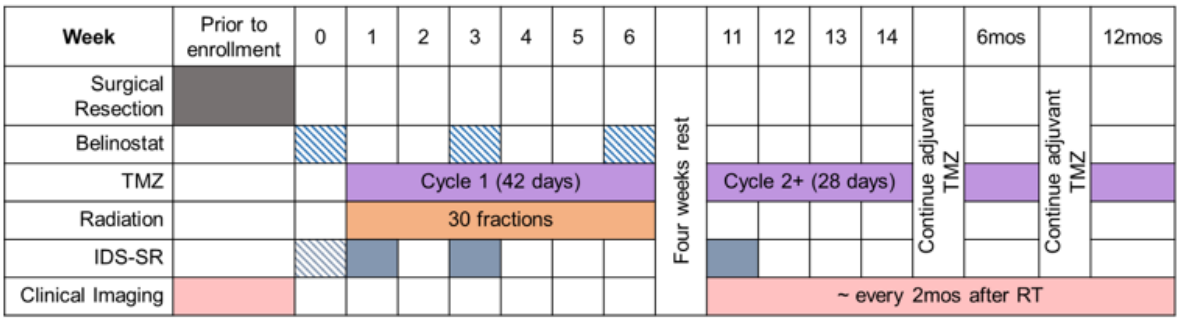

Figure 7.1. One-year timeline of chemotherapy, intravenous belinostat, and radiation for patients in NCT02137759.

sMRI data were acquired for patients before starting treatment and four weeks post-RT. The sMRI data acquisition combined 3D echo-planar spectroscopic imaging, with GRAPPA (Generalized Autocalibrating Partial Parallel Acquisition) parallelization, and elliptical k-space encoding (TE/TR/FA = 17.6ms/1551ms/71°) on 3T MRI scanners with a

32-channel head coil array (Siemens Healthineers or Philips Healthcare) [50]. Raw data were processed using the Metabolite Imaging and Data Analysis System (MIDAS) (University of Miami) [50,51,61] with a nominal voxel size of 4.4 mm × 4.4 mm × 5.6 mm. Metabolite maps generated included choline (Cho), Creatine (Cr), N-acetylaspartate (NAA), as well as Cho/NAA ratio maps [12]. Metabolite and ratio maps were then imported into the Brain Imaging Collaboration Suite (BrICS) for registration with the radiation planning MRI images [52]. A new volume was created based on union of Cho/NAA elevated lesions with residual contrast-enhancing volume (excluding resection cavity) as described in our dose escalation trial scheme [52].

7.2.3 Follow-Up

After completing enrollment in August of 2018, we continued to track patients to assess long-term outcomes and recurrence patterns. Tumor progression was determined using a combination of the BT-RADS (The Brain Tumor Reporting and Data System) structured reporting criteria as well as clinical judgment, which is standard practice at Emory University [30,31,53,109]. For each patient, T1w-CE MRIs were acquired at the radiologically confirmed progression dates and co-registered to MRIs used for RT planning. The recurrence volumes based on enhancement in T1w-CE MRIs (rGTVs) were generated by manually contouring abnormal enhancement in the progressed MRIs. Overlap statistics were calculated between rGTV and PTVs (PTV 1 and 2) as well as calculation of the minimum, maximum, and mean radiation doses that the rGTV volume received using in-house automated algorithms to perform voxel-wise dose comparisons. Radiation doses received by each volume were extracted from the clinical system using the Eclipse Scripting Application Programming Interface (ESAPI) which is built into the Eclipse

treatment-planning platform (Varian Medical Systems, Inc., Palo Alto, CA, USA). Incorporation with this platform enabled automation of our method, saving time and errors that often occur from manual data extraction, with the additional benefit of using the original measurements of the radiation dose clouds for a comparison to tumor recurrence in terms of the range and median doses received by those regions. Two patients were excluded from analysis of rGTV due to follow-up imaging being unavailable.

7.3 RESULTS

7.3.1 Survival Analysis

A total of 26 patients were enrolled (13 control and 13 belinostat) with median follow-up of 50 months. Patient/tumor characteristics were similar between cohorts (Table A1); summary statistics are highlighted in **Table 7.1**.

Table 7.1. Summary statistics for both cohorts including tabulation of significant toxicities (≥grade 3) in all patients. * All occurrences were at 750 mg/m^2/day dosing.

	Control	**Belinostat**
Number of Patients	13	13
Age	58.5 ± 11.1	51.2 ± 11.6
IDH1 Mutation	1 (7.7%)	1 (7.7%)
MGMT Methylated	4 (30.8%)	4 (30.8%)
Toxicities (Grade)		
Thrombocytopenia (4)	0/13	2/13*
Neutropenia (4)	0/13	1/13*
Lymphopenia (3)	3/13	1/13*

Constipation (3)	1/13	1/13
Fatigue (3)	1/13	1/13
Confusion (3)	1/13	0/13

Median OS was 15.8 months for the control cohort and 18.5 months for the belinostat cohort (p = 0.53). Comparison of OS curves for the two cohorts are shown in **Figure 7.2A**. 6-month PFS was 54% and 84% (p = 0.073) for the control and the belinostat cohorts, respectively, reported previously [12]. The median PFS was 9.0 months for the control and 9.3 months for the belinostat cohorts (p = 0.75).

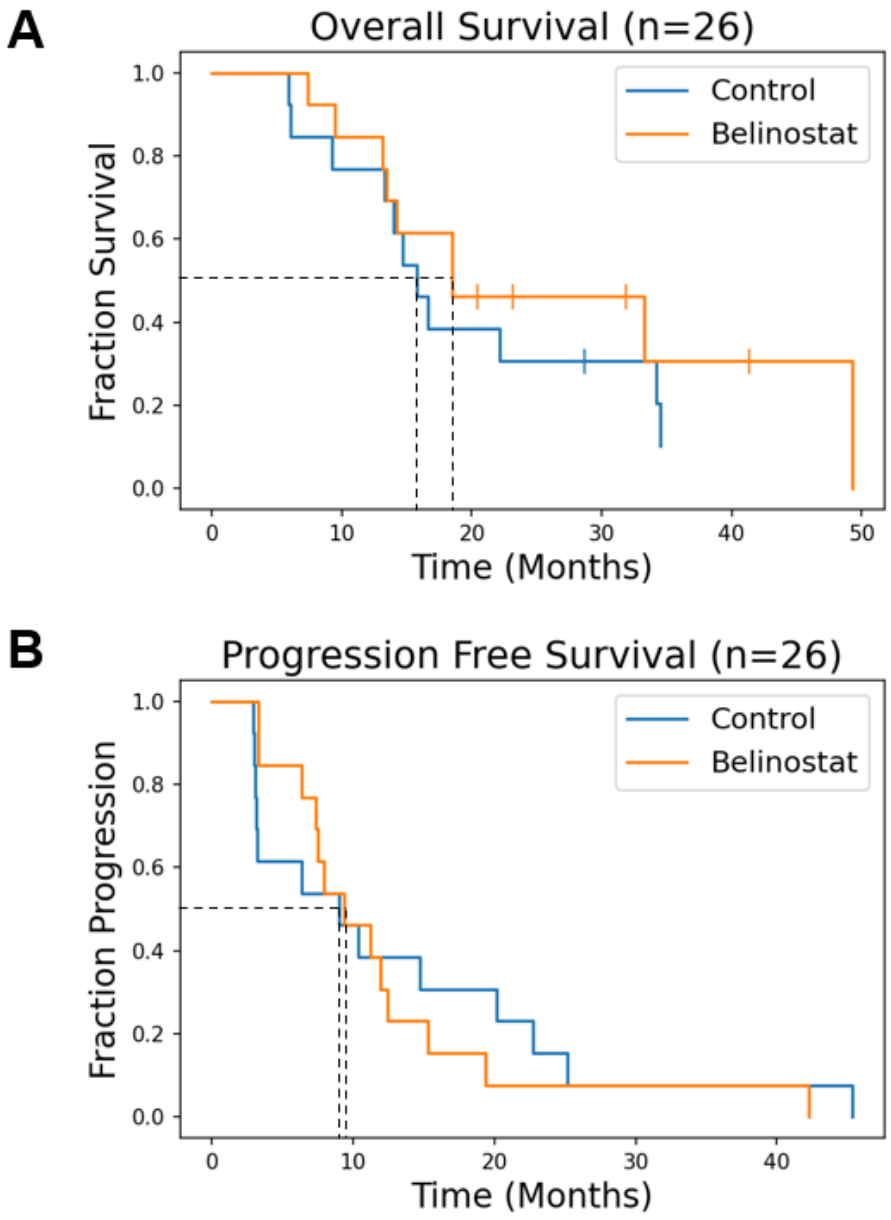

Figure 7.2. (A) Overall Survival (OS) Kaplan-Meier Survival Curves. The median OS for the control and belinostat cohorts was 15.8 and 18.5 months, respectively (p = 0.53), for all patients. (B) Progression free survival (PFS) for all patients. The median PFS for control and belinostat cohorts was 9.0 months and 9.3 months, respectively (p = 0.75).

7.3.2 Radiation Overlap Statistics

To gain a greater understanding of enhancing recurrence patterns relative the radiation dose distribution in study patients, we determined the actual dose received by the

region of recurrence. The minimum, maximum, and mean radiation dose to rGTV, the percentage of rGTV that occurred in PTV1, and the percentage of rGTV that occurred in PTV2 for each patient enrolled in the trial was determined and is listed in **Table 7.2**. For example, for patient QINU01EM008, the minimum, maximum, and mean radiation dose to rGTV was 11.8 Gy, 64.7 Gy, and 58.7 Gy, respectively. For that same patient, 90.9% of the rGTV recurrence volume occurred within the PTV1 treatment contour while 69.9% of the recurrence occurred within PTV2. This would suggest that for this patient, most of the recurred lesion was within the PTV radiation targets. For the control versus the belinostat cohort, the minimum, maximum, and mean radiation dose to rGTV was on average 54.6 versus 45.0 Gy (p = 0.20), 64.1 versus 57.9 Gy (p = 0.11), and 62.0 versus 51.5 Gy (p = 0.042), respectively. For the control versus the belinostat cohorts, the mean percentage of rGTV within PTV1 and PTV2 was 99.3% versus 73.9% (p = 0.052) and 97.1% versus 69.0% (p = 0.034), respectively. While all control patients had in-field failure as the site of first recurrence, only ten out of 13 belinostat patients failed in-field initially. **Figure 7.3** illustrates out-of-field failure in the three remaining belinostat patients (cohort 2). For those patients, there were regions of rGTV that fell squarely within the PTV1 and PTV2 contours, illustrating instances of failure "in-field" of radiation. However, these three cases also show instances where rGTV was either completely outside of the PTV contours or spread from outside of the PTV contours (as suggested by the red arrows).

Table 7.2. Minimum, maximum, and mean radiation dose to recurrence volume (rGTV), overlap between rGTV and PTV1, and overlap between rGTV and PTV2.

Study ID	Minimum Dose (Gy)	Maximum Dose (Gy)	Mean Dose (Gy)	rGTV Overlap with PTV1	rGTV Overlap with PTV2
Cohort 1					
QINU01EM001	59.0	65.2	62.3	100.0%	100.0%

QINU01EM002	61.1	63.4	62.4	100.0%	100.0%
QINU01EM003	59.4	63.8	61.8	100.0%	100.0%
QINU01EM004	61.9	64.5	63.1	100.0%	100.0%
QINU01EM005	60.3	63.5	62.5	100.0%	100.0%
QINU01EM006	61.1	64.2	62.5	100.0%	100.0%
QINU01EM007	60.2	63.6	62.0	100.0%	100.0%
QINU01EM008	11.8	64.7	58.7	90.9%	69.9%
QINU01EM010	52.2	64.7	62.3	100.0%	99.1%
QINU01EM011	44.1	64.7	62.2	99.8%	99.5%
QINU01EM012	58.7	63.6	61.9	100.0%	94.5%
QINU01EM013	59.0	64.1	61.8	100.0%	100.0%
QINU01JH001	60.1	63.2	61.4	100.0%	99.8%
Cohort 2					
QINU01EM014	52.2	63.2	58.2	100.0%	50.1%
QINU01EM015	58.7	62.8	61.2	100.0%	96.2%
QINU01EM016	56.2	64.9	62.8	99.2%	99.2%
QINU01EM017	10.9	50.3	25.2	0.0%	0.0%
QINU01EM019	60.2	63.2	61.6	100.0%	100.0%
QINU01EM021	*	*	*	*	*
QINU01EM022	59.6	62.8	61.0	100.0%	100.0%
QINU01EM023	45.6	53.4	50.3	0.0%	0.0%
QINU01EM024	59.5	63.8	61.6	100.0%	100.0%
QINU01JH002	60.0	62.1	61.0	100.0%	100.0%
QINU01JH003	1.9	63.8	32.3	13.4%	13.4%
QINU01EM025	19.8	21.7	20.9	100.0%	100.0%
QINU01EM026	*	*	*	*	*

*****Follow-up imaging was not available for recurrence analysis

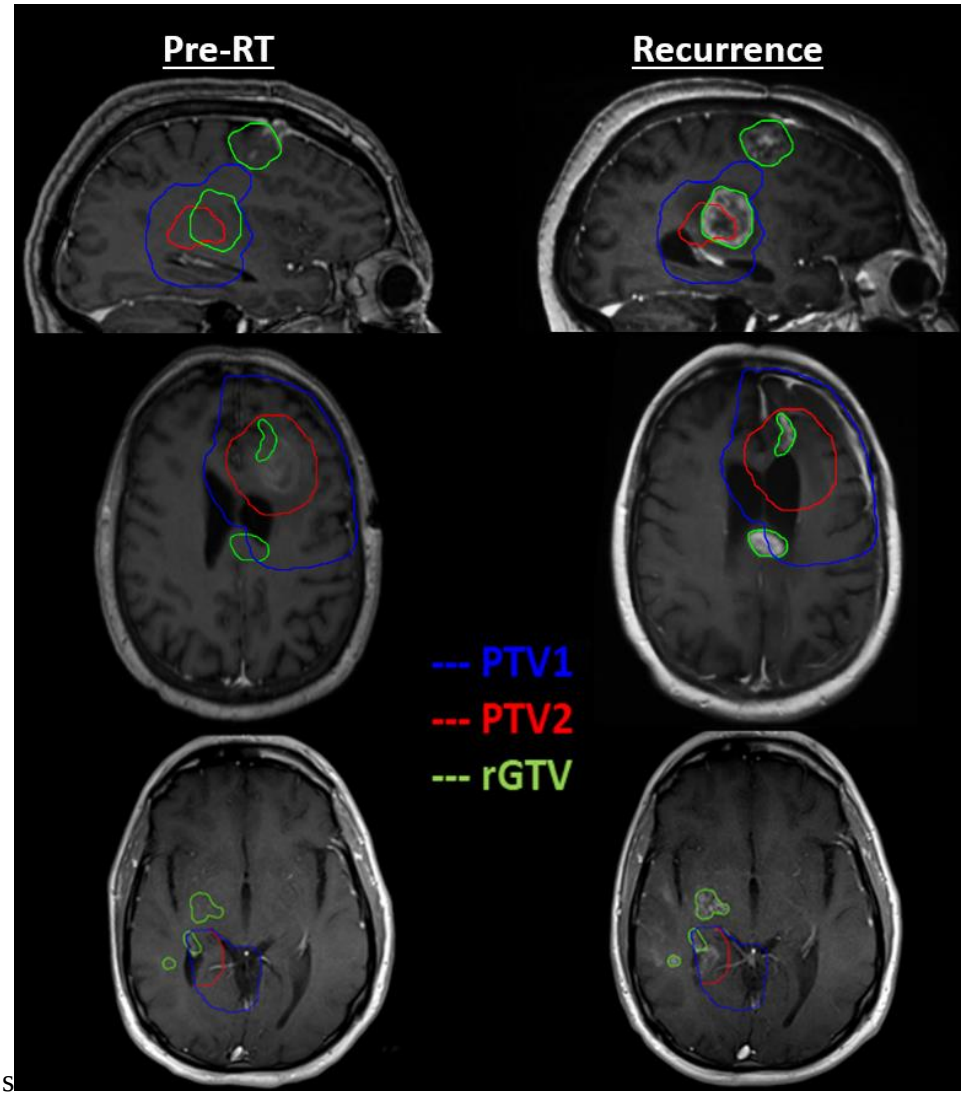

s

Figure 7.3. T1 post-contrast imaging in three patients, by horizontal row, with out of field recurrence in cohort 2. For each patient, the enhancing recurrence contour (rGTV) encompasses lesion that has spread outside the extent of radiation treatment targets PTV1 (guided by T2/FLAIR) or PTV2 (guided by T1w-CE).

7.3.3 Recurrence Analysis and Toxicities

In **Figure 7.4**, we sought to explore why three patients in the belinostat cohort had worse outcomes than historical controls. We investigated Cho/NAA abnormalities in these patients' pre-RT sMRI scan as Cho/NAA is a sensitive marker for regions at risk of recurrence [22]. The contours in the first column of **Figure 7.4** depict the margin of two-

fold or greater elevations in the Cho/NAA ratio (compared to the contralateral normal-appearing white matter). In the second column these are overlaid on the standard contrast enhanced MRI images to show the substantial difference between what is usually recognized as residual tumor and regions that predict tumor extent by Cho/NAA. This level of Cho/NAA elevation equates to a mean Z-score of 6.62 as reported previously (with >99.999% confidence) [12]. In the third column, the margins for the two-fold or greater elevations in the Cho/NAA ratio are overlaid on FLAIR images. This shows somewhat greater but still incomplete concordance with the extent of the tumor predicted by the Cho/NAA ratio.

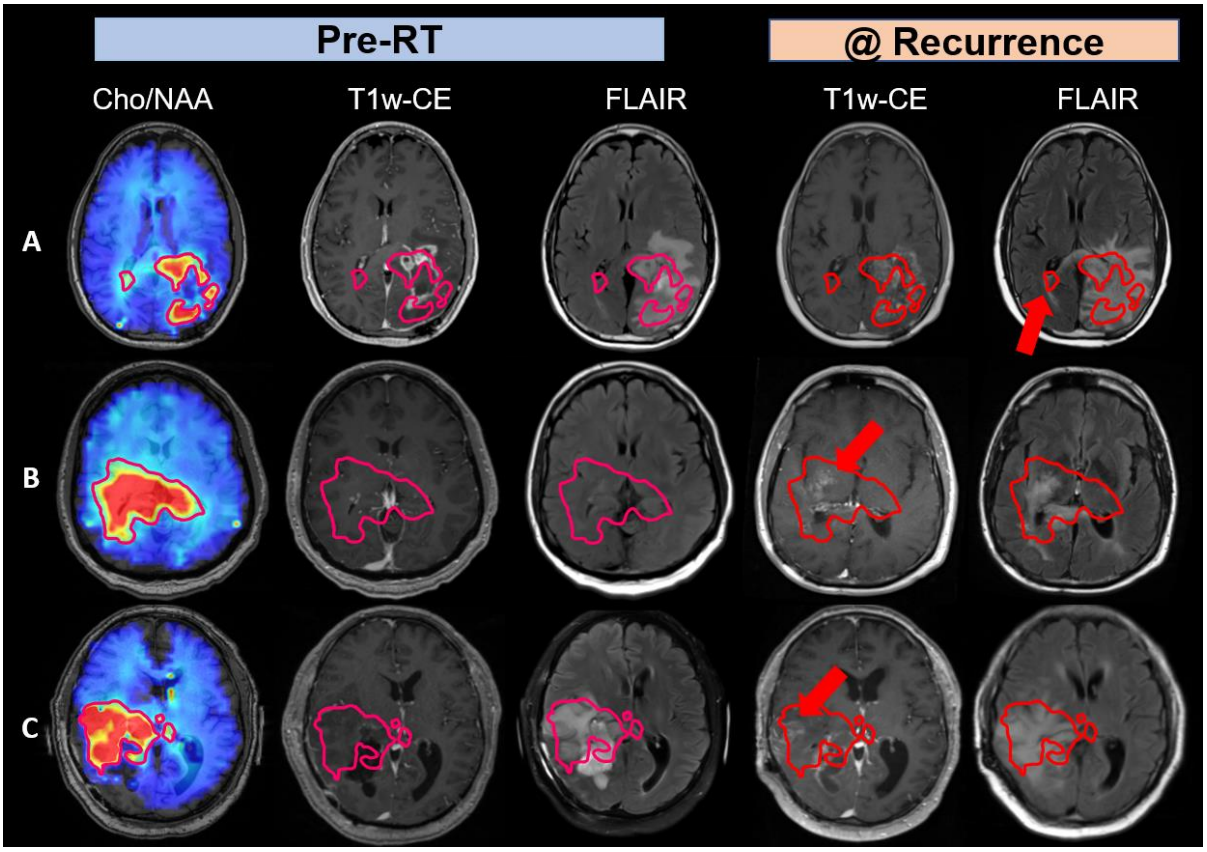

Figure 7.4. Pre-RT sMRI scans suggest out-of-field recurrence in the belinostat cohort with tumor infiltration beyond what is shown in standard imaging. (**A**) This patient had two-fold Cho/NAA elevation that had spread contralaterally. While pre-RT standard imaging failed to detect this, FLAIR hyperintensity at recurrence mimics the direction of

tumor infiltration detected by pre-RT sMRI. (**B**) The second patient had tumor infiltration across the midline that wasn't detected by pre-RT standard imaging. Lesions at recurrence in both T1w-CE and FLAIR MRIs confirm Cho/NAA abnormalities in the pre-RT sMRI scan, suggesting standard imaging underestimated the extent of tumor infiltration. (**C**) This patient had a large lesion of metabolically active tumor that was not shown in T1w-CE, thus, undertreated, which became apparent at recurrence.

Axial slices in **Figure 7.4** were chosen to most emphasize regions of tumor recurrence that were detectable in pre-RT Cho/NAA imaging. In row 4A, Cho/NAA elevation showed tumor spreading to the contralateral side through the corpus callosum, which wasn't apparent in pre-RT T1w-CE or FLAIR MRIs, and thus was not treated within the radiation treatment plan. At recurrence, FLAIR hyperintensity had spread contralaterally in a similar direction to the Cho/NAA abnormality confirming tumor infiltration that was not treated during RT. In row 4B, the pre-RT Cho/NAA abnormality crosses the midline, which wasn't apparent in T1w-CE or even in FLAIR MRIs. Less than a year after RT, recurrence patterns with standard imaging confirmed findings in the pre-RT sMRI scan with both enhancement and FLAIR hyperintensity apparent within the pre-RT Cho/NAA contour. For this patient especially, the morphology of the T1w-CE and FLAIR lesions evolved throughout the follow-up period to approximate the morphology of the pre-RT Cho/NAA abnormality. In row 4C, the pre-RT Cho/NAA abnormality spread widely anterior to the resection cavity, which was not visible in T1w-CE. Thus, this elevated Cho/NAA ratio abnormality was incompletely treated with high dose radiation. The recurrence pattern confirmed the findings in the pre-RT sMRI scan. The T1w-CE and FLAIR studies demonstrate increasing enhancement evolved throughout the follow-up period to approximate the morphology of the pre-RT Cho/NAA ratio abnormality. In summary, these three cases suggest that standard imaging underestimates the true extent of tumor infiltration, causing these patients to be undertreated and have a lower survival.

When excluding these three patients, the median OS of the belinostat cohort increases to over 30 months.

Treatment with belinostat given at a dose of 750 mg/m^2/day × five days every three weeks during week zero (pre-RT) as well as week three and week six of RT resulted in dose limiting toxicities (DLTs) (two with grade 4 thrombocytopenia and one with grade neutropenia) in two of three patients. However, after de-escalation of the belinostat dose to 500 mg/m^2/day in the remaining cohort patients, no further DLTs were experienced. Significant toxicities (grade 3 or greater) that were judged to at least possibly be due to therapy for our control and belinostat cohorts are summarized in **Table 7.1**. Overall, the addition of belinostat at the 500 mg/m^2/day dosing to concurrent RT/TMZ appears to be well tolerated.

7.4 DISCUSSION

Here, we report the final results of a pilot study adding belinostat to concurrent RT and TMZ for patients with newly diagnosed GBMs [131]. Previously, the cohort receiving belinostat showed an improved six-month PFS compared to the control cohort (54% vs. 84%, p = 0.073). In **Figure 7.2B**, the beneficial effects of belinostat delaying tumor progression appear to decline by month nine. A speculated reason for the improved PFS at six months but not by nine months is that belinostat was only given to subjects for a short duration throughout RT. HDACis such as belinostat are known to be reversible drugs, with epigenetic stress in tumors and the microenvironment resuming in the absence of HDACis resulting in a truncated effect. In our final analysis, the median overall survival was promising appearing slightly longer (by about 2.7 months) for the belinostat cohort. While

the result is not statistically significant, this may be in part due to the small sample size. In a recent cooperative group trial (NRG-BN001) comparing dose-escalated to conventional dose RT for newly diagnosed GBM patients, patients on the experimental arm that received dose-escalated photon radiation had a median OS of 18.7 months [42]. The similarity in median OS benefit between the dose-escalated treatment arm of BN001 and our belinostat cohort points to the potential of belinostat possibly having a radiation sensitizer effect on patients comparable to dose escalation. In our trial, the voxel-based analysis of recurrence patterns comparing recurrent voxels to those in PTV2 indicates a potential shift of recurrences being more out-of-field suggesting that in-field control was improved due to the radiosensitizing effects of belinostat.

Pre-RT sMRI scans for a few representative belinostat patients reveal larger tumor extents (median volume difference was 6.2-fold between union of Cho/NAA $\geq$ 2*x and residual tumor vs. residual tumor volume in all belinostat group patients) than were detected in standard imaging. Therefore, these portions of the lesion (as defined by Cho/NAA) were left undertreated. RT plans for all patients on the trial were guided by abnormality in T1w-CE and FLAIR only. Recurrence patterns confirm that pre-RT sMRI findings provide a possible reason for some in the belinostat cohort having an OS that was lower than that in historical controls. Due to the initial study design, we were only permitted to perform sMRI scans up to four weeks after completion of radiation therapy. In the future, we hope to include the sMRI sequence during patient follow-up as it is a valuable predictor of tumor infiltration extent.

The wide variability in OS suggests that some patients respond much more positively to a belinostat regimen while for others, the effect is minimal. While HDAC

inhibitors are powerful epigenetic modulators, they are still target-specific drugs. They are hypothesized to work in the subgroup of patients whose tumorigenesis is driven by epigenetic modifications. This encourages investigation into whether certain subtypes of GBMs are more genetically predisposed to react positively to HDACi's like belinostat. Unfortunately, our sample size was too small to identify molecular subtypes that were responsive to belinostat. Interestingly, one patient with an IDH mutation who responded remarkably well to belinostat [132]. With this patient, there was not only a visible size reduction of metabolically active tumor volume but also the metabolic activity in the contralateral side of the brain was restored to healthy levels. This supports the observations reported by other groups that IDH1/2 mutations in grade IV astrocytomas are associated with a fascinating link to 2-hydroxyglutarate (2-HG) accumulation representing an altered metabolite profile, which may have broad implications for both cancer epigenetics and clinical management of disease [136]. While it is difficult to run a clinical trial in grade IV astrocytomas with IDH mutation in a single institution since the incident rate is low, it may be beneficial to run a multisite trial to determine if grade IV astrocytomas with IDH mutation are unusually sensitive to belinostat.

Patients receiving belinostat on our study appear to have a different recurrence pattern than those in the control cohort. In particular, the mean radiation dose to the rGTV region was statistically significantly lower in the belinostat cohort than that in the control cohort (51.5 Gy vs. 62.0 Gy, $p = 0.042$) while other comparisons of the minimum and maximum dose to rGTV were similarly trending in the same direction. This suggests that concurrent belinostat may be delaying recurrences in regions that received higher radiation doses. The overlap between rGTV and PTV treatment zones was also lower in the

belinostat cohort than that in the control cohort. In particular, the mean overlap between rGTV and PTV2, which received the highest dose of radiation, was significantly lower in the belinostat patients than that for the control (69.0% vs. 97.1%, $p = 0.034$). Overall, these trends look promising for belinostat's activity in GBM especially in concert with full dose RT. This is further supported by the three patients in the belinostat cohort that had out-of-field recurrence as the first site of recurrence. In them the belinostat was unable to significantly impede recurrences when RT dose was inadequate.

Finally, the addition of belinostat to concurrent RT/TMZ at a dose of 750 mg/m^2/day x five days every three weeks starting one week prior to RT did result in DLTs in two of three patients that completed this therapy. In one case, grade 4 thrombocytopenia first developed just prior to cycle one of adjuvant TMZ. In the other case, grade 4 thrombocytopenia and neutropenia did not develop until after receiving three cycles of adjuvant TMZ (more than four months following the last treatment with belinostat). While it is possible that these were spurious events as these hematologic toxicities can occur with TMZ alone, the lack of hematologic DLTs in our control cohort (N = 13) and the remaining belinostat cohort (N = 10) treated at 500 mg/m^2/day argues for implicating belinostat in these DLTs. Also, at the lower belinostat dose, no unusual toxicity was definitively noted. Thus, based on our limited experience, the dosing regimen of three cycles of belinostat at 500 mg/m^2/day x five days every three weeks during concurrent RT/TMZ is well tolerated and should serve as a point of departure for dosing in future trials evaluating belinostat in combination with RT and TMZ.

Due to limitations in the study including a small sample size in each cohort, a wide range of survival responses to belinostat, as well as toxicities from initially larger doses of

administered belinostat, future work will require larger cohorts with manageable belinostat dosing regimens to discern the true effect size of this treatment. In this trial, belinostat was only administered during RT. Since an HDACi such as belinostat is a reversible drug and epigenetic modification-induced stress remains, we hypothesize that extended use of belinostat during the maintenance period after radiation therapy may further improve outcomes in patients. This will require future testing to assess the safety and efficacy of belinostat when combined with adjuvant TMZ. Based on the results of this pilot study, we are planning a multisite trial with a larger cohort of patients that will also including maintenance belinostat after sMRI-guided radiation treatment.

7.5 CONCLUSION

In summary, we have established that belinostat can be safely given with concurrent RT and TMZ and is trending towards improving outcomes in newly diagnosed GBM patients. Since recurrence volumes in the control cohort had larger overlap with PTV2s (volume receiving 60 Gy) than in the belinostat cohort, this suggests that belinostat has a better likelihood of delaying recurrence in those regions receiving 60 Gy. Trends in this study highlight the potential of belinostat, a BBB-penetrating HDACi, as a synergistic therapeutic agent for GBM treatment.

Chapter 8. The Utility of Spectroscopic MRI in Stereotactic Biopsy and Radiotherapy Guidance in Newly Diagnosed Glioblastoma

8.1 INTRODUCTION

Gliomas represent one of the most prevalent types of central nervous system neoplasm in the United States. Initial glioma management relies on standard MRI, in which T1-weighted contrast-enhanced (T1w-CE) imaging is heavily used to determine tumor extent and pathologic assessment. While maximal resection is preferred, many patients will only undergo more limited biopsy due to tumor size and location, particularly when there is involvement of areas of eloquent brain. Contrast-enhancement indicates areas of blood-brain barrier disruption and leaky tumor neovasculature, which is the hallmark of high-grade gliomas. When initial diagnosis is obtained by stereotactic sampling of a small portion of the tumor, pathological determination may be subject to sampling error leading to tumor mistyping, under-grading or even nondiagnostic specimens [137]. Areas of contrast enhancement are typically used to define biopsy targets, but non-enhancing gliomas can be anaplastic (grade 3) in up to a third of cases and standard imaging becomes an unreliable predictor of tumor grade [138,139]. In non-enhancing gliomas, biopsy is traditionally taken from areas of hyperintensity on T2-weighted (T2w) and/or FLAIR (fluid-attenuated inversion recovery) images [15]. However, T2w/FLAIR hyperintensity is nonspecific and cannot differentiate non-enhancing tumor from edema, gliosis, radiation effects, ischemic injury, and infection [15,57]. These major pitfalls in standard diagnostic imaging create practical limitations in surgical biopsy of gliomas.

Because of the limitations with standard MRI, many additional advanced MR techniques have been proposed to facilitate biopsy guidance [140,141]. One of these techniques, whole-brain 3D spectroscopic MRI (sMRI), a type of magnetic resonance spectroscopic imaging, identifies the spatial distribution of endogenous metabolites and has shown benefit in glioma grading and differentiating tumor from non-tumor [142-144]. Several metabolites can be reliably evaluated with sMRI including choline-containing compounds (Cho), membrane components which are nearly always elevated in gliomas; creatine (Cr), an energy metabolite; N-acetylaspartate (NAA), a marker of healthy neurons; and myo-inositol (mI), a precursor of many secondary messaging molecules [145]. Early studies established that the spectra of brain tumors differ significantly from normal brain [12,146,147]. Increased levels of Cho and decreased levels of NAA are associated with tumor, suggesting that sMRI can be clinically useful in identifying tumor cells [18,20,43,146-148]. T1w-CE and in T2w/FLAIR fail to capture these tumor regions that are detected by sMRI [12]. In a study published in 2016, sMRI was combined with 5-aminolevulinic acid fluorescence guided stereotactic tissue extraction to find that Cho/NAA abnormal regions were significantly correlated with two major quantitative measures of pathological tissue infiltration: SOX2 density and *ex-vivo* fluorescence [12]. In another small cohort study with 10 patients, we demonstrated that sMRI can be predictive for subsequent recurrence in patients with WHO grade II and grade III gliomas. Specifically, the report establishes that regions of elevated Cho/NAA ratios compared to normal appearing white matter on the contralateral side of the brain serve as reliable imaging biomarkers for low-to-intermediate grade gliomas [13]. In glioma grades where contrast-enhancement is typically absent, this tumor marker becomes extremely valuable. At our institution, sMRI has been used as an

adjunct tool for image-guided biopsies in lower grade gliomas, including WHO grade II and grade III tumors. These heterogenous tumors typically present without consistent contrast enhancement on MRI, complicating optimal target planning for stereotactic biopsies and high dose radiation therapy. For selective challenging cases, we utilize sMRI to supplement conventional clinical MRI to increase the accuracy of stereotactic biopsy and obtain the most anaplastic glioma cells. Previous studies have shown that using a five-fold increase in Cho/NAA (Cho/NAA ≥ 5X) compared to normal appearing white matter maximizes the tumor density within the target site [13]. Using our in-house cloud platform, the Brain Imaging Collaboration Suite (BrICS), we are able to create sMRI target volumes for a variety of clinical purposes (i.e., radiotherapy, surgery, and diagnostic biopsy) [32,52]. In this report, we present an example of one of our routine sMRI-guided biopsies to establish the importance and strength of utilizing metabolite mapping for diagnostic biopsies.

Imaging techniques that can be validated with pathology, surgery, and biopsy are strong candidates to guide RT planning. sMRI has the potential to serve as the primary imaging technique for patients with GBM to guide their care from diagnosis to every stage of therapy. There is an urgent need to improve the current standard of care for GBMs which, currently guided by standard MRI, involves maximal safe neurosurgical tumor removal, followed by a course of radiation therapy (RT) combined with concurrent and subsequent administration of the chemotherapy agent temozolomide (TMZ) [40,149]. Despite this comprehensive treatment strategy, the median overall survival (OS) for GBM patients remains approximately 16 months [10,58]. There is mounting evidence that sMRI is a superior imaging biomarker compared to T1w-CE imaging for RT and can impact

survival outcomes positively [34]. For RT targeting, our previous work determined that a two-fold increase in Cho/NAA ratio compared to normal appearing white matter on the contralateral side of the brain (Cho/NAA ≥ 2X) can be used to detect regions of significant tumor infiltration [12,21]. Another avenue to improve the current treatment protocol for GBM involves the utilization of histone deactylase inhibitors (HDACi) which have been shown to improve outcomes in patients with gliomas [126,132]. This report performs a retrospective analysis on a two-site pilot study (NCT02137759) in which newly diagnosed GBM patients were treated with standard-of-care chemoradiation concurrently with belinostat, an HDACi. Belinostat, a reversable epigenetic drug, has been shown to possess among the best blood-brain barrier penetration properties among HDACi currently being investigated [128]. The primary outcomes of NCT02137759 found that median OS was not significantly different between the belinostat cohort (18.5 months) and control cohort (15.8 months). However, recurrence analysis suggested that patients treated with belinostat were less likely to have disease progression within the field of treatment, which shows a radiosensitizing effect [22]. We hypothesize that one possible reason for OS not being significantly increased by the addition of belinostat is due to inadequate targeting of the tumor with standard MRI. In this paper, we investigate whether there is a relationship between undertreated tumor detected by sMRI and OS for patients treated with belinostat in the NCT02137759 pilot study. We also conducted a unique volumetric analysis to elucidate recurrence patterns in relation to our Cho/NAA ≥ 2X volume and standard MRI-derived treatment volumes. We hypothesize that tumor recurrence will occur in areas not targeted by standard MRI but demarcated by our sMRI biomarker.

8.2 METHODS

8.2.1 Stereotactic Biopsy

We identified a patient who required a stereotactic needle biopsy to characterize progression of her disease seen on standard imaging. The patient was a 36-year-old female previously diagnosed with WHO grade II astrocytoma with IDH mutation with a sub-total resection. On subsequent surveillance imaging, findings suggested progression and stereotactic needle biopsy was recommended. Whole-brain 3D echo-planar spectroscopic imaging (EPSI) and accelerated with Generalized Autocalibrating Partial Parallel Acquisition (GRAPPA) parallelization and elliptical k-space encoding (TE/TR/FA = 17.6ms/1551ms/71°) on a Siemens 3-Tesla MRI scanner using a 32-channel head coil array (PRISMA, Siemens Healthineers, Erlangen, Germany) [50]. Padded foam blocks were used to stabilize the head and reduce motion related artifacts. First-order shims were optimized to a waterline width of 25 Hz while lipid signal was nulled using outer-volume suppression with manually placed saturation bands using the Syngo software [12]. Tissue water signal was collected in an interleaved manner with the metabolite data for signal normalization and image registration. The scan time was 15 minutes with a nominal voxel size of 314 µL, an FOV of 280 mm x 280 mm x 180 mm, and a matrix size of 50 x 50 x 18. The raw data was processed using the Metabolite Imaging and Data Analysis System (MIDAS) (University of Miami) to obtain metabolite maps with an interpolated voxel size of 4.4 x 4.4 x 5.6 mm^3 (effective resolution of 0.1 mL) and imported into BrICS *[50,51,61]*. At the same session, a non-contrast T1-weighted 3D magnetization-prepared rapid-acquisition gradient echo (MPRAGE, 1 mm^3, TR/TE/FA = 2300 ms/3.4 ms/9 degrees) and 3D

T2w/FLAIR images (TR/TE/FA = 4800 ms/441 ms/120 degrees) with 1 mm isotropic voxels were obtained. T1w-CE with the same parameters as the non-contrast T1w sequence images were acquired at a different date prior to sMRI. Within BrICS, the sMRI images, T2w/FLAIR and T1w-CE were registered to the non-contrast T1w image acquired on the same date as the sMRI. A target biopsy volume was created using a Cho/NAA ≥ 5X threshold. The 5X volume was chosen to maximize tumor density and increase chances for a successful tumor sample acquisition. The volume mask and registered T1w-CE MRI were imported into the Medtronic Stealth S8 system for biopsy planning. A high-resolution CT image with voxel size of 1 mm^3 was acquired prior to the biopsy to provide a high-resolution image for registration of the skull. The CT image was registered to the T1w-CE image within the Medtronic system prior to the biopsy.

8.2.2 Tumor Volume Determination (NCT02137759)

The retrospective analysis of this report utilized data from 13 patients within the belinostat cohort of the NCT02137759 study, all of whom had pathologically confirmed, newly diagnosed grade IV GBM. Patients were enrolled from two clinical sites, Emory University(n=11) and Johns Hopkins University (n=2). Emory University patients were imaged on a Siemens 3T TIM/TRIO scanner (Siemens Healthineers, Erlangen, Germany) and Johns Hopkins patients were imaged on a Philips 3T Achieva scanner (Philips Healthcare, Massachusetts, United States). Whole-brain 3D EPSI was acquired with GRAPPA parallelization and elliptical k-space encoding (TE/TR/FA = 17.6ms/1551ms/71°). A non-contrast and gadolinium contrast T1-weighted 3D MPRAGE (1 mm^3, TR/TE/FA = 2300 ms/3.4 ms/9 degrees) were acquired. T2w/FLAIR images (TR/TE/FA = 10000 ms/121 ms/90 degrees) was also obtained. In accordance with the

updated 2021 WHO definition of grade IV GBM, one patient from Emory University with an IDH mutation was excluded from our retrospective analysis *[59]*. All patients underwent maximal safe surgical resection before enrolling in the study. Patients received standard treatment including daily TMZ at a dosage of 75 mg/m^2 and focal radiation. The gross tumor volume 1 (GTV1) was created utilizing abnormal FLAIR signals and the gross tumor volume 2 (GTV2) was created using T1w-CE enhancement and included the resection cavity. Clinical tumor volumes (CTV1 and CTV2) were created by adding margins of 5 mm to the GTVs. To accommodate microscopic disease spread and treatment uncertainty, another 3 mm margin was added to create planning treatment volumes (PTV1 and PTV2). The specific margin added to the CTV and PTV is determined by the physician and depends on the patients' clinical characteristics, location of the tumor, and proximity to vital organs (brain stem, pons, medulla etc.) which cannot be targeted with radiation. For this analysis, the margins added were kept as close as possible to those listed above for both the CTV creation and PTV creation. Focal radiation doses of 51 Gy were delivered to PTV1 and 60 Gy to PTV2 for each patient. All treatment volumes were verified by a board-certified radiation oncologist and pre-RT T1w-CE lesions were verified by a board-certified neuroradiologist. Patients also received daily intravenous doses of belinostat for five consecutive days in three cycles, three weeks apart, starting one week before chemoradiation [21,22].

Patients were subsequently followed using standard MRI scans (T1w-CE and FLAIR) every two months for a period of 12 months after RT or until there was evidence of disease progression on radiographic imaging. Tumor progression dates were determined for each patient using criteria defined by the Brain Tumor Reporting and Data System (BT-

RADS) and physician interpretation *[30,31,53,109]*. Each patient's T1w-CE scans obtained at the radiological progression dates were co-registered to the MRIs that were initially used for RT planning. The recurrence volumes (rCE), as determined by these follow-up T1w-CE images, were created by manual delineation of areas of abnormal enhancement present in scans obtained during monitoring of their diseases. All rCEs were verified by a board-certified neuroradiologist. Image registration was performed using the Python SimpleITK library *[150-152]*. Manual lesion segmentation was performed in BrICS.

This study used sMRI sequences collected prior to RT treatment. sMRI was acquired with 3T MRI scanners using a 32-channel head coil array (Siemens Healthineers or Philips Healthcare) with same parameters described above *[50]*. Raw data was processed using MIDAS *[50,51,61]*. sMRI lesion volumes were created in BrICS with Cho/NAA ≥ 2x as the threshold *[52]*. sMRI lesions volumes were independently verified by two MRSI experts for SNR and artifacts before and during generation of the 2X volumes. The treating radiation oncologist in collaboration with a neuro-radiologist would verify and make minor adjustments to the treatment volumes to optimize clinical care by removing apparent artifacts and reducing coverage of potential at-risk structures.

8.2.3 Statistical Analysis/Survival Analysis

For the 12-patient cohort, the difference was taken between lesion volumes from Cho/NAA ≥ 2x and pre-RT T1w-CE. The cohort was then split into two subgroups using the median difference of 16.1 cc as the cutoff. The High-Mismatch Group had a larger volume difference between Cho/NAA ≥ 2x and T1w-CE compared to the median difference. The Low-Mismatch Group had a lower volume difference between Cho/NAA ≥ 2x and T1w-CE compared to the median difference. The Kaplan-Meier estimator was

used to calculate survival curves based on OS after a median follow-up time of 50 months. The Kaplan-Meier curves generated for each group were compared using a log-rank test. Finally, the R-squared correlation coefficient was calculated between lesion volumes from T1w-CE and Cho/NAA ≥ 2x. Statistical analysis was performed using the Python *lifelines* library **[55]**.

We also conducted an analysis of the total amount of rCE that was found in our pre-RT sMRI Cho/NAA 2X volumes for 11 patients in the cohort that had imaging from at least two follow-up visits. All post-progression dates were rigidly registered to images acquired at the date of progression. We then calculated the volume of rCE that was not included in the GTV2 or CTV2. Our equation to determine this volume is shown below with GTV used as an example.

$$\boldsymbol{rCE_{ExcludeGTV} = rCE \cap (GTV)'}$$

Using this volume, the total overlap with the pre-RT Cho/NAA ≥ 2x volume was calculated to determine the percentage of recurred voxels outside of high-dose radiation targets derived from standard imaging, that fall within pre-radiation sMRI targets. The equation for the percentage of rCE that intersected with Cho/NAA ≥ 2x is shown below. See Figure 8.1 for a graphical depiction.

$$\boldsymbol{Overlap}\ (\%) = \frac{\boldsymbol{rCE_{ExcludeGTV} \cap \left(\frac{Cho}{NAA} \geq 2X\right)}}{\boldsymbol{rCE_{ExcludeGTV}}}$$

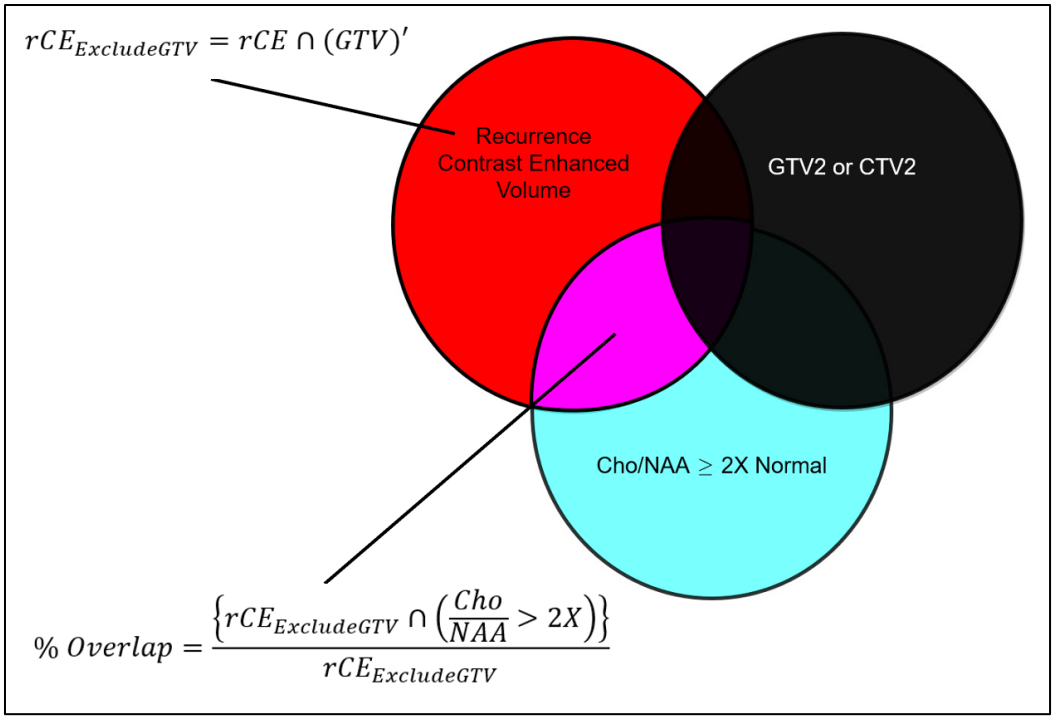

Figure 8.1. Graphical depiction of the calculations performed for overlap analysis. The goal of our analysis was to quantify the region of overlap (purple) between the recurring contrast enhanced volume (red) and Cho/NAA ≥ 2X excluding (light blue) the original treatment volume (GTV2 or CTV2), depicted in black. This would allow us to infer the capability of pretreatment sMRI in predicting areas of subsequent recurrence.

Paired T-tests were used to compare the different groups. All volumes are presented in cubic centimeters (cc). For each group, volumes are presented as mean ± standard deviation.

8.3 RESULTS

8.3.1 Stereotactic Biopsy

Figure 8.2 shows the standard MRI and Cho/NAA metabolite map for a case with ill-defined margins for biopsy. The lack of enhancement in T1w-CE and large T2w/FLAIR volume complicates the process of selecting an accurate biopsy target. Using BrICS, an ideal target zone of 4.9 cc for stereotactic biopsy was created using Cho/NAA ≥ 5X. The

3D contour of the 5X volume from BrICS shows the region with the highest density of tumor within the T1w image. The 5X contour was chosen as the biopsy target as previous studies have shown that it provides the maximal tumor density (close to 100% tumor) and provides surgeons with the highest chance of obtaining a tumor sample [12].

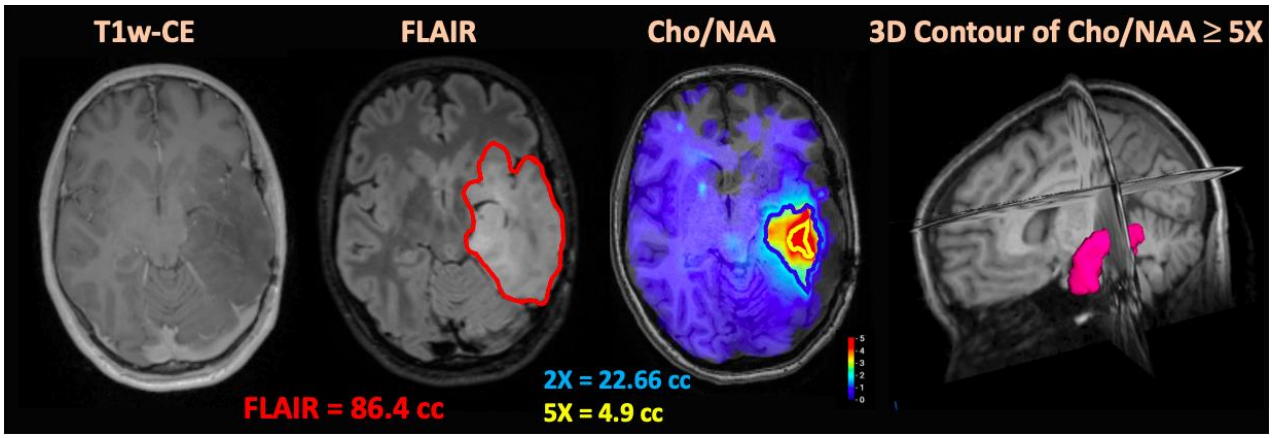

Figure 8.2. Patient with low grade glioma presented for repeat biopsy to assess possible disease progression. Due to lack of enhancement in CE-T1w and difficulty finding the areas most suspicious for progressive tumor within the FLAIR volume, sMRI was utilized to better delineate target for biopsy. As noted, the FLAIR volume (red) of 86.4 cc is too large to allow for adequate targeting during surgical biopsies. Cho/NAA ratio five times (yellow) abnormal was instead utilized to delineate biopsy target. The 3D contour of Cho/NAA ≥ 5X (yellow) and Cho/ NAA ≥ 2X (blue) is shown for comparison. The 2X volume is typically used for radiation-treatment while the 5X threshold maximizes tumor density and probability of a successful biopsy. All images are displayed in our in-house program, the Brain Imaging Collaboration Suite (BrICS).

Figure 8.3 shows the 5X volume and registered MRI in the Medtronic S8 Stealth® Navigation Tool. The tissue sections obtained showed an infiltrating glioma with mixed morphology, tumor cells with both rounded and oblong hyperchromatic nuclei and moderate atypia and scattered mitotic figures. Due to the features present in the biopsy, the patient was reclassified from a grade II IDH-mutant to a grade III IDH-mutant astrocytoma

ultimately leading to a change in her treatment plan. This case underscores the significance of employing precise and specific imaging biomarkers to inform diagnostic procedures.

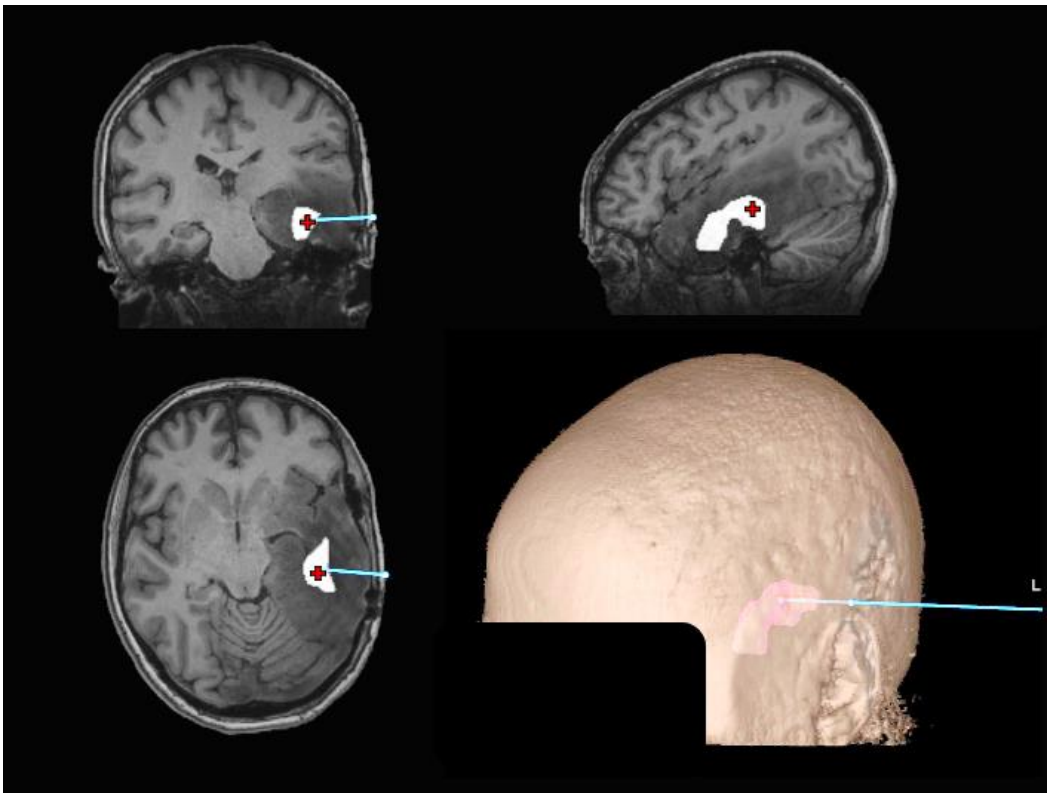

Figure 8.3. Medtronic S8 Stealth® Navigation Tool with 5X Cho/NAA biopsy target displayed. Entry point coordinate was (72, 15, -14) and target point, depicted by the red crosshair, was at coordinates (36, 12, -15) in MRI DICOM space. Total travel distance was 36.1 mm to reach target volume. The blue line shows the projected travel of the needle. The patient's face is obscured for anonymity.

8.3.2 NCT02137759 Retrospective Analysis

The retrospective analysis was performed with 12 patients within the belinostat cohort of the clinical trial. The median difference between lesion volumes from Cho/NAA $\geq$ 2x and T1w-CE was 16.1 cc. Each subgroup had a total of 6 patients with two patients with MGMT hypermethylation status. The High-Mismatch Group had much larger

differences between Cho/NAA ≥ 2x and T1w-CE, and therefore sMRI suggested there was more undertreated tumor during radiation treatment. The average pre-RT T1w-CE tumor volume post-resection for the High-Mismatch Group was 12.1 ± 4.5 cc and 10.1 ± 4.6 cc for the Low-Mismatch Group. While the T1w-CE tumor volumes were similar, the average pre-RT Cho/NAA ≥ 2X for the High-Mismatch Group was 49.9 ± 11.8 cc and 18.0 ± 8.1 cc for the Low-Mismatch Group ($p < 0.05$). The lack of a linear relationship between T1w-CE and Cho/NAA volumes was further reflected by the r-squared value of 0.05. The mean difference between the Cho/NAA volume and the T1w-CE volume for the High-Mismatch Group was 37.8 ± 16.1 cc and 7.7 ± 3.6 cc for the Low-Mismatch Group ($p < 0.05$). The median OS for the High-Mismatch Group and the Low-Mismatch Group was 14.4 and 34.3 months respectively, with the difference approaching statistical significance ($p = 0.07$). Comparisons of the OS curves for the two cohorts are shown in **Figure 8.4** along with a representative patient elucidating that the difference between T1w-CE volume and the Cho/NAA ≥ 2X volume can almost be two-fold. The Kaplan-Meier curves did not have any cross-over between the two groups.

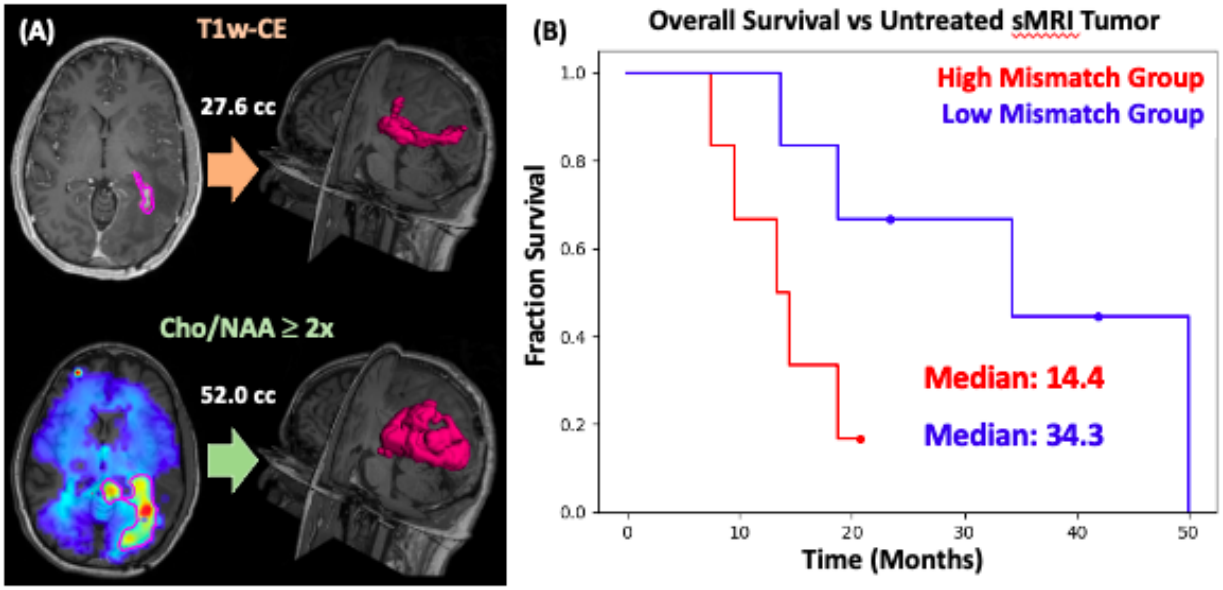

Figure 8.4. (A) A representative patient from the belinostat cohort displaying the vast difference in the T1w-CE derived volume compared to the Cho/NAA ≥ 2x volume. (B) The High-Mismatch Group patients (red) had much larger Cho/NAA ≥ 2x volumes compared to the T1w-CE lesion and showed a median survival of 14.4 months, whereas the counterpart (Low-Mismatch Group) had a smaller difference between Cho/NAA ≥ 2X and the T1w-CE lesion with a median survival of 34.3 months.

Table 8.1 contains GTV2 and CTV2 volumes, rCE volumes at progression and post-progression date 1, and the overlap percentage calculated using GTV2 and CTV2 respectively for the 11 patients in the cohort. The patients' post-progression date 1 scan was typically two to three months after the calculated date of progression. Most patients had post-progression imaging available at least six to eight months after progression providing us with ample data for this analysis. One patient was excluded from the Low-Mismatch Group due to not having sufficient progression scans. The average pre-RT GTV2 for the High-Mismatch Group was 49.2 ± 22.9 cc versus 47.0 ± 9.6 cc for the Low-Mismatch Group ($p = 0.98$). The pre-RT Cho/NAA ≥ 2X volumes for the High-Mismatch

Group was 49.9 ± 11.8 cc and 18.0 ± 8.1 cc for the Low-Mismatch Group ($p < 0.05$). The rCE volumes at the date of progression for the High-Mismatch Group was 21.1 ± 25.5 cc versus 9.8 ± 11.7 cc for the Low-Mismatch Group ($p = 0.42$). We found that on average 17.4% of the rCE volume that was not in the GTV2 area was found within the Cho/NAA ≥ 2X volume. The percentage ranges of rCE excluding the pre-RT GTV2 area but within the pre-RT Cho/NAA ≥ 2X (Overlap % Ex-GTV2) were as large as 53.7% for the High-Mismatch Group and 26.8% for Low-Mismatch Group. When examining the patients at post-progression date 1, we found that the rCE areas had grown to an average of 53.2 ± 33.7 cc for the High-Mismatch Group and 26.9 ± 20.2 cc for the Low-Mismatch Group. However, it was noted that average percentage of rCE volume not included in the GTV2 area but found within the Cho/NAA ≥ 2X was lower at 10.9%.

Table 8.1. Recurrence Analysis Results.

						Progression Date			Post-Progression Date 1		
Subject	**Mismatch Group**	**OS***	**GTV2 (cc)**	**CTV2 (cc)**	**Cho/NAA≥2x (cc)**	**rCE (cc)**	**Overlap Ex-GTV2 (%)**	**Overlap Ex-CTV2 (%)**	**rCE (cc)**	**Overlap Ex-GTV2 (%)**	**Overlap Ex-CTV2 (%)**
EM016	High	18.5	80.7	142.6	55.8	23.7	**32.7**	**5.2**	69.2	**13.1**	**2.2**
EM017	High	7.4	22.0	50.4	42.2	0.3	**0.0**	**0.0**	32.7	**18.6**	**2.7**
EM023	High	20.5	39.2	79.2	31.6	0.1	**0.0**	**0.0**	4.6	**8.9**	**9.2**
EM025	High	9.4	65.7	144.2	62.8	19.0	**53.7**	**13.8**	28.9	**8.2**	**0.0**
JH002	High	13.1	28.8	130.9	21.7	69.2	**0.0**	**0.0**	102.3	**2.3**	**5.8**
JH003	High	14.2	58.9	94.4	61.9	14.2	**26.0**	**27.0**	81.5	**16.5**	**17.8**
EM014	Low	49.3	37.9	71.8	14.5	0.8	**21.5**	**6.1**	3.5	**12.7**	**5.0**
EM015	Low	18.5	59.8	121.8	30.1	4.1	**26.8**	**12.4**	57.4	**22.1**	**9.0**
EM021	Low	13.4	43.9	87.6	19.7	28.6	**26.7**	**14.5**	28.6	**7.9**	**0.4**
EM022	Low	23.1	54.1	98.0	13.0	1.6	**0.0**	**0.0**	29.8	**1.6**	**6.7**
EM024	Low	41.4	39.2	86.5	9.3	13.8	**3.6**	**0.0**	15.0	**8.3**	**0.0**

Progression date was calculated by physician during NCT02137759.
Post-progression date 1 is the next available scan following the progression date.
Ex-GTV2: Excluding GTV2.

Ex-CTV2: Excluding CTV2.
*Months after Surgery.

In **Figure 8.5**, an example patient from this analysis is shown using images acquired post-progression date 2 which is about 4 months after the date of recurrence. This analysis was repeated on these later follow-up dates to show the extent of the Cho/NAA ≥ 2X predictive capabilities. At this date, almost 54.5% of the rCE volume is located within the pre-RT Cho/NAA ≥ 2X but excluded from the pre-RT GTV2. The 3D images in **Figure 8.5** depict the substantial size of the recurrence volume (yellow) that was not within the GTV2 but is enveloped by the sMRI-derived contour (green).

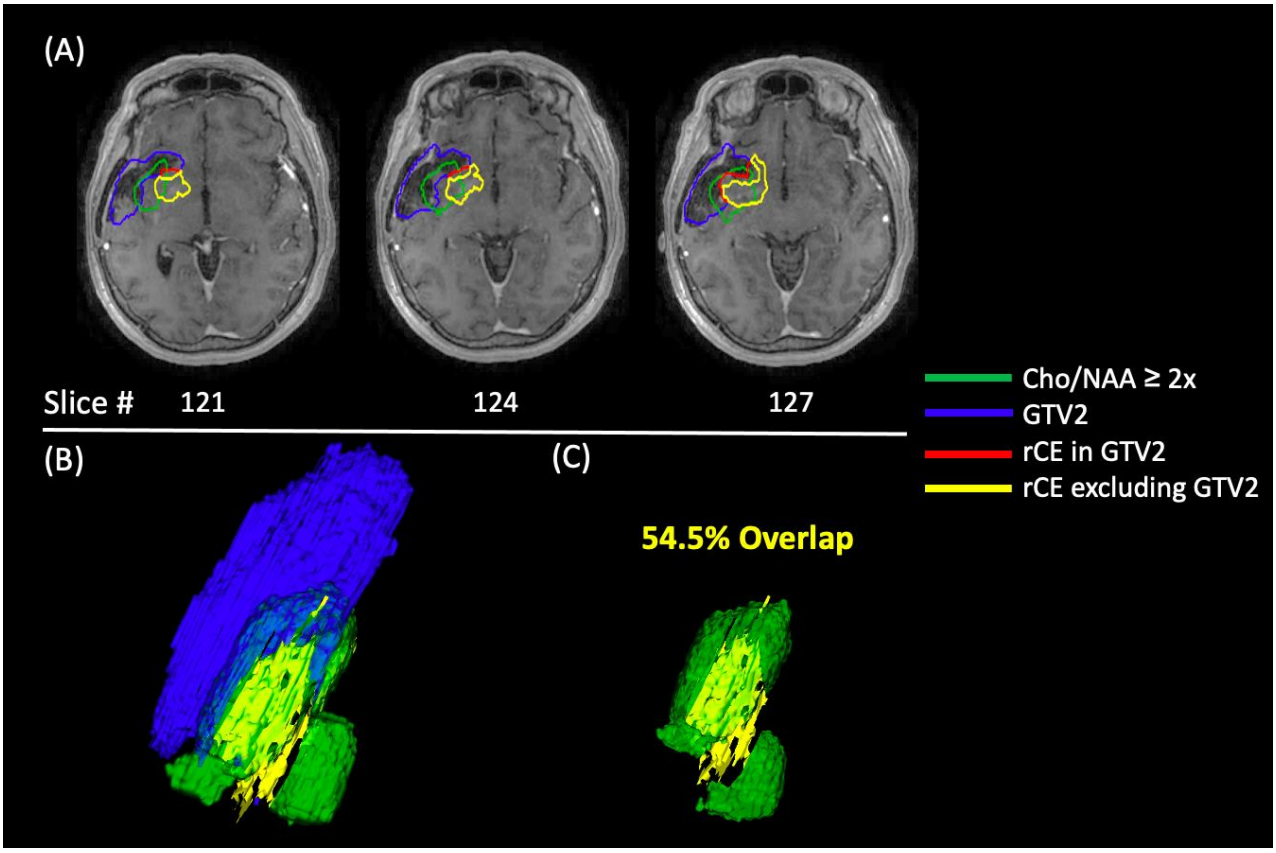

Figure 8.5. A representative case from the High-Mismatch Group with recurrence overlap analysis using GTV2. (A) An axial view of the GTV2 (blue), pre-RT Cho/NAA ≥ 2X, and rCE excluded from GTV2 (yellow) and rCE within the GTV2 (red) These images were acquired 3 months after the progression date calculated using BT-RADS and clinical correlations. (B) 3D images of the rCE volume excluding GTV2 (yellow), the pre-RT Cho/NAA ≥ 2X (green), and the GTV2 (blue). (C) 3D images of the rCE excluded from

GTV2 (yellow) and pre-RT Cho/NAA ≥ 2X (green) without the GTV2 displaying the 54.5% overlap between the two volumes.

When performing the same analysis utilizing CTV2 areas at the date of progression, we found that on average 7.2% of the rCE volume was not located in the CTV2 but found in the Cho/NAA ≥ 2X volume. The average Cho/NAA ≥ 2X volume and rCE volumes remained the same as mentioned above for this analysis. The average CTV2 volume for the High-Mismatch Group was 107 ± 38.4 cc and 93.1 ± 18.5 cc for the Low-Mismatch Group ($p = 0.56$). A similar trend was observed in the post-progression date where the percentage overlap between rCE volume and Cho/NAA≥2X dropped to 5.3%.

Figure 8.6 depicts the same patient with the same date shown in **Figure 8.5**, except with the CTV2 area being shown. At this post-progression date, the rCE volume a 24.8% overlap with the pre-RT Cho/NAA ≥ 2X compared to the original CTV2, despite the large margin added with treatment volumes. As with **Figure 8.5**, the 3D images depict the substantial size of the recurrence volume (yellow) that was not within the CTV2 but is enveloped by the sMRI-derived contour (green).

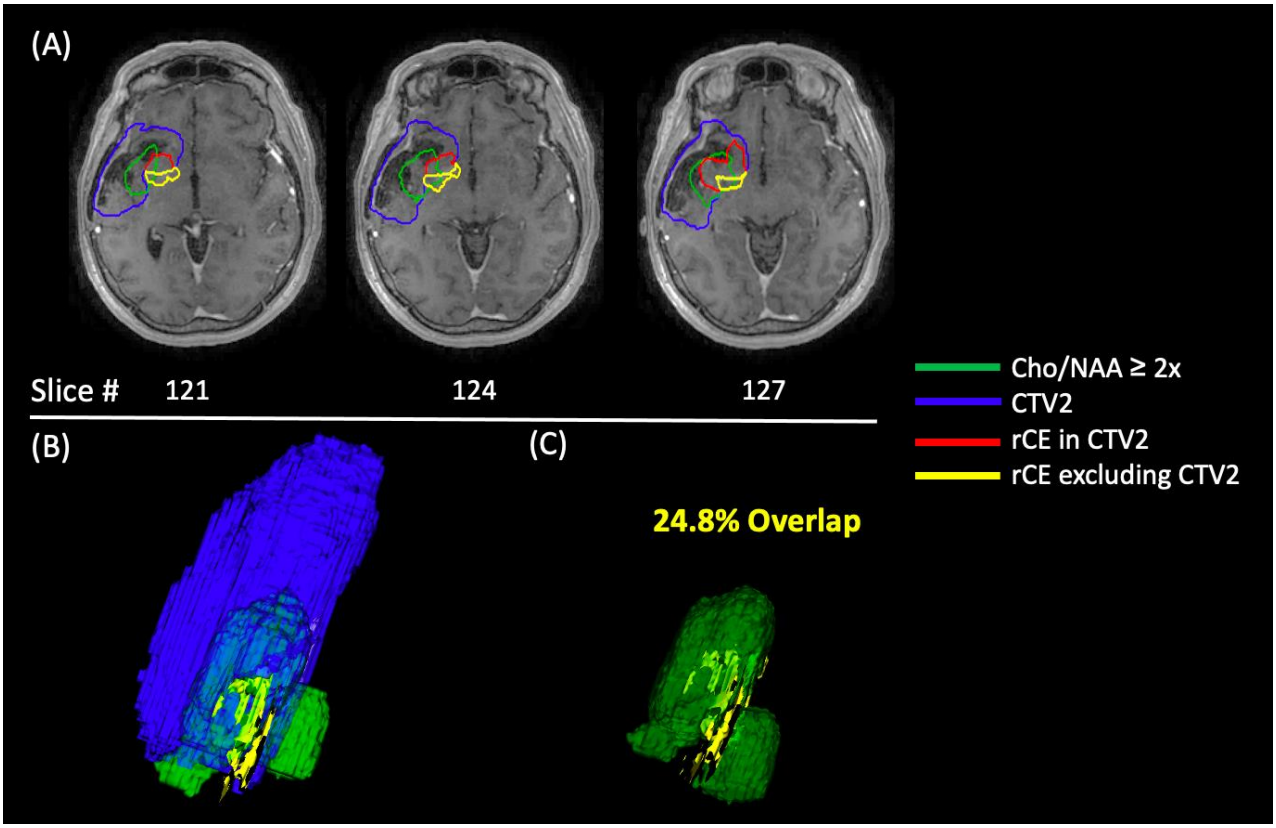

Figure 8.6. A representative case from the High-Mismatch Group with recurrence overlap analysis using CTV2. This is the same patient displayed in Figure 5. (A) An axial view of the CTV2 (blue), pre-RT Cho/NAA ≥ 2X, and rCE excluded from CTV2 (yellow) and rCE within the CTV2 (red). Similar to Figure 5, these images were acquired 3 months after the progression date calculated using BT-RADS and clinical correlations. (B) 3D images of the rCE volume excluding CTV2 (yellow), the pre-RT Cho/NAA ≥ 2X (green), and the CTV2 (blue). (C) 3D images of the rCE excluded from CTV2 (yellow) and pre-RT Cho/NAA ≥ 2X (green) without the CTV2 displaying the 24.8% overlap between the two volumes.

8.4 DISCUSSION

In this report, we present evidence of the clinical value of sMRI in glioma diagnostics and therapeutics by reporting the utility of sMRI in challenging stereotactic biopsies, highlighting the relationship between undertreated sMRI volumes and OS, and emphasizing its role as a recurrence predictor using our unique overlap analysis. In many

of our typical cases, pre-operative diagnostics for stereotactic biopsy are initially completed with standard MRI, which include T1w-CE and T2w/FLAIR scans among other sequences. Low-grade gliomas can be non-enhancing which renders T1w-CE images ineffective, and T2w/FLAIR images may have limited utility due to the large area of hyperintensity which cannot delineate high tumor density, from regions of edema, inflammation, or prior treatment. The diagnostic yield of stereotactic biopsy and the accuracy of tumor grading relies heavily on precise biopsy sampling of the areas of highest grade of disease [153]. A study conducted at the University of Texas MD Anderson Cancer Center found that stereotactic biopsies guided by pre-operative standard MRI can be inaccurate compared to surgical samples. Up to 49% of patients received a different diagnosis when pathologists were only provided the biopsies and at least 33% of those patients would have undergone a different treatment pathway based on this result alone [153,154]. In contrast to the standard MRI scans, our sMRI images were able to distinguish a specific region within the large T2w/FLAIR hyperintensity with more metabolically cancerous tissue [13]. As a result of this sMRI-targeted biopsy, the patient's diagnosis was reclassified from WHO grade II IDH-mutant to WHO grade III IDH-mutant astrocytoma. This would result in recommending a treatment course of concurrent RT with TMZ based on the CATNON trial [155]. If this patient was unable to receive sMRI-guided biopsy, the probability of inadvertently targeting a low tumor density region based on T2w/FLAIR imaging would have been much higher. Ultimately, this could have misguided the patient's treatment course leading to adverse outcomes. This case shows the importance of utilizing accurate and specific imaging biomarkers to guide diagnostic stereotactic biopsies.

Here, we used data from a completed clinical trial to conduct a retrospective analysis exploring whether there is a correlation between undertreated tumors identified through sMRI and OS. Our study group included patients treated with standard-of-care therapy alongside belinostat. We found that patients who had lower volumes of undertreated tumor detected by sMRI had better survival outcomes. Figure 8.4 clearly shows that for the cohort of 12 GBM patients who received belinostat concurrently with chemoradiation, patients with vastly larger Cho/NAA $\geq$ 2x volumes than T1w-CE residual tumor volumes had much poorer survival outcomes. Furthermore, the correlation between the T1w-CE volume and Cho/NAA $\geq$ 2X volume was low (R^2 = 0.05) which exemplifies the lack of relationship between the two volumes and suggests that the tumor area cannot be inferred from T1w-CE abnormality alone. The dissonance between T1w-CE and sMRI volumes demonstrates the importance of utilizing additional metabolic information to guide RT. While the difference in survival was not statistically significant, most likely due to the small sample size, the difference of 20 months between the median OS of the two groups is clinically significant. We hypothesize that if sMRI-guided RT was integrated with belinostat in a larger cohort size, the effects of the treatment would be more apparent in both OS and PFS. The large gap between the Kaplan-Meier curves suggests that treating volumes that largely include sMRI abnormality improves OS compared to treating T1w-CE volumes alone. This study built upon previous pre-clinical studies demonstrating that belinostat was effective in reducing tumor volume in a rat glioma model in a dose-dependent manner **[131]**. However, the efficacy of HDACi in GBM has been widely debated with a variety of clinical trials assessing other similar agents such as vorinostat and panobinostat **[156]**. The Alliance N0874/ACTC trial, which was evaluating the effectiveness of vorinostat combined with

standard chemoradiation in newly diagnosed GBM patients, failed to meet the primary efficacy endpoint with a median OS at 16.1 months **[157]**. From our study results, we hypothesize that some of the failures of other HDACi may be two-fold with the first being poor blood-brain barrier penetration compared to belinostat and the second being RT field planning that does not sufficiently address potential residual tumor **[128]**. The results of this paper suggest that the lack of OS improvement in the treatment cohort of the NCT02137759 trial examining belinostat may have largely been due to poor RT targeting of standard MRI. Our paper emphasizes the importance of utilizing specific and sensitive imaging biomarkers in GBM to evaluate the potential efficacy of HDACi. Compared to the studies mentioned above, the number of patients in our analysis is much smaller and thus larger cohorts are required to create fairer comparisons.

Our overlap statistics showed that on average 17.4% of recurrence volumes could have been treated had RT been guided by Cho/NAA ≥ 2X rather than standard imaging. When considering CTVs rather than GTVs, we demonstrated similar results showing that on average 7.2% of recurrence volumes were undertreated by standard MRI and would have been treated if guided by sMRI. Figure 6 demonstrates that even when adding a substantial margin to create treatment volumes (blue), abnormal tissue is still missed, leading to future patterns of recurrence. This is significant given the large margins added to create the CTVs. If sMRI volumes are used to guide RT, maximal targeting of tumorous tissue could be ensured. We also noted that the rCE overlap volume with the Cho/NAA ≥ 2X at the progression date was similar to the overlap volume at the post-progression date leading to smaller overlap percentages in the post-progression dates. This result was expected as both the Cho/NAA ≥ 2X as well as the GTV and CTV are static volumes while

the rCE is expected to grow with time. The probability that recurrence would extend closer to the treatment volume is low and thus at the post-progression date, our overlap percentages decrease. Figure 8.5 and Figure 8.6 also show us that metabolite mapping displays tumor infiltration connecting two separate lobules of rCE which is not possible with a uniformly expanded CTV2. Metabolite mapping is critical to better track, treat and prevent tumor recurrence. This paper builds upon previous research published that sMRI is an accurate indicator of tumor volume compared to standard clinical imaging [12,21,131]. However, this analysis could be improved if we were able to acquire follow-up sMRI metabolite maps to track the recurrence of the disease more accurately with time. The volumetric analysis performed in this study is unique and allows for more insight into the efficacy of RT targets. The analysis was limited by a small cohort size and data from only two clinical sites but offers proof-of-concept that could be added to a larger clinical trial.

8.5 CONCLUSION

The complex radiographic presentation of gliomas limits the utility of T1w-CE and T2w/FLAIR imaging potentially leading to misdiagnoses from imaging-guided biopsies and undertreatment during radiation therapy. This study showed the efficacy and clinical translatability of spectroscopic MRI in diagnostic stereotactic biopsies while also demonstrating its use as a predictive biomarker for OS. Our recurrence analysis demonstrated that undertreated tumor volumes undetected in standard imaging, but detected with sMRI, tend to overlap with future recurrence patterns, suggesting the vital need for new tools to guide GBM treatment in the clinic. Further, this analysis shows

promise in sMRI-guided radiation therapy combined with a radiosensitizer like belinostat as well as in accurately delineating targets of stereotactic biopsies.

Chapter 9. Conclusions and Future Work

9.1 MAIN CONTRIBUTIONS

9.1.1 Clinical Translatability of Spectroscopic MRI

MR Spectroscopy has existed in one form or another for almost forty years. Despite decades of work recognizing biomarkers in spectroscopy that could potentially treat brain tumors, our work in this dissertation has made great leaps in bringing this technology to the clinic, and ultimately improving patient survival in the process. The Brain Imaging Collaboration Suite, or BrICS, was a software designed specifically for visualizing sMRI acquisitions and generating surgical and radiation treatment plans for GBM [32,52]. In our multi-institutional clinical trial, clinicians and researchers from three reputed academic hospitals (University of Miami, Emory University, and Johns Hopkins University) successfully used sMRI to generate high-dose RT targets for their patients [21]. In that trial, median patient survival extended to 23 months, which is significantly larger than the 15-16 months seen in standard clinical treatment. Remarkably, despite a higher radiation dose administered in potentially larger amounts of tissue, we saw very few if any patient toxicities or side effects from our sMRI-guided radiation treatment.

By analyzing results from this clinical trial, we were able to prove with statistical significance that patients with lower lesion volumes detected by sMRI had much higher survival than patients with relatively larger sMRI lesions [34]. While this finding may seem obvious at first glance, it is important to emphasize that the size of post-surgical sMRI lesions does not correlate with residual enhancing lesions detected in standard clinical

imaging. This demonstrates the unique added value of sMRI in detecting GBM infiltration compared to what physicians use in the clinic.

Finally, we were able to demonstrate the feasibility of low-TE sMRI when tracking GBM patients treated with Belinostat [22,131]. In these studies, each patient had 3-4 sMRI acquisitions, which included one post-treatment sMRI scan. In these cases, BrICS helped clinicians visualize changes in infiltrating tumor as well as the possible influence of radiation treatment on brain metabolism.

9.1.2 Automated Post-Treatment Tracking of Glioblastoma

While we have made great progress in guiding treatment of GBM using sMRI, we have also helped clinicians in the post-treatment follow-up phase. In the clinic, physicians visually assess longitudinal imaging for changes in lesion size. By developing the Longitudinal Imaging Tracker (BrICS-LIT), we have helped physicians visualize imaging from five different dates simultaneously, as well as overlay radiation dose maps, and the ability to graph changes in lesion volume to help quantitatively assess for tumor recurrence [32,35]. While there are hundreds of deep learning segmentation algorithms for pre-surgical brain tumors, we are the first to train and develop a post-surgical tumor segmentation algorithm that is housed in BrICS-LIT for physicians to use. By leveraging the latest computer vision techniques such as Swin-Transformers and even classical CNNs, we were able to achieve Dice Scores over 0.7 for FLAIR and T1w-CE lesions [33]. By using automated segmentation algorithms, we can not only streamline radiation treatment planning, but we also developed a method for automated disease-state classification during post-treatment follow-up. In this process, we can generate suggestive structured reporting

scores using volumetric lesion information that is an improvement from visual assessment of recurrence used in the clinic. Finally, by generating automated disease-state classifications for a patient purely based on their imaging, we have generated a powerful, expedient tool that can track brain tumor patients and detect early recurrence.

9.2 FUTURE WORK

9.2.1 Spectroscopic MRI to Guide GBM Treatment

Every effort in this dissertation to use sMRI for treatment and tracking involved one MRI sequence called Echo Planar Spectroscopic Imaging (EPSI). The 3D-EPSI sequence we use, and its post-processing software (MIDAS) were developed by the University of Miami with the hope of clinical adoption in the future. While BrICS integrates seamlessly with this sequence, there are other sequences, albeit with their own limitations, that are actively used in research for measuring brain metabolism including single voxel (SVS) Stimulated Echo Acquisition Mode (STEAM) or Point Resolved Spectroscopy (PRESS) and other chemical shift imaging (CSI) sequences [158]. While we would advocate that 3D-EPSI, with its whole brain coverage and high resolution is better suited for the clinic, having a software platform that can integrate with any spectroscopy sequence could help bring MR spectroscopy to the clinic.

Further, the MIDAS post-processing software, while sophisticated and complex, usually requires 6-8 hours of post-processing before BrICS can perform additional processing and visualization. While this has been sufficient in our clinical trials, it is not well suited in clinical environments where physicians typically need to see scan results the same day. In addition, MIDAS uses a software language called IDL (Interactive Data

Language), which requires a license for use. To these ends, we are in the process of re-writing the MIDAS software package in Python, which is open source, and can leverage the latest libraries to leverage the GPU and parallel computing. With "pyMIDAS" as well as a previously published deep learning algorithm for fitting MR spectra known as "NNFIT" [60], we plan to reduce the post-processing time from 6-8 hours to one hour and possibly even faster if we can integrate this software onboard MRI scanners.

Finally, sMRI and our imaging software platform will be used in an upcoming nationwide consortium trial (EAF223) to help physicians distinguish true tumor progression from pseudo-progression during post-treatment patient follow-up, a problem that has confounded physicians for decades with clinical imaging.

9.2.2 Additional Applications of Spectroscopic MRI

While we have focused our efforts on applying sMRI for GBM treatment, there are plenty of other applications of sMRI that have been tested and are actively being researched. For one, sMRI can help delineate grade of brain tumor better than clinical imaging can. If physicians can identify that a patient has a grade III astrocytoma or an oligodendroglioma vs a GBM, their treatment plan would change drastically as well as the patient's likely survival [13]. Previous chapters have mentioned our 3D-EPSI sequence using an echo time (TE) of 50 ms or higher for the main purpose of improving signal-to-noise with respect to the Cho, NAA, and Creatine signals. However, when using the same MR acquisition but acquiring at a shorter TE, other metabolite signals can be detected including, glutamate/glutamine, and myo-inositol, which are key metabolites implicated in

depression. There is currently active research in analyzing any relationship between these metabolites and mental health disorders such as seizures, dementia, and depression.

9.2.3 Automated Approaches for Tumor Segmentation and Longitudinal Tracking

There are hundreds of publications on tumor segmentation and even possibly brain tumor segmentation alone. While there have been great leaps in the past decade in bringing computer vision to healthcare, there have been very limited opportunities for these algorithms to make inroads in the clinic. For one, it is quite common for segmentation algorithms to have poor generalizability to external datasets, possibly due to overtraining and testing on datasets that are not sufficiently diverse. The challenge of building a diverse dataset from multiple institutions throughout the world remains difficult as each institution may acquire their imaging in a unique manner and have their own rules and regulations for releasing even anonymized datasets. Most importantly, even if there are segmentation algorithms that can successfully generalize to clinical data, they are difficult to translate to the clinic. Often, these algorithms require input imaging in a certain format, or need a lot of time to format and process imaging before segmentation or require sophisticated hardware such as the latest GPUs often costing thousands of dollars to sufficiently perform segmentation in a timely manner. Finally, many of these algorithms, while dockerized, sit in git repositories, untouched by physicians or clinical software.

To successfully integrate the latest segmentation algorithms into the clinic, there must be an acknowledgement that these algorithms will not be fully-automated. Likely clinical workflows will involve these algorithms performing initial segmentations to save time and then require clinicians to oversee and edit these initializations to their liking. For

this to occur, segmentation algorithms need to be housed in software such as BrICS that allow for easy visualization and expedient editing. Further, a "one-size-fits-all" algorithm may not be the correct solution for the clinic. My segmentation algorithm failed to differentiate ventricle from resection cavity. To account for several possible edge cases, multiple algorithms may need to work together to validate segmentations for the clinic.

There also may need to be a revaluation of medical segmentation tasks in the big picture. Currently, the Dice overlap statistic is used to determine whether a segmentation task has performed well or not. The Dice score is used to train segmentation algorithms to determine whether there is "sufficient" overlap between predicted segmentations and those generated by a clinician. While Dice certainly has its advantages, it may not capture important differences between segmented contours near the edges for example, which can be more significant for treatment planning. In such situations, other loss functions such as Hausdorff may need to be used along with Dice for segmentation tasks tuned to patient treatment. Further, several segmentation competitions and tasks attempt to improve on previous approaches by incrementally improving the Dice score from for example 0.90 to 0.93. While this quantitatively does suggest an "improvement", it is likely a difference that the human eye would not notice and likely a clinician would not care about. More studies are necessary to determine differences between many clinicians even for segmentation tasks before determining an appropriate goal for deep learning.

Finally, for the task of tumor tracking, I attempted to use percent changes in tumor volume over time to predict patient disease-state. However, this runs into a lot of issues. For one, if a patient has a lesion that's 0.2 cc, and in their next visit, their lesion increases to 0.6 cc, that would be a 200% increase in tumor size. But a 0.4 cc increase could likely

be a rounding error or not be clinically important. To that end, the task of tumor tracking is incredibly challenging as the criteria to determine whether a patient's condition is a cause for concern can change depending on the initial size of the tumor and several other factors, making it difficult to quantitate. Further, many longitudinal patient datasets involve non-constant intervals. For example, patient data could occur at month 1, month 4, month 5, and then month 11. With non-constant intervals, new approaches are required to track and develop algorithms for predicting patient risk and survival outcomes. Classic time-series approaches often depend on constant time intervals as a prior assumption. To successfully incorporate the latest transformer-based, RNN, and other time-series approaches for healthcare data, thousands of patient datasets are required. To that end, as with any deep learning or predictive challenge in healthcare, future work will need to address how to handle disparate and smaller datasets.

9.3 CONCLUSION

Treatment of glioblastoma is complex with poor patient outcomes, and little improvement in treatment in the past decade. Imaging is central for guiding patient treatment and post-treatment tracking. By introducing spectroscopic MRI to detect lesion far beyond what is seen in clinical imaging to guide treatment, we have extended patient survival by almost 50%. Further, by developing automated tumor segmentation algorithms and disease-state classifications, we have also improved post-treatment patient tracking that robustly leverages tumor volume. Finally, with every advancement we have made towards improving patient survival, we have ensured our quantitative techniques can be leveraged by physicians by housing them in software that integrates with clinical

workflows. We hope this work can set the foundation for advancing treatment strategies for glioblastoma.

APPENDIX A

A1. List of Publications

1. Gurbani, SS, Yoon Y, Weinberg BD, Salgado E, Press RH, Cordova JS, **Ramesh K**, Liang Z, Voloschin A, Olson, J., Schreibmann E, Shim, H, Shu HG. (2019) Assessing treatment response of glioblastoma to an HDAC inhibitor belinostat. *Tomography* 5(1) QIN Special Issue, 53-60. PMC6403031

2. **Ramesh K,** Gurbani SS, Mellon EA, Huang V, Goryawala M, Barker PB, Kleinberg L, Shu HG, Shim H, Weinberg BD. (2020) The longitudinal imaging tracker (BrICS-LIT): A cloud platform for monitoring treatment response in glioblastoma patients. *Tomography*. 6(2) 93-100. PMC7289246

3. Zhong J., Huang V., Gurbani S., **Ramesh K**., Cordova J.S., Schreibmann E., Shu H.G., Olson J., Han H., Giuffrida A., Shim H., Weinberg B.D. (2021) 3D whole-brain metabolite imaging to improve characterization of low-to-intermediate grade gliomas. *J. Neuroncology*, 153(2):303-311. PMC8237861

4. **Ramesh K**, Mellon EA, Gurbani SS, Huang V, Goryawala M, Barker PB, Kleinberg L, Zhong J, Schreibmann E, Weinberg BD, Maudsley, AA, **Shim H**, Shu HG. (2022) A multisite pilot clinical trial of spectroscopic MRI-guided radiation dose escalation in glioblastoma patients: Interim results and toxicity reports. *Neuro-Oncology Advances*. PMC8976280

5. Xu K, **Ramesh K,** Huang V, Gurbani SS, Schreibmann E, Weinberg BD, Sengupta S, Voloschin AD, Holdhoff M, Barker PB, Kleinberg LR, Olson JJ, Shu HG, Shim H. (2022) Final report on clinical outcomes and tumor recurrence patterns of a human pilot study assessing efficacy of belinostat (PXD-101) combined with chemoradiation in treating newly diagnosed glioblastoma. *Tomography*. PMC8938806

6. **Ramesh, K. K.**, Huang, V., Rosenthal, J., Mellon, E. A., Goryawala, M., Barker, P. B., Gurbani, S. S., Trivedi, A. G., Giuffrida, A. S., Schreibmann, E., Han, H., de le Fuente, M., Dunbar, E. M., Holdhoff, M., Kleinberg, L. R., Shu, H. G., Shim, H., & Weinberg, B. D. (2023). A Novel Approach to Determining Tumor Progression Using a Three-Site Pilot Clinical Trial of Spectroscopic MRI-Guided Radiation Dose Escalation in Glioblastoma. *Tomography*. PMC8938806

7. Huang, V., Rejimon, A., Reddy, K., Trivedi, A. G., **Ramesh, K. K.**, Giuffrida, A. S., Muiruri, R., Shim, H., & Eaton, B. R. (2023). Spectroscopic MRI-Guided Proton Therapy in Non-Enhancing Pediatric High-Grade Glioma. *Tomography*. PMC10037577

8. Chang, C. M., **Ramesh, K. K.**, Huang, V., Gurbani, S., Kleinberg, L. R., Weinberg, B. D., Shim, H., & Shu, H. G. (2023). Mutant Isocitrate Dehydrogenase 1 Expression

Enhances Response of Gliomas to the Histone Deacetylase Inhibitor Belinostat. *Tomography*. PMC10204413

9. Trivedi, A. G., Kim, S. H., **Ramesh, K. K.**, Giuffrida, A. S., Weinberg, B. D., Mellon, E. A., Kleinberg, L. R., Barker, P. B., Han, H., Shu, H. G., Shim, H., & Schreibmann, E. (2023). Applying a Radiation Therapy Volume Analysis Pipeline to Determine the Utility of Spectroscopic MRI-Guided Adaptive Radiation Therapy for Glioblastoma. *Tomography*. PMC10204497

10. Trivedi, A. G., **Ramesh, K. K.**, Huang, V., Mellon, E. A., Barker, P. B., Kleinberg, L. R., Weinberg, B. D., Shu, H. G., & Shim, H. (2023). Spectroscopic MRI-Based Biomarkers Predict Survival for Newly Diagnosed Glioblastoma in a Clinical Trial. *Cancers*. PMC10340675

11. **Ramesh, K. K.**, Xu, K. M., Trivedi, A. G., Huang, V., Sharghi, V. K., Kleinberg, L. R., Mellon, E. A., Shu, H. G., Shim, H., & Weinberg, B. D. (2023). A Fully Automated Post-Surgical Brain Tumor Segmentation Model for Radiation Treatment Planning and Longitudinal Tracking. *Cancers*. PMC10417353

A2. List of Abstracts

1. **Ramesh K**, Gurbani SS, Giuffrida A, Schreibmann E, Shu HG, Shim H, Weinberg BD. The longitudinal imaging tracker (BrICS-LIT): A cloud platform for longitudinal follow-up for patients with glioblastoma. AACR-SNO Meeting, Atlanta, GA, April, 2019. (Oral)

2. Gurbani S, **Ramesh, K**., Shim, H, Weinberg B A cloud platform for longitudinal follow-up for patients with glioblastoma. International Society of Magnetic Resonance in Medicine (ISMRM). Montreal, Canada, May 2019 (Oral)

3. Weinberg B, **Ramesh K,** Gurbani S, Schreibmann E, Kleinberg L, Shu H, Shim H. Brain tumor reporting and data system (BT-RADS) and its assistive tools. SNO Annual Meeting. Phoenix, AZ, November 2019. (Poster)

4. Mellon E, Gurbani S, **Ramesh K**, Weinberg B, Kleinberg L, Schreibmann E, Barker P, Maudsley A, Shim H, Shu H. A Multisite Clinical Trial of Spectroscopic MRI-guide Radiation Dose Escalation in Glioblastoma Patients. SNO Annual Meeting. Phoenix, AZ, November 2019. (Oral)

5. Olson J, Weinberg B, Gurbani S, **Ramesh K**, Schreibmann E, Shu H, Shim H. Spectroscopic MRI to guide biopsy of lower grade gliomas. SNO Annual Meeting. Phoenix, AZ, November 2019 (Poster)

6. Shu H, Gurbani S, **Ramesh K**, Weinberg B, Voloschin A, Olson J, Shim H (2019) Remarkable response of a patient with secondary GBM to a histone deacetylase inhibitor. Society of Neuro-Oncology Annual Meeting. Nov 2019, Phoenix, AZ

7. Schreibmann E, **Ramesh K**, Shu H, Shim H. High resolution spectroscopic MRI and scripting: Toward automated planning for a multi-center clinical trial. AAPM. Virtual Meeting, July 2020. (Oral)

8. Xu K, Huang V, **Ramesh K**, Gurbani S, Schreibmann E, Weinberg BD, Sengupta S, Voloschin AD, Holdhoff M, Barker PB, Kleinberg L, Olson J, Shim H, Shu, HG. Updates on clinical outcomes and tumor recurrence patterns of a human pilot study assessing efficacy of belinostat combining with chemoradiation in treating glioblastoma. SNO Annual Meeting, Virtual, November, 2020. (Poster)

9. Shu H, Gurbani S, **Ramesh K**, Weinberg B, Mellon E. Kleinberg L, Schreibmann E, Barker P, Maudsley A, Shim H. A Multisite Clinical Trial of Spectroscopic MRI-guide Radiation Dose Escalation in Glioblastoma Patients. American Society of Clinical Oncology (ASCO) Annual Meeting. Virtual Meeting, May 2021 (Poster)

10. Shu H, Xu K, Huang V, **Ramesh K**, Gurbani S, Schreibmann E, Weinberg BD,

Sengupta S, Voloschin AD, Holdhoff M, Barker PB, Kleinberg L, Olson J, Shim H. Pilot study utilizing HDAC inhibitor belinostat with chemoradiation for newly-diagnosed glioblastoma. Society of Neuro-Oncology CNS Clinical Trial Virtual Meeting, October 2021 (Oral)

11. Trivedi A, **Ramesh K**, Vicki H, Mellon E, Goryawala M, Kleinberg L, Shu H, Shim H, Weinberg B. Imaging biomarkers for predicting overall and progression-free survival of newly diagnosed GBM in a clinical trial. Radiological Society of North America (RSNA) Annual Meeting, November 2022 (Oral)

12. Trivedi A, Kim S-H, **Ramesh K**, Giuffrida A, Shu H, Mellon E, Kleinberg L, Weinberg B, Schreibmann E, Shim H. Automated analysis pipeline using longitudinal spectroscopic MRI data to assess therapy response in GBM patients. Radiological Society of North America (RSNA) Annual Meeting, November 2023 (Oral)

13. **Ramesh K**, Vicki H, Gurbani S, Kleinberg L, Weinberg B, Shu H, Shim H. Imaging Biomarkers for Predicting Overall Survival of Newly Diagnosed Glioblastoma Treated with Belinostat and Standard of Care. Radiological Society of North America (RSNA) Annual Meeting, November 2023 (Oral)

14. **Ramesh K**, Xu K, Trivedi A, Schreibmann E, Shu H, Shim H, Weinberg B. A Lightweight 3D Segmentation Tool for Radiation Treatment Planning for Glioblastoma. Radiological Society of North America (RSNA) Annual Meeting, November 2023 (Oral)

REFERENCESREFERENCES

1. Thakkar, J.P.; Dolecek, T.A.; Horbinski, C.; Ostrom, Q.T.; Lightner, D.D.; Barnholtz-Sloan, J.S.; Villano, J.L. Epidemiologic and molecular prognostic review of glioblastoma. *Cancer epidemiology, biomarkers & prevention : a publication of the American Association for Cancer Research, cosponsored by the American Society of Preventive Oncology* **2014**, *23*, 1985-1996, doi:10.1158/1055-9965.Epi-14-0275.

2. Krex, D.; Klink, B.; Hartmann, C.; von Deimling, A.; Pietsch, T.; Simon, M.; Sabel, M.; Steinbach, J.P.; Heese, O.; Reifenberger, G.; et al. Long-term survival with glioblastoma multiforme. *Brain : a journal of neurology* **2007**, *130*, 2596-2606, doi:10.1093/brain/awm204.

3. Ostrom, Q.T.; Cioffi, G.; Gittleman, H.; Patil, N.; Waite, K.; Kruchko, C.; Barnholtz-Sloan, J.S. CBTRUS Statistical Report: Primary Brain and Other Central Nervous System Tumors Diagnosed in the United States in 2012–2016. *Neuro-Oncology* **2019**, *21*, v1-v100, doi:10.1093/neuonc/noz150 %J Neuro-Oncology.

4. Gilbert, M.R.; Dignam, J.; Won, M.; Blumenthal, D.T.; Vogelbaum, M.A.; Aldape, K.D.; Colman, H.; Chakravarti, A.; Jeraj, R.; Armstrong, T.S.; et al. RTOG 0825: Phase III double-blind placebo-controlled trial evaluating bevacizumab (Bev) in patients (Pts) with newly diagnosed glioblastoma (GBM). **2013**, *31*, 1-1, doi:10.1200/jco.2013.31.18_suppl.1.

5. Gilbert, M.R.; Wang, M.; Aldape, K.D.; Stupp, R.; Hegi, M.; Jaeckle, K.A.; Armstrong, T.S.; Wefel, J.S.; Won, M.; Blumenthal, D.T.; et al. RTOG 0525: A randomized phase III trial comparing standard adjuvant temozolomide (TMZ) with a dose-dense (dd) schedule in newly diagnosed glioblastoma (GBM). **2011**, *29*, 2006-2006, doi:10.1200/jco.2011.29.15_suppl.2006.

6. Stupp, R.; Taillibert, S.; Kanner, A.; Read, W.; Steinberg, D.M.; Lhermitte, B.; Toms, S.; Idbaih, A.; Ahluwalia, M.S.; Fink, K.; et al. Effect of Tumor-Treating Fields Plus Maintenance Temozolomide vs Maintenance Temozolomide Alone on Survival in Patients With Glioblastoma. *JAMA* **2017**, *318*, 2306, doi:10.1001/jama.2017.18718.

7. Ling, C.; Pouget, C.; Rech, F.; Pflaum, R.; Treffel, M.; Bielle, F.; Mokhtari, K.; Casse, J.-M.; Vignaud, J.-M.; Kalamarides, M.; et al. Endothelial Cell Hypertrophy and Microvascular Proliferation in Meningiomas Are Correlated with Higher Histological Grade and Shorter Progression-Free Survival. *Journal of Neuropathology & Experimental Neurology* **2016**, *75*, 1160-1170, doi:10.1093/jnen/nlw095 %J Journal of Neuropathology & Experimental Neurology.

8. McCullough, B.J.; Ader, V.; Aguedan, B.; Feng, X.; Susanto, D.; Benkers, T.L.; Henson, J.W.; Mayberg, M.; Cobbs, C.S.; Gwinn, R.P.; et al. Preoperative relative cerebral blood volume analysis in gliomas predicts survival and mitigates risk of biopsy sampling error. *Journal of neuro-oncology* **2018**, *136*, 181-188, doi:10.1007/s11060-017-2642-2.

9. Verdugo, E.; Puerto, I.; Medina, M. An update on the molecular biology of glioblastoma, with clinical implications and progress in its treatment. *Cancer communications (London, England)* **2022**, *42*, 1083-1111, doi:10.1002/cac2.12361.

10. Stupp, R.; Mason, W.P.; Van Den Bent, M.J.; Weller, M.; Fisher, B.; Taphoorn, M.J.B.; Belanger, K.; Brandes, A.A.; Marosi, C.; Bogdahn, U.; et al. Radiotherapy plus Concomitant and Adjuvant Temozolomide for Glioblastoma. *New England Journal of Medicine* **2005**, *352*, 987-996, doi:10.1056/nejmoa043330.

11. Noch, E.; Khalili, K. Molecular mechanisms of necrosis in glioblastoma: the role of glutamate excitotoxicity. *Cancer biology & therapy* **2009**, *8*, 1791-1797, doi:10.4161/cbt.8.19.9762.

12. Cordova, J.S.; Shu, H.K.; Liang, Z.; Gurbani, S.S.; Cooper, L.A.; Holder, C.A.; Olson, J.J.; Kairdolf, B.; Schreibmann, E.; Neill, S.G.; et al. Whole-brain spectroscopic MRI biomarkers identify infiltrating margins in glioblastoma patients. *Neuro Oncol* **2016**, *18*, 1180-1189, doi:10.1093/neuonc/now036.

13. Zhong, J.; Huang, V.; Gurbani, S.S.; Ramesh, K.; Scott Cordova, J.; Schreibmann, E.; Shu, H.G.; Olson, J.; Han, H.; Giuffrida, A.; et al. 3D whole-brain metabolite imaging to improve characterization of low-to-intermediate grade gliomas. *Journal of neuro-oncology* **2021**, *153*, 303-311, doi:10.1007/s11060-021-03770-2.

14. Kelly, P.J.; Daumas-Duport, C.; Kispert, D.B.; Kall, B.A.; Scheithauer, B.W.; Illig, J.J. Imaging-based stereotaxic serial biopsies in untreated intracranial glial neoplasms. *Journal of neurosurgery* **1987**, *66*, 865-874, doi:10.3171/jns.1987.66.6.0865.

15. Tsuchiya, K.; Mizutani, Y.; Hachiya, J. Preliminary evaluation of fluid-attenuated inversion-recovery MR in the diagnosis of intracranial tumors. *AJNR. American journal of neuroradiology* **1996**, *17*, 1081-1086.

16. Chang, J.; Thakur, S.B.; Huang, W.; Narayana, A. Magnetic resonance spectroscopy imaging (MRSI) and brain functional magnetic resonance imaging (fMRI) for radiotherapy treatment planning of glioma. *Technol Cancer Res Treat* **2008**, *7*, 349-362.

17. Nelson, S.J.; Graves, E.; Pirzkall, A.; Li, X.; Antiniw Chan, A.; Vigneron, D.B.; McKnight, T.R. In vivo molecular imaging for planning radiation therapy of gliomas: an application of 1H MRSI. *Journal of magnetic resonance imaging : JMRI* **2002**, *16*, 464-476, doi:10.1002/jmri.10183.

18. Nelson, S.J.; Vigneron, D.B.; Dillon, W.P. Serial evaluation of patients with brain tumors using volume MRI and 3D 1H MRSI. *NMR Biomed* **1999**, *12*, 123-138.

19. Parra, N.A.; Maudsley, A.A.; Gupta, R.K.; Ishkanian, F.; Huang, K.; Walker, G.R.; Padgett, K.; Roy, B.; Panoff, J.; Markoe, A.; et al. Volumetric Spectroscopic Imaging of Glioblastoma Multiforme Radiation Treatment Volumes. *International Journal of Radiation Oncology*Biology*Physics* **2014**, *90*, 376-384, doi:https://doi.org/10.1016/j.ijrobp.2014.03.049.

20. Pirzkall, A.; Li, X.; Oh, J.; Chang, S.; Berger, M.S.; Larson, D.A.; Verhey, L.J.; Dillon, W.P.; Nelson, S.J. 3D MRSI for resected high-grade gliomas before RT: tumor extent according to metabolic activity in relation to MRI. *International Journal of Radiation Oncology*Biology*Physics* **2004**, *59*, 126-137, doi:https://doi.org/10.1016/j.ijrobp.2003.08.023.

21. Ramesh, K.; Mellon, E.A.; Gurbani, S.S.; Weinberg, B.D.; Schreibmann, E.; Sheriff, S.A.; Goryawala, M.; de le Fuente, M.; Eaton, B.R.; Zhong, J.; et al. A multi-institutional pilot clinical trial of spectroscopic MRI-guided radiation dose escalation for newly diagnosed glioblastoma. *Neuro-Oncology Advances* **2022**, *4*, vdac006, doi:10.1093/noajnl/vdac006.

22. Xu, K.; Ramesh, K.; Huang, V.; Gurbani, S.S.; Cordova, J.S.; Schreibmann, E.; Weinberg, B.D.; Sengupta, S.; Voloschin, A.D.; Holdhoff, M.; et al. Final Report on Clinical Outcomes and Tumor Recurrence Patterns of a Pilot Study Assessing Efficacy of Belinostat (PXD-101) with Chemoradiation for Newly Diagnosed Glioblastoma. *Tomography* **2022**, *8*, 688-700.

23. Abdulla, S.; Saada, J.; Johnson, G.; Jefferies, S.; Ajithkumar, T. Tumour progression or pseudoprogression? A review of post-treatment radiological appearances of glioblastoma. *Clinical Radiology* **2015**, *70*, 1299-1312.

24. Da Cruz, L.H.; Rodriguez, I.; Domingues, R.; Gasparetto, E.; Sorensen, A. Pseudoprogression and pseudoresponse: imaging challenges in the assessment of posttreatment glioma. *American Journal of Neuroradiology* **2011**, *32*, 1978-1985.

25. Cramer, J.A.; Eisenmenger, L.B.; Pierson, N.S.; Dhatt, H.S.; Heilbrun, M.E.J.A.R. Structured and templated reporting: An overview. *Applied Radiology* **2014**, *43*, 18-21.

26. Ganeshan, D.; Duong, P.T.; Probyn, L.; Lenchik, L.; McArthur, T.A.; Retrouvey, M.; Ghobadi, E.H.; Desouches, S.L.; Pastel, D.; Francis, I.R. Structured Reporting in Radiology. *Academic radiology* **2018**, *25*, 66-73, doi:10.1016/j.acra.2017.08.005.

27. D'orsi, C.J. *Illustrated Breast Imaging Reporting and Data System:(illustrated BI-RADS)*; American College of Radiology: 1998.

28. Hong, A.S.; Rosen, E.L.; Soo, M.S.; Baker, J.A. BI-RADS for sonography: positive and negative predictive values of sonographic features. *American Journal of Roentgenology* **2005**, *184*, 1260-1265.

29. Lazarus, E.; Mainiero, M.B.; Schepps, B.; Koelliker, S.L.; Livingston, L.S. BI-RADS lexicon for US and mammography: interobserver variability and positive predictive value. *Radiology* **2006**, *239*, 385-391.

30. Gore, A.; Hoch, M.J.; Shu, H.G.; Olson, J.J.; Voloschin, A.D.; Weinberg, B.D. Institutional Implementation of a Structured Reporting System: Our Experience with the Brain Tumor Reporting and Data System. *Academic radiology* **2019**, *26*, 974-980, doi:10.1016/j.acra.2018.12.023.

31. Weinberg, B.; Ramesh, K.; Gurbani, S.; Schreibmann, E.; Kleinberg, L.; Shu, H.-K.; Shim, H. NIMG-23. BRAIN TUMOR REPORTING AND DATA SYSTEM (BT-RADS) AND QUANTITATIVE TOOLS TO GUIDE ITS IMPLEMENTATION. *Neuro-Oncology* **2019**, *21*, vi166-vi166, doi:10.1093/neuonc/noz175.695 %J Neuro-Oncology.

32. Ramesh, K.; Gurbani, S.S.; Mellon, E.A.; Huang, V.; Goryawala, M.; Barker, P.B.; Kleinberg, L.; Shu, H.G.; Shim, H.; Weinberg, B.D. The Longitudinal Imaging Tracker (BrICS-LIT):A Cloud Platform for Monitoring Treatment Response in Glioblastoma Patients. *Tomography* **2020**, *6*, 93-100, doi:10.18383/j.tom.2020.00001.

33. Ramesh, K.K.; Xu, K.M.; Trivedi, A.G.; Huang, V.; Sharghi, V.K.; Kleinberg, L.R.; Mellon, E.A.; Shu, H.-K.G.; Shim, H.; Weinberg, B.D. A Fully Automated Post-Surgical Brain Tumor Segmentation Model for Radiation Treatment Planning and Longitudinal Tracking. *Cancers* **2023**, *15*, 3956.

34. Trivedi, A.G.; Ramesh, K.K.; Huang, V.; Mellon, E.A.; Barker, P.B.; Kleinberg, L.R.; Weinberg, B.D.; Shu, H.-K.G.; Shim, H. Spectroscopic MRI-Based Biomarkers Predict Survival for Newly Diagnosed Glioblastoma in a Clinical Trial. *Cancers* **2023**, *15*, 3524.

35. Ramesh, K.K.; Huang, V.; Rosenthal, J.; Mellon, E.A.; Goryawala, M.; Barker, P.B.; Gurbani, S.S.; Trivedi, A.G.; Giuffrida, A.S.; Schreibmann, E.; et al. A Novel Approach to Determining Tumor Progression Using a Three-Site Pilot Clinical Trial of Spectroscopic MRI-Guided Radiation Dose Escalation in Glioblastoma. *Tomography* **2023**, *9*, 362-374.

36. Rejimon, A.C.; Ramesh, K.K.; Trivedi, A.G.; Huang, V.; Schreibmann, E.; Weinberg, B.D.; Kleinberg, L.R.; Shu, H.-K.G.; Shim, H.; Olson, J.J. The Utility of Spectroscopic MRI in Stereotactic Biopsy and Radiotherapy Guidance in Newly Diagnosed Glioblastoma. **2024**, *10*, 428-443.

37. Ostrom, Q.T.; Gittleman, H.; Farah, P.; Ondracek, A.; Chen, Y.; Wolinsky, Y.; Stroup, N.E.; Kruchko, C.; Barnholtz-Sloan, J.S. CBTRUS statistical report:

Primary brain and central nervous system tumors diagnosed in the United States in 2006-2010. *Neuro Oncol* **2013**, *15 Suppl 2*, ii1-56, doi:10.1093/neuonc/not151.

38. Gilbert, M.R.; Dignam, J.J.; Armstrong, T.S.; Wefel, J.S.; Blumenthal, D.T.; Vogelbaum, M.A.; Colman, H.; Chakravarti, A.; Pugh, S.; Won, M.; et al. A Randomized Trial of Bevacizumab for Newly Diagnosed Glioblastoma. **2014**, *370*, 699-708, doi:10.1056/NEJMoa1308573.

39. Gilbert, M.R.; Wang, M.; Aldape, K.D.; Stupp, R.; Hegi, M.E.; Jaeckle, K.A.; Armstrong, T.S.; Wefel, J.S.; Won, M.; Blumenthal, D.T.; et al. Dose-dense temozolomide for newly diagnosed glioblastoma: a randomized phase III clinical trial. *J Clin Oncol* **2013**, *31*, 4085-4091, doi:10.1200/JCO.2013.49.6968.

40. Stupp, R.; Hegi, M.E.; Mason, W.P.; van den Bent, M.J.; Taphoorn, M.J.; Janzer, R.C.; Ludwin, S.K.; Allgeier, A.; Fisher, B.; Belanger, K.; et al. Effects of radiotherapy with concomitant and adjuvant temozolomide versus radiotherapy alone on survival in glioblastoma in a randomised phase III study: 5-year analysis of the EORTC-NCIC trial. *Lancet Oncol* **2009**, *10*, 459-466.

41. Wernicke, A.G.; Smith, A.W.; Taube, S.; Mehta, M.P. Glioblastoma: Radiation treatment margins, how small is large enough? *Practical radiation oncology* **2016**, *6*, 298-305, doi:10.1016/j.prro.2015.12.002.

42. Gondi, V.; Pugh, S.; Tsien, C.; Chenevert, T.; Gilbert, M.; Omuro, A.; Mcdonough, J.; Aldape, K.; Srinivasan, A.; Rogers, C. Radiotherapy (RT) Dose-intensification (DI) Using Intensity-modulated RT (IMRT) versus Standard-dose (SD) RT with Temozolomide (TMZ) in Newly Diagnosed Glioblastoma (GBM): Preliminary Results of NRG Oncology BN001. *International Journal of Radiation Oncology, Biology, Physics* **2020**, *108*, S22-S23.

43. Narayana, A.; Chang, J.; Thakur, S.; Huang, W.; Karimi, S.; Hou, B.; Kowalski, A.; Perera, G.; Holodny, A.; Gutin, P.H. Use of MR spectroscopy and functional imaging in the treatment planning of gliomas. *Br J Radiol* **2007**, *80*, 347-354.

44. Ken, S.; Vieillevigne, L.; Franceries, X.; Simon, L.; Supper, C.; Lotterie, J.A.; Filleron, T.; Lubrano, V.; Berry, I.; Cassol, E.; et al. Integration method of 3D MR spectroscopy into treatment planning system for glioblastoma IMRT dose painting with integrated simultaneous boost. *Radiat Oncol* **2013**, *8*, 1, doi:10.1186/1748-717X-8-1.

45. Laprie, A.; Ken, S.; Filleron, T.; Lubrano, V.; Vieillevigne, L.; Tensaouti, F.; Catalaa, I.; Boetto, S.; Khalifa, J.; Attal, J.; et al. Dose-painting multicenter phase III trial in newly diagnosed glioblastoma: the SPECTRO-GLIO trial comparing arm A standard radiochemotherapy to arm B radiochemotherapy with simultaneous integrated boost guided by MR spectroscopic imaging. *BMC Cancer* **2019**, *19*, 167, doi:10.1186/s12885-019-5317-x.

46. Schag, C.C.; Heinrich, R.L.; Ganz, P.A. Karnofsky performance status revisited: reliability, validity, and guidelines. *Journal of Clinical Oncology* **1984**, *2*, 187-193.

47. Goryawala, M.; Saraf-Lavi, E.; Nagornaya, N.; Heros, D.; Komotar, R.; Maudsley, A.A. The Association between Whole-Brain MR Spectroscopy and IDH Mutation Status in Gliomas. *Journal of Neuroimaging* **2020**, *30*, 58-64, doi:10.1111/jon.12685.

48. Goryawala, M.Z.; Sheriff, S.; Maudsley, A.A. Regional distributions of brain glutamate and glutamine in normal subjects. *NMR Biomed* **2016**, *29*, 1108-1116, doi:10.1002/nbm.3575.

49. Goryawala, M.Z.; Sheriff, S.; Stoyanova, R.; Maudsley, A.A. Spectral decomposition for resolving partial volume effects in MRSI. *Magn Reson Med* **2018**, *79*, 2886-2895, doi:10.1002/mrm.26991.

50. Sabati, M.; Sheriff, S.; Gu, M.; Wei, J.; Zhu, H.; Barker, P.B.; Spielman, D.M.; Alger, J.R.; Maudsley, A.A. Multivendor implementation and comparison of volumetric whole-brain echo-planar MR spectroscopic imaging. *Magn Reson Med* **2015**, *74*, 1209-1220, doi:10.1002/mrm.25510.

51. Maudsley, A.A.; Darkazanli, A.; Alger, J.R.; Hall, L.O.; Schuff, N.; Studholme, C.; Yu, Y.; Ebel, A.; Frew, A.; Goldgof, D.; et al. Comprehensive processing, display and analysis for in vivo MR spectroscopic imaging. *NMR Biomed* **2006**, *19*, 492-503.

52. Gurbani, S.; Weinberg, B.; Cooper, L.; Mellon, E.; Schreibmann, E.; Sheriff, S.; Maudsley, A.; Goryawala, M.; Shu, H.K.; Shim, H. The Brain Imaging Collaboration Suite (BrICS): A Cloud Platform for Integrating Whole-Brain Spectroscopic MRI into the Radiation Therapy Planning Workflow. *Tomography* **2019**, *5*, 184-191, doi:10.18383/j.tom.2018.00028.

53. Weinberg, B.D.; Gore, A.; Shu, H.G.; Olson, J.J.; Duszak, R.; Voloschin, A.D.; Hoch, M.J. Management-Based Structured Reporting of Posttreatment Glioma Response With the Brain Tumor Reporting and Data System. *Journal of the American College of Radiology : JACR* **2018**, *15*, 767-771, doi:10.1016/j.jacr.2018.01.022.

54. Bland, J.M.; Altman, D.G. Statistics Notes: Survival probabilities (the Kaplan-Meier method). *BMJ* **1998**, *317*, 1572-1580, doi:10.1136/bmj.317.7172.1572.

55. Davidson-Pilon, C. Lifelines: survival analysis in Python. *Journal of Open Source Software* **2019**, *4*, doi:doi.org/10.21105/joss.01317.

56. Zikou, A.; Sioka, C.; Alexiou, G.A.; Fotopoulos, A.; Voulgaris, S.; Argyropoulou, M.I. Radiation Necrosis, Pseudoprogression, Pseudoresponse, and Tumor Recurrence: Imaging Challenges for the Evaluation of Treated Gliomas. *Contrast media & molecular imaging* **2018**, *2018*, 6828396, doi:10.1155/2018/6828396.

57. Pope, W.B.; Young, J.R.; Ellingson, B.M. Advances in MRI assessment of gliomas and response to anti-VEGF therapy. *Curr Neurol Neurosci Rep* **2011**, *11*, 336-344, doi:10.1007/s11910-011-0179-x.

58. Stupp, R.; Taillibert, S.; Kanner, A.A.; Kesari, S.; Steinberg, D.M.; Toms, S.A.; Taylor, L.P.; Lieberman, F.; Silvani, A.; Fink, K.L.; et al. Maintenance Therapy With Tumor-Treating Fields Plus Temozolomide vs Temozolomide Alone for Glioblastoma: A Randomized Clinical Trial. *JAMA* **2015**, *314*, 2535-2543, doi:10.1001/jama.2015.16669.

59. Louis, D.N.; Perry, A.; Wesseling, P.; Brat, D.J.; Cree, I.A.; Figarella-Branger, D.; Hawkins, C.; Ng, H.; Pfister, S.M.; Reifenberger, G. The 2021 WHO classification of tumors of the central nervous system: a summary. *Neuro-oncology* **2021**, *23*, 1231-1251.

60. Gurbani, S.S.; Schreibmann, E.; Maudsley, A.A.; Cordova, J.S.; Soher, B.J.; Poptani, H.; Verma, G.; Barker, P.B.; Shim, H.; Cooper, L.A.D. A convolutional neural network to filter artifacts in spectroscopic <scp>MRI</scp>. *Magnetic Resonance in Medicine* **2018**, *80*, 1765-1775, doi:10.1002/mrm.27166.

61. Maudsley, A.A.; Domenig, C.; Govind, V.; Darkazanli, A.; Studholme, C.; Arheart, K.; Bloomer, C. Mapping of brain metabolite distributions by volumetric proton MR spectroscopic imaging (MRSI). *Magn Reson Med* **2009**, *61*, 548-559, doi:10.1002/mrm.21875.

62. Veenith, T.V.; Mada, M.; Carter, E.; Grossac, J.; Newcombe, V.; Outtrim, J.; Lupson, V.; Nallapareddy, S.; Williams, G.B.; Sheriff, S.; et al. Comparison of inter subject variability and reproducibility of whole brain proton spectroscopy. *PLoS One* **2014**, *9*, e115304, doi:10.1371/journal.pone.0115304.

63. Zhang, Y.; Taub, E.; Salibi, N.; Uswatte, G.; Maudsley, A.A.; Sheriff, S.; Womble, B.; Mark, V.W.; Knight, D.C. Comparison of reproducibility of single voxel spectroscopy and whole-brain magnetic resonance spectroscopy imaging at 3T. *NMR Biomed* **2018**, *31*, e3898, doi:10.1002/nbm.3898.

64. Cordova, J.S.; Schreibmann, E.; Hadjipanayis, C.G.; Guo, Y.; Shu, H.K.; Shim, H.; Holder, C.A. Quantitative tumor segmentation for evaluation of extent of glioblastoma resection to facilitate multisite clinical trials. *Transl Oncol* **2014**, *7*, 40-47, doi:10.1593/tlo.13835.

65. Chinot, O.L.; Wick, W.; Mason, W.; Henriksson, R.; Saran, F.; Nishikawa, R.; Carpentier, A.F.; Hoang-Xuan, K.; Kavan, P.; Cernea, D.; et al. Bevacizumab plus Radiotherapy–Temozolomide for Newly Diagnosed Glioblastoma. *New England Journal of Medicine* **2014**, *370*, 709-722, doi:10.1056/nejmoa1308345.

66. Grabowski, M.M.; Recinos, P.F.; Nowacki, A.S.; Schroeder, J.L.; Angelov, L.; Barnett, G.H.; Vogelbaum, M.A. Residual tumor volume versus extent of resection:

predictors of survival after surgery for glioblastoma. *Journal of neurosurgery* **2014**, *121*, 1115-1123, doi:10.3171/2014.7.JNS132449.

67. Haj, A.; Doenitz, C.; Schebesch, K.-M.; Ehrensberger, D.; Hau, P.; Putnik, K.; Riemenschneider, M.; Wendl, C.; Gerken, M.; Pukrop, T.; et al. Extent of Resection in Newly Diagnosed Glioblastoma: Impact of a Specialized Neuro-Oncology Care Center. *Brain Sciences* **2017**, *8*, 5, doi:10.3390/brainsci8010005.

68. Awad, A.-W.; Karsy, M.; Sanai, N.; Spetzler, R.; Zhang, Y.; Xu, Y.; Mahan, M.A. Impact of removed tumor volume and location on patient outcome in glioblastoma. *Journal of neuro-oncology* **2017**, *135*, 161-171, doi:10.1007/s11060-017-2562-1.

69. Ostrom, Q.T.; Gittleman, H.; Truitt, G.; Boscia, A.; Kruchko, C.; Barnholtz-Sloan, J.S. CBTRUS statistical report: primary brain and other central nervous system tumors diagnosed in the United States in 2011–2015. *Neuro-oncology* **2018**, *20*, iv1-iv86.

70. Aiken, A.H.; Farley, A.; Baugnon, K.L.; Corey, A.; El-Deiry, M.; Duszak, R.; Beitler, J.; Hudgins, P.A. Implementation of a novel surveillance template for head and neck cancer: Neck Imaging Reporting and Data System (NI-RADS). *Journal of the American College of Radiology* **2016**, *13*, 743-746. e741.

71. Weinreb, J.C.; Barentsz, J.O.; Choyke, P.L.; Cornud, F.; Haider, M.A.; Macura, K.J.; Margolis, D.; Schnall, M.D.; Shtern, F.; Tempany, C.M. PI-RADS prostate imaging–reporting and data system: 2015, version 2. *European Urology* **2016**, *69*, 16-40.

72. Ellingson, B.M.; Bendszus, M.; Boxerman, J.; Barboriak, D.; Erickson, B.J.; Smits, M.; Nelson, S.J.; Gerstner, E.; Alexander, B.; Goldmacher, G. Consensus recommendations for a standardized brain tumor imaging protocol in clinical trials. *Neuro-oncology* **2015**, *17*, 1188-1198.

73. Huang, R.Y.; Wen, P.Y. Response assessment in neuro-oncology criteria and clinical endpoints. *Magnetic Resonance Imaging Clinics* **2016**, *24*, 705-718.

74. James, K.; Eisenhauer, E.; Christian, M.; Terenziani, M.; Vena, D.; Muldal, A.; Therasse, P. Measuring response in solid tumors: unidimensional versus bidimensional measurement. *Journal of the National Cancer Institute* **1999**, *91*, 523-528.

75. Macdonald, D.R.; Cascino, T.L.; Schold, S.C., Jr.; Cairncross, J.G. Response criteria for phase II studies of supratentorial malignant glioma. *J Clin Oncol* **1990**, *8*, 1277-1280, doi:10.1200/JCO.1990.8.7.1277.

76. Quant, E.C.; Wen, P.Y. Response assessment in neuro-oncology. *Current oncology reports* **2011**, *13*, 50-56.

77. Wen, P.Y.; Macdonald, D.R.; Reardon, D.A.; Cloughesy, T.F.; Sorensen, A.G.; Galanis, E.; DeGroot, J.; Wick, W.; Gilbert, M.R.; Lassman, A.B. Updated response assessment criteria for high-grade gliomas: response assessment in neuro-oncology working group. *Journal of clinical oncology* **2010**, *28*, 1963-1972.

78. Zhang, J.Y.; Weinberg, B.D.; Hu, R.; Saindane, A.; Mullins, M.; Allen, J.; Hoch, M.J. Quantitative Improvement in Brain Tumor MRI Through Structured Reporting (BT-RADS). *Academic radiology* **2020**, *27*, 780-784, doi:10.1016/j.acra.2019.07.028.

79. Harris, P.A.; Taylor, R.; Thielke, R.; Payne, J.; Gonzalez, N.; Conde, J.G. Research electronic data capture (REDCap)—a metadata-driven methodology and workflow process for providing translational research informatics support. *Journal of biomedical informatics* **2009**, *42*, 377-381.

80. Gurbani, S.S.; Schreibmann, E.; Sheriff, S.; Cooper, L.A.D.; Shu, H.K.G.; Holder, C.A.; Maudsley, A.A.; Shim, H. A Software Platform for Collaborative Radiation Therapy Planning Using Spectroscopic MRI. *International Journal of Radiation Oncology • Biology • Physics* **2017**, *99*, E667, doi:10.1016/j.ijrobp.2017.06.2209.

81. Yoo, T.S.; Ackerman, M.J.; Lorensen, W.E.; Schroeder, W.; Chalana, V.; Aylward, S.; Metaxas, D.; Whitaker, R. Engineering and algorithm design for an image processing Api: a technical report on ITK--the Insight Toolkit. *Studies in health technology and informatics* **2002**, *85*, 586-592.

82. McCormick, M.; Liu, X.; Jomier, J.; Marion, C.; Ibanez, L. ITK: enabling reproducible research and open science. *Frontiers in neuroinformatics* **2014**, *8*, 13, doi:10.3389/fninf.2014.00013.

83. Johnson, H.; Harris, G.; Williams, K. BRAINSFit: mutual information rigid registrations of whole-brain 3D images, using the insight toolkit. *Insight Journal* **2007**, *57*.

84. Dempsey, M.F.; Condon, B.R.; Hadley, D.M. Measurement of tumor "size" in recurrent malignant glioma: 1D, 2D, or 3D? *American journal of neuroradiology* **2005**, *26*, 770-776.

85. Warr, D.; McKinney, S.; Tannock, I. Influence of measurement error on assessment of response to anticancer chemotherapy: proposal for new criteria of tumor response. *Journal of Clinical Oncology* **1984**, *2*, 1040-1046.

86. Otsu, N. A threshold selection method from gray-level histograms. *IEEE transactions on systems, man, cybernetics*

1979, *9*, 62-66.

87. Bauer, S.; Fejes, T.; Reyes, M. A skull-stripping filter for ITK. *Insight Journal* **2013**, *2012*.

88. Annangi, P.; Krishnan, K.B.; Banerjee, J.; Gupta, M.; Patil, U. Automatic detection and estimation of biparietal diameter from fetal ultrasonography. In Proceedings of the Medical Imaging 2011: Ultrasonic Imaging, Tomography, and Therapy, 2011; p. 79680I.

89. Vincent, L. Morphological area openings and closings for grey-scale images. In *Shape in Picture*; Springer: 1994; pp. 197-208.

90. Sethian, J.A. *Level set methods and fast marching methods: evolving interfaces in computational geometry, fluid mechanics, computer vision, and materials science*; Cambridge university press: 1999; Volume 3.

91. Tan, A.C.; Ashley, D.M.; López, G.Y.; Malinzak, M.; Friedman, H.S.; Khasraw, M. Management of glioblastoma: State of the art and future directions. *CA: a cancer journal for clinicians* **2020**, *70*, 299-312, doi:10.3322/caac.21613.

92. Duijn, J.H.; Matson, G.B.; Maudsley, A.A.; Weiner, M.W. 3D phase encoding 1H spectroscopic imaging of human brain. *Magnetic resonance imaging* **1992**, *10*, 315-319, doi:10.1016/0730-725x(92)90490-q.

93. Horská, A.; Barker, P.B. Imaging of brain tumors: MR spectroscopy and metabolic imaging. *Neuroimaging clinics of North America* **2010**, *20*, 293-310, doi:10.1016/j.nic.2010.04.003.

94. Farche, M.K.; Fachinetti, N.O.; da Silva, L.R.; Matos, L.A.; Appenzeller, S.; Cendes, F.; Reis, F. Revisiting the use of proton magnetic resonance spectroscopy in distinguishing between primary and secondary malignant tumors of the central nervous system. *The Neuroradiology Journal* **2022**, *35*, 619-626.

95. Lawrence, Y.R.; Li, X.A.; el Naqa, I.; Hahn, C.A.; Marks, L.B.; Merchant, T.E.; Dicker, A.P. Radiation dose-volume effects in the brain. *Int J Radiat Oncol Biol Phys* **2010**, *76*, S20-27, doi:10.1016/j.ijrobp.2009.02.091.

96. Fulham, M.J.; Bizzi, A.; Dietz, M.J.; Shih, H.H.; Raman, R.; Sobering, G.S.; Frank, J.A.; Dwyer, A.J.; Alger, J.R.; Di Chiro, G. Mapping of brain tumor metabolites with proton MR spectroscopic imaging: clinical relevance. *Radiology* **1992**, *185*, 675-686.

97. Shu, H., Mellon, EA, Kleinberg, LR, Gurbani, SS, Ramesh, KK, Goryawala, M, Sheriff, SA, Huang, V, Barker, PB, Maudsley, A, Schreibmann, E, Weinberg, BD, Shim, H. A multisite clinical trial of spectroscopic MRI-guided radiation dose escalation for newly-diagnosed glioblastomas. In Proceedings of the American Society of Clinical Oncology Virtual, 2021.

98. Yang, Y.; Yang, Y.; Wu, X.; Pan, Y.; Zhou, D.; Zhang, H.; Chen, Y.; Zhao, J.; Mo, Z.; Huang, B. Adding DSC PWI and DWI to BT-RADS can help identify postoperative recurrence in patients with high-grade gliomas. *Journal of neuro-oncology* **2020**, *146*, 363-371, doi:10.1007/s11060-019-03387-6.

99. Balwant, M.K. A Review on Convolutional Neural Networks for Brain Tumor Segmentation: Methods, Datasets, Libraries, and Future Directions. *IRBM* **2022**, *43*, 521-537, doi:https://doi.org/10.1016/j.irbm.2022.05.002.

100. Ghosh, A.; Thakur, S. Review of Brain Tumor MRI Image Segmentation Methods for BraTS Challenge Dataset. In Proceedings of the 2022 12th International Conference on Cloud Computing, Data Science & Engineering (Confluence), 27-28 Jan. 2022, 2022; pp. 405-410.

101. Tillmanns, N.; Lum, A.E.; Cassinelli, G.; Merkaj, S.; Verma, T.; Zeevi, T.; Staib, L.; Subramanian, H.; Bahar, R.C.; Brim, W.; et al. Identifying clinically applicable machine learning algorithms for glioma segmentation: recent advances and discoveries. *Neuro-Oncology Advances* **2022**, *4*, doi:10.1093/noajnl/vdac093.

102. Wang, F.; Jiang, R.; Zheng, L.; Meng, C.; Biswal, B. 3D U-Net Based Brain Tumor Segmentation and Survival Days Prediction. In Proceedings of the Brainlesion: Glioma, Multiple Sclerosis, Stroke and Traumatic Brain Injuries, Cham, 2020//, 2020; pp. 131-141.

103. Hatamizadeh, A.; Nath, V.; Tang, Y.; Yang, D.; Roth, H.R.; Xu, D. Swin UNETR: Swin Transformers for Semantic Segmentation of Brain Tumors in MRI Images. In Proceedings of the Brainlesion: Glioma, Multiple Sclerosis, Stroke and Traumatic Brain Injuries, Cham, 2022//, 2022; pp. 272-284.

104. Shusharina, N.; Söderberg, J.; Edmunds, D.; Löfman, F.; Shih, H.; Bortfeld, T. Automated delineation of the clinical target volume using anatomically constrained 3D expansion of the gross tumor volume. *Radiotherapy and Oncology* **2020**, *146*, 37-43, doi:https://doi.org/10.1016/j.radonc.2020.01.028.

105. Sadeghi, S.; Farzin, M.; Gholami, S. Fully automated clinical target volume segmentation for glioblastoma radiotherapy using a deep convolutional neural network. *Polish Journal of Radiology* **2023**, *88*, 31-40, doi:10.5114/pjr.2023.124434.

106. Ermiş, E.; Jungo, A.; Poel, R.; Blatti-Moreno, M.; Meier, R.; Knecht, U.; Aebersold, D.M.; Fix, M.K.; Manser, P.; Reyes, M.; et al. Fully automated brain resection cavity delineation for radiation target volume definition in glioblastoma patients using deep learning. *Radiation Oncology* **2020**, *15*, 100, doi:10.1186/s13014-020-01553-z.

107. Chukwueke, U.N.; Wen, P.Y. Use of the Response Assessment in Neuro-Oncology (RANO) criteria in clinical trials and clinical practice. *CNS Oncology* **2019**, *8*, CNS28, doi:10.2217/cns-2018-0007.

108. Kickingereder, P.; Isensee, F.; Tursunova, I.; Petersen, J.; Neuberger, U.; Bonekamp, D.; Brugnara, G.; Schell, M.; Kessler, T.; Foltyn, M.; et al. Automated quantitative tumour response assessment of MRI in neuro-oncology with artificial

neural networks: a multicentre, retrospective study. *The Lancet Oncology* **2019**, *20*, 728-740, doi:https://doi.org/10.1016/S1470-2045(19)30098-1.

109. Kim, S.; Hoch, M.J.; Cooper, M.E.; Gore, A.; Weinberg, B.D. Using a Website to Teach a Structured Reporting System, the Brain Tumor Reporting and Data System. *Current problems in diagnostic radiology* **2021**, *50*, 356-361, doi:10.1067/j.cpradiol.2020.01.006.

110. Lee, S.J.; Weinberg, B.D.; Gore, A.; Banerjee, I. A Scalable Natural Language Processing for Inferring BT-RADS Categorization from Unstructured Brain Magnetic Resonance Reports. *Journal of digital imaging* **2020**, *33*, 1393-1400, doi:10.1007/s10278-020-00350-0.

111. Cao, H.; Wang, Y.; Chen, J.; Jiang, D.; Zhang, X.; Tian, Q.; Wang, M. Swin-Unet: Unet-Like Pure Transformer for Medical Image Segmentation. In Proceedings of the Computer Vision – ECCV 2022 Workshops, Cham, 2023//, 2023; pp. 205-218.

112. Ronneberger, O.; Fischer, P.; Brox, T. U-net: Convolutional networks for biomedical image segmentation. In Proceedings of the Medical Image Computing and Computer-Assisted Intervention–MICCAI 2015: 18th International Conference, Munich, Germany, October 5-9, 2015, Proceedings, Part III 18, 2015; pp. 234-241.

113. Yang, C.; Guo, X.; Wang, T.; Yang, Y.; Ji, N.; Li, D.; Lv, H.; Ma, T. Automatic Brain Tumor Segmentation Method Based on Modified Convolutional Neural Network. *Annual International Conference of the IEEE Engineering in Medicine and Biology Society. IEEE Engineering in Medicine and Biology Society. Annual International Conference* **2019**, *2019*, 998-1001, doi:10.1109/embc.2019.8857303.

114. Liu, Z.; Lin, Y.; Cao, Y.; Hu, H.; Wei, Y.; Zhang, Z.; Lin, S.; Guo, B. Swin transformer: Hierarchical vision transformer using shifted windows. In Proceedings of the Proceedings of the IEEE/CVF international conference on computer vision, 2021; pp. 10012-10022.

115. Çiçek, Ö.; Abdulkadir, A.; Lienkamp, S.S.; Brox, T.; Ronneberger, O. 3D U-Net: learning dense volumetric segmentation from sparse annotation. In Proceedings of the Medical Image Computing and Computer-Assisted Intervention–MICCAI 2016: 19th International Conference, Athens, Greece, October 17-21, 2016, Proceedings, Part II 19, 2016; pp. 424-432.

116. Fushiki, T. Estimation of prediction error by using K-fold cross-validation. *Statistics and Computing* **2011**, *21*, 137-146, doi:10.1007/s11222-009-9153-8.

117. Dice, L.R. Measures of the Amount of Ecologic Association Between Species. *Ecology*

1945, *26*, 297-302, doi:https://doi.org/10.2307/1932409.

118. Barragán-Montero, A.; Javaid, U.; Valdés, G.; Nguyen, D.; Desbordes, P.; Macq, B.; Willems, S.; Vandewinckele, L.; Holmström, M.; Löfman, F.; et al. Artificial intelligence and machine learning for medical imaging: A technology review. *Physica Medica* **2021**, *83*, 242-256, doi:https://doi.org/10.1016/j.ejmp.2021.04.016.

119. Giansanti, D.; Di Basilio, F. The Artificial Intelligence in Digital Radiology: Part 1: The Challenges, Acceptance and Consensus. **2022**, *10*, 509.

120. Saw, S.N.; Ng, K.H. Current challenges of implementing artificial intelligence in medical imaging. *Physica Medica* **2022**, *100*, 12-17, doi:https://doi.org/10.1016/j.ejmp.2022.06.003.

121. Martín-Noguerol, T.; Paulano-Godino, F.; López-Ortega, R.; Górriz, J.M.; Riascos, R.F.; Luna, A. Artificial intelligence in radiology: relevance of collaborative work between radiologists and engineers for building a multidisciplinary team. *Clinical Radiology* **2021**, *76*, 317-324, doi:https://doi.org/10.1016/j.crad.2020.11.113.

122. Choi, Y.; Choi, M.; Kim, M.; Ha, J.-W.; Kim, S.; Choo, J. Stargan: Unified generative adversarial networks for multi-domain image-to-image translation. In Proceedings of the Proceedings of the IEEE conference on computer vision and pattern recognition, 2018; pp. 8789-8797.

123. Xin, B.; Hu, Y.; Zheng, Y.; Liao, H. Multi-modality generative adversarial networks with tumor consistency loss for brain mr image synthesis. In Proceedings of the 2020 IEEE 17th international symposium on biomedical imaging (ISBI), 2020; pp. 1803-1807.

124. Isola, P.; Zhu, J.-Y.; Zhou, T.; Efros, A.A. Image-to-image translation with conditional adversarial networks. In Proceedings of the Proceedings of the IEEE conference on computer vision and pattern recognition, 2017; pp. 1125-1134.

125. Gittleman, H.; Lim, D.; Kattan, M.W.; Chakravarti, A.; Gilbert, M.R.; Lassman, A.B.; Lo, S.S.; Machtay, M.; Sloan, A.E.; Sulman, E.P.; et al. An independently validated nomogram for individualized estimation of survival among patients with newly diagnosed glioblastoma: NRG Oncology RTOG 0525 and 0825. *Neuro Oncol* **2017**, *19*, 669-677, doi:10.1093/neuonc/now208.

126. Was, H.; Krol, S.K.; Rotili, D.; Mai, A.; Wojtas, B.; Kaminska, B.; Maleszewska, M. Histone deacetylase inhibitors exert anti-tumor effects on human adherent and stem-like glioma cells. *Clinical epigenetics* **2019**, *11*, 11, doi:10.1186/s13148-018-0598-5.

127. Mann, B.S.; Johnson, J.R.; Cohen, M.H.; Justice, R.; Pazdur, R. FDA approval summary: vorinostat for treatment of advanced primary cutaneous T-cell lymphoma. *The oncologist* **2007**, *12*, 1247-1252, doi:10.1634/theoncologist.12-10-1247.

128. Wang, C.; Eessalu, T.E.; Barth, V.N.; Mitch, C.H.; Wagner, F.F.; Hong, Y.; Neelamegam, R.; Schroeder, F.A.; Holson, E.B.; Haggarty, S.J.; et al. Design, synthesis, and evaluation of hydroxamic acid-based molecular probes for in vivo imaging of histone deacetylase (HDAC) in brain. *American journal of nuclear medicine and molecular imaging* **2013**, *4*, 29-38.

129. Hanson, J.E.; La, H.; Plise, E.; Chen, Y.H.; Ding, X.; Hanania, T.; Sabath, E.V.; Alexandrov, V.; Brunner, D.; Leahy, E.; et al. SAHA enhances synaptic function and plasticity in vitro but has limited brain availability in vivo and does not impact cognition. *PLoS One* **2013**, *8*, e69964, doi:10.1371/journal.pone.0069964.

130. Lee, H.Z.; Kwitkowski, V.E.; Del Valle, P.L.; Ricci, M.S.; Saber, H.; Habtemariam, B.A.; Bullock, J.; Bloomquist, E.; Li Shen, Y.; Chen, X.H.; et al. FDA Approval: Belinostat for the Treatment of Patients with Relapsed or Refractory Peripheral T-cell Lymphoma. *Clinical cancer research : an official journal of the American Association for Cancer Research* **2015**, *21*, 2666-2670, doi:10.1158/1078-0432.Ccr-14-3119.

131. Gurbani, S.S.; Yoon, Y.; Weinberg, B.D.; Salgado, E.; Press, R.H.; Cordova, J.S.; Ramesh, K.K.; Liang, Z.; Velazquez Vega, J.; Voloschin, A.; et al. Assessing Treatment Response of Glioblastoma to an HDAC Inhibitor Using Whole-Brain Spectroscopic MRI. *Tomography* **2019**, *5*, 53-60, doi:10.18383/j.tom.2018.00031.

132. Gurbani, S.S.; Weinberg, B.D.; Salgado, E.; Voloschin, A.; Velazquez Vega, J.E.; Olson, J.J.; Shu, H.G.; Shim, H. Remarkable response of a patient with secondary glioblastoma to a histone deacetylase inhibitor. *Oxford medical case reports* **2020**, *2020*, omaa006, doi:10.1093/omcr/omaa006.

133. Sulman, E.P.; Ismaila, N.; Armstrong, T.S.; Tsien, C.; Batchelor, T.T.; Cloughesy, T.; Galanis, E.; Gilbert, M.; Gondi, V.; Lovely, M.; et al. Radiation Therapy for Glioblastoma: American Society of Clinical Oncology Clinical Practice Guideline Endorsement of the American Society for Radiation Oncology Guideline. *J Clin Oncol* **2017**, *35*, 361-369, doi:10.1200/jco.2016.70.7562.

134. Kazda, T.; Dziacky, A.; Burkon, P.; Pospisil, P.; Slavik, M.; Rehak, Z.; Jancalek, R.; Slampa, P.; Slaby, O.; Lakomy, R. Radiotherapy of Glioblastoma 15 Years after the Landmark Stupp's Trial: More Controversies than Standards? *Radiology and oncology* **2018**, *52*, 121-128, doi:10.2478/raon-2018-0023.

135. McDonald, M.W.; Shu, H.K.; Curran, W.J., Jr.; Crocker, I.R. Pattern of failure after limited margin radiotherapy and temozolomide for glioblastoma. *Int J Radiat Oncol Biol Phys* **2011**, *79*, 130-136, doi:10.1016/j.ijrobp.2009.10.048.

136. Prensner, J.R.; Chinnaiyan, A.M. Metabolism unhinged: IDH mutations in cancer. *Nature Medicine* **2011**, *17*, 291-293, doi:10.1038/nm0311-291.

137. Krieger, M.D.; Chandrasoma, P.T.; Zee, C.S.; Apuzzo, M.L. Role of stereotactic biopsy in the diagnosis and management of brain tumors. *Semin Surg Oncol* **1998**, *14*, 13-25, doi:10.1002/(sici)1098-2388(199801/02)14:1<13::aid-ssu3>3.0.co;2-5.

138. Scott, J.N.; Brasher, P.M.; Sevick, R.J.; Rewcastle, N.B.; Forsyth, P.A. How often are nonenhancing supratentorial gliomas malignant? A population study. *Neurology* **2002**, *59*, 947-949, doi:10.1212/wnl.59.6.947.

139. Kondziolka, D.; Lunsford, L.D.; Martinez, A.J. Unreliability of contemporary neurodiagnostic imaging in evaluating suspected adult supratentorial (low-grade) astrocytoma. *J Neurosurg* **1993**, *79*, 533-536, doi:10.3171/jns.1993.79.4.0533.

140. Di Costanzo, A.; Scarabino, T.; Trojsi, F.; Giannatempo, G.M.; Popolizio, T.; Catapano, D.; Bonavita, S.; Maggialetti, N.; Tosetti, M.; Salvolini, U.; et al. Multiparametric 3T MR approach to the assessment of cerebral gliomas: tumor extent and malignancy. *Neuroradiology* **2006**, *48*, 622-631, doi:10.1007/s00234-006-0102-3.

141. Press, R.H.; Zhong, J.; Gurbani, S.S.; Weinberg, B.D.; Eaton, B.R.; Shim, H.; Shu, H.G. The Role of Standard and Advanced Imaging for the Management of Brain Malignancies From a Radiation Oncology Standpoint. *Neurosurgery* **2019**, *85*, 165-179, doi:10.1093/neuros/nyy461.

142. Law, M. MR spectroscopy of brain tumors. *Top Magn Reson Imaging* **2004**, *15*, 291-313, doi:10.1097/00002142-200410000-00003.

143. Lin, A.; Bluml, S.; Mamelak, A.N. Efficacy of proton magnetic resonance spectroscopy in clinical decision making for patients with suspected malignant brain tumors. *J Neurooncol* **1999**, *45*, 69-81, doi:10.1023/a:1006387703127.

144. Schlemmer, H.P.; Bachert, P.; Herfarth, K.K.; Zuna, I.; Debus, J.; van Kaick, G. Proton MR spectroscopic evaluation of suspicious brain lesions after stereotactic radiotherapy. *AJNR Am J Neuroradiol* **2001**, *22*, 1316-1324.

145. Miller, B.L. A review of chemical issues in 1H NMR spectroscopy: N-acetyl-L-aspartate, creatine and choline. *NMR Biomed* **1991**, *4*, 47-52, doi:10.1002/nbm.1940040203.

146. Go, K.G.; Kamman, R.L.; Mooyaart, E.L.; Heesters, M.A.; Pruim, J.; Vaalburg, W.; Paans, A.M. Localised proton spectroscopy and spectroscopic imaging in cerebral gliomas, with comparison to positron emission tomography. *Neuroradiology* **1995**, *37*, 198-206, doi:10.1007/bf01578258.

147. Chang, J.; Thakur, S.; Perera, G.; Kowalski, A.; Huang, W.; Karimi, S.; Hunt, M.; Koutcher, J.; Fuks, Z.; Amols, H.; et al. Image-fusion of MR spectroscopic images for treatment planning of gliomas. *Med Phys* **2006**, *33*, 32-40, doi:10.1118/1.2128497.

148. Graves, E.E.; Pirzkall, A.; Nelson, S.J.; Larson, D.; Verhey, L. Registration of magnetic resonance spectroscopic imaging to computed tomography for radiotherapy treatment planning. *Med Phys* **2001**, *28*, 2489-2496, doi:10.1118/1.1420400.

149. Jakacki, R.I.; Cohen, K.J.; Buxton, A.; Krailo, M.D.; Burger, P.C.; Rosenblum, M.K.; Brat, D.J.; Hamilton, R.L.; Eckel, S.P.; Zhou, T.; et al. Phase 2 study of concurrent radiotherapy and temozolomide followed by temozolomide and lomustine in the treatment of children with high-grade glioma: a report of the Children's Oncology Group ACNS0423 study. *Neuro Oncol* **2016**, *18*, 1442-1450, doi:10.1093/neuonc/now038.

150. Beare, R.; Lowekamp, B.; Yaniv, Z. Image Segmentation, Registration and Characterization in R with SimpleITK. *Journal of Statistical Software* **2018**, *86*, 1 - 35, doi:10.18637/jss.v086.i08.

151. Yaniv, Z.; Lowekamp, B.C.; Johnson, H.J.; Beare, R. SimpleITK Image-Analysis Notebooks: a Collaborative Environment for Education and Reproducible Research. *Journal of Digital Imaging* **2018**, *31*, 290-303, doi:10.1007/s10278-017-0037-8.

152. Lowekamp, B.; Chen, D.; Ibanez, L.; Blezek, D. The Design of SimpleITK. *Frontiers in Neuroinformatics* **2013**, *7*, doi:10.3389/fninf.2013.00045.

153. Jackson, R.J.; Fuller, G.N.; Abi-Said, D.; Lang, F.F.; Gokaslan, Z.L.; Shi, W.M.; Wildrick, D.M.; Sawaya, R. Limitations of stereotactic biopsy in the initial management of gliomas. *Neuro-Oncology* **2001**, *3*, 193-200, doi:10.1093/neuonc/3.3.193.

154. Gates, E.D.H.; Lin, J.S.; Weinberg, J.S.; Hamilton, J.; Prabhu, S.S.; Hazle, J.D.; Fuller, G.N.; Baladandayuthapani, V.; Fuentes, D.; Schellingerhout, D. Guiding the first biopsy in glioma patients using estimated Ki-67 maps derived from MRI: conventional versus advanced imaging. *Neuro Oncol* **2019**, *21*, 527-536, doi:10.1093/neuonc/noz004.

155. van den Bent, M.J.; Tesileanu, C.M.S.; Wick, W.; Sanson, M.; Brandes, A.A.; Clement, P.M.; Erridge, S.; Vogelbaum, M.A.; Nowak, A.K.; Baurain, J.F.; et al. Adjuvant and concurrent temozolomide for 1p/19q non-co-deleted anaplastic glioma (CATNON; EORTC study 26053-22054): second interim analysis of a randomised, open-label, phase 3 study. *The Lancet Oncology* **2021**, *22*, 813-823, doi:10.1016/S1470-2045(21)00090-5.

156. Everix, L.; Seane, E.N.; Ebenhan, T.; Goethals, I.; Bolcaen, J. Introducing HDAC-Targeting Radiopharmaceuticals for Glioblastoma Imaging and Therapy. *Pharmaceuticals* **2023**, *16*, 227.

157. Galanis, E.; Anderson, S.K.; Miller, C.R.; Sarkaria, J.N.; Jaeckle, K.; Buckner, J.C.; Ligon, K.L.; Ballman, K.V.; Moore, D.F., Jr.; Nebozhyn, M.; et al. Phase I/II trial

of vorinostat combined with temozolomide and radiation therapy for newly diagnosed glioblastoma: results of Alliance N0874/ABTC 02. *Neuro Oncol* **2018**, *20*, 546-556, doi:10.1093/neuonc/nox161.

158. Moonen, C.T.; von Kienlin, M.; van Zijl, P.C.; Cohen, J.; Gillen, J.; Daly, P.; Wolf, G. Comparison of single-shot localization methods (STEAM and PRESS) for in vivo proton NMR spectroscopy. *NMR Biomed* **1989**, *2*, 201-208, doi:10.1002/nbm.1940020506.